MODELING WAVE-WAVE INTERACTIONS AND 3-D WAVE-INDUCED CIRCULATION IN THE PRESENCE OF REFLECTION-DIFFRACTION EFFECTS

A Dissertation

by

ABHISHEK SHARMA

Submitted to the Office of Graduate and Professional Studies of
Texas A&M University
in partial fulfillment of the requirements for the degree of

DOCTOR OF PHILOSOPHY

Chair of Committee,	Vijay Panchang
Co-Chair of Committee,	James Kaihatu
Committee Members,	Scott Socolofsky
	Prabir Daripa
Head of Department,	Robin Autenrieth

May 2015

Major Subject: Ocean Engineering

ABSTRACT

Accurate prediction of wave environment is critical to the design of ports, harbors and coastal structures. In this dissertation, two advancements for existing phase-resolving models based on elliptic mild-slope equation (EMSE) are proposed. First, an approach is developed to simulate wave-wave interactions using nonlinear elliptic mild-slope equation in domains where wave reflection, refraction, diffraction and breaking effects must also be considered. This involves the construction of an efficient solution procedure involving effective boundary treatment, modification of the nonlinear equation to resolve convergence issues, and validation of the overall approach. For solving the second-order boundary-value problem using finite difference method, the Alternating Direction Implicit (ADI) scheme is employed, and the use of approximate boundary conditions is supplemented, for improved accuracy, with internal wave generation method and dissipative sponge layers. The performance of the nonlinear model is investigated for a range of practical wave conditions involving reflection, diffraction and shoaling in the presence of nonlinear wave-wave interactions. In addition, the transformation of wave spectrum due to nonlinear shoaling and breaking, and nonlinear harbor resonance inside a rectangular harbor are simulated. Numerical calculations are compared with the results from other relevant nonlinear models and experimental data available in literature. Based on these results, a methodology is then developed which can be used to advance the existing finite element models to include wave-wave interaction effects. The finite element model developed in this study is applied to simulate nonlinear wave transformation inside Ponce de Leon Inlet, FL. Results show that the methodology developed here performs reasonably well, and has thus improved the applicability of this class of

wave transformation models.

Second, a generalized expression for the three-dimensional radiation stress tensor (RST) is derived from first principles. Computation of vertically-dependent RS using this expression requires prior knowledge of the complex velocity potential obtained from phase-resolving wave models based on linear wave theory. As such, this represents a generalization of the vertically-integrated (2-D) RST proposed by Bettess and Bettess (1982) and is applicable to arbitrary linear wave fields. It can therefore be used to simulate 3-D wave-induced flow fields in harbors and coastal regions where the presence of structures and bathymetric irregularities may cause reflection, diffraction, breaking and focusing (caustics). To investigate the performance of the generalized formulation, a 3-D coupled current-wave system is developed which involves a wave prediction model (based on elliptic mild-slope equation) and a 3-D circulation model that uses the generalized RST. The coupled system is then applied to three different cases involving wave propagation over a sloping beach, a standing-wave case, and wave interaction with a shore-parallel breakwater. Numerical calculations of the wave-induced set-up/down and the 3-D current fields are compared with analytical results and experimental data available in literature. Results show that the approach developed here performs reasonably well and has a wide range of applicability. In addition, the existing (2-D and 3-D) radiation stress formulations are shown to be the special cases of this generalized form, which is further used to develop an analytical expression of 3-D RST for full/partial standing waves over flat bottom.

TABLE OF CONTENTS

Page

LIST OF FIGURES

FIGURE Page

LIST OF TABLES

TABLE Page

1. INTRODUCTION, LITERATURE REVIEW AND OBJECTIVES

1.1 Context

Accurate prediction of wave environment is critical to the design of ports, harbors and coastal structures. While harbors are important hubs for commercial, naval, social and cultural activities, nearshore regions contribute to the growth of local and state economies. With an ever increasing demand for harbor expansions and nearshore constructions, engineers are often challenged to provide robust infrastructure for the safety and efficiency of harbor and nearshore operations. Studies involving physical and mathematical models are often conducted simultaneously to ensure the feasibility of the proposed designs. For design projects, two physical quantities of major concern are wave field and the associated wave-induced flow field (currents and setup/down). For example, big waves inside harbors may disturb harbor tranquility which can cause operational difficulties, and the wave-induced currents in nearshore regions and near harbor entrances may lead to the problems associated with sediment transport, erosion, scouring, etc.

Reliable modeling of waves and circulation pattern in harbors and nearshore regions is often obtained using numerical techniques; however, sometimes these domains challenge modelers with a variety of difficulties. For example, as shown in Fig. 1.1, arbitrarily-shaped coastlines, harbor walls, artificial structures like breakwaters present in harbors may cause significant wave transformation due to reflection, diffraction, refraction, breaking and focusing. In addition, the incident waves may represent a spectrum of wave frequencies, and the mechanism of wave-wave interactions may generate new harmonics which may trigger harbor resonance and, as a consequence, may damage mooring lines and disrupt vessel operations in harbors.

In this dissertation, two significant advancements for existing phase-resolving models based on elliptic mild-slope equation (EMSE) are proposed. The phase-resolving nature of these elliptic models allow them to handle complex domains (with reflection, diffraction, etc.) similar to the one shown in 1.1. Precisely, these two advancements are related to the simulation of nonlinear wave-wave interactions and the computation of vertically-varied wave-induced forcing using elliptic models. A detailed description of these advancements, motivation for this research, research objectives and the organization of the dissertation are provided in this chapter.

1.2 Nonliear Wave-Wave Interactions and Elliptic Equation

The linear elliptic mild-slope equation [1, 2] has been utilized for a wide range of applications that require reliable simulations of wave phenomena such as refraction, diffraction, and reflection from bathymetric features and structures. Extensions of this equation have also been developed to incorporate steep-slope effects [3, 4], floating docks [5], and nonlinear mechanisms such as wave-current interaction [6], wave breaking [7] and amplitude dispersion [8]. In the last few decades, harbor wave models developed using the elliptic equation (e.g. PHAROS, HARBD, MIKE21-EMS, CGWAVE, etc) have found increasing use in practice. While other phase-resolving models such as Boussinesq models can also simulate the mechanisms mentioned above, the elliptic equation automatically spans the full range of water depths of concern in engineering applications, enabling it to readily handle short as well as long wavelengths with generally less susceptibility to numerical and other problems, such as those noted by Walkley and Berzins [9] for harbor applications. In addition, unlike its "parabolic approximation" [10], the elliptic equation places no limitation on the angle of wave incidence or the degree and direction of wave reflection and scattering. Thus elliptic equation models have been applied to Los

Angeles/Long Beach harbor [11], Douglas Harbor [5], Venice Harbor [12], etc. and in nearshore regions around submerged as well as surface protruding structures like piers and breakwaters (e.g. [13]).

Their widespread usefulness notwithstanding, one major limitation of these elliptic mild-slope equation models is that the governing equation (with or without extensions mentioned above) is rooted in linear theory; hence they completely ignore wave-wave interactions. Even some spectral wave propagation studies (e.g. [14, 7]) conducted using these models have relied on simple linear superposition of the wave components. However, nonlinear wave-wave interactions, which, in general, involve transfer of energy and wave phase coupling among spectral components, are known to be quite significant especially in shoaling regions [15]. In fact, data from [16] suggest that the higher harmonics generated through such interactions can have amplitudes larger than the incident primary harmonic even in simple cases. In harbors, nonlinear interactions may contribute significantly to resonance [17, 18]. As mentioned earlier, harbors with large natural periods can be excited by long period waves, resulting in potential damage to mooring lines, fenders, and piers, and undesirable vessel motions. The primary source of the generation of these long period waves sometimes is the nonlinear interaction (between short-period waves) which occur in shallower regions in the vicinity of harbor entrances. Eventually both short-period as well as long-period waves get trapped and amplified inside the harbor.

In the past, nonlinear oscillations inside harbors have been modeled in an *ad hoc* manner or using application-specific approaches, for example, by decomposing the domain into separate regions and selecting an appropriate model for each subdomain. Rogers and Mei [17] applied linear theory in the deep-water part of their domain and the conventional shallow-water equations (including wave-wave interactions) inside the harbor region. Similarly, U.S. Army Corps of Engineers developed

the Infra-gravity Wave Toolbox (IGWT) to couple a linear elliptic model (for the harbor interior) with a one-dimensional Boussinesq model (for the exterior region). The one-dimensional model (which includes waves generated via nonlinear interactions) in the IGWT provides the input for the linear elliptic model, which then simulates oscillations inside the harbor, one frequency at a time, neglecting the possibility of nonlinear interactions inside the harbor [19]. Besides being cumbersome, the reliability of such methods cannot be assured because they clearly do not couple the solutions in the sub-domains; rather, one sub-domain merely provides an approximate input to the other.

To overcome these limitations and to provide a basis for the effective modeling of nonlinear wave transformation in complex coastal and harbor environments, we consider the second-order nonlinear extension of the original mild-slope equation [20, 21]. Although this extension includes wave-wave coupling, this elliptic nonlinear mild-slope equation (hereafter referred to as ENMSE) has linear characteristics (i.e. fully-dispersive) of the original mild slope equation, and hence would be applicable (like the linear elliptic model) to a wide range of practical wave conditions and water depths. Solutions with this approach have in fact been obtained in the past [20, 21, 22] but recourse was made to the parabolic approximation. This approximation is certainly computationally effective because it reduces the order of all (or some of) the highest-order derivatives. However, it is suitable only when (1) waves propagate along a principal wave direction, and wave diffraction in this direction is negligible; (2) the reflected or backscattered component of the wave is negligibly small; and (3) wave amplitudes vary slowly in space. This approach is thus not suitable to domains where structures and arbitrarily-shaped geometries (as found in harbors) may generate reflected or back-scattered waves, or may violate the assumption of slowly-varying amplitudes. In fact, one such difficulty has already been reported [20]

while modeling one nonlinear wave shoaling scenario.

In this study we attempt the development of a model based on the ENMSE (i.e. without invoking any simplifying approximations) and explore the difficulties that may arise while eventually tackling domains of complex shape. Solution of the ENMSE, owing to the high degree of nonlinearity in some cases, can pose several problems associated with convergence, boundary conditions, etc. which must be addressed.

1.3 Generalized Three-dimensional Wave-induced Forcing

Many theoretical, analytical and experimental studies pertaining to wave-induced circulation in nearshore regions have been conducted over the last few decades. Most of these studies have utilized circulation models based on the vertically-integrated (2DH) Navier-Stokes equations, and, commensurately, the wave-induced forcing was obtained from the vertically-integrated (2-D) radiation stresses (e.g. [23], [24], [25]). Although these models have been applied successfully to simulate wave-induced nearshore processes (e.g. longshore currents, rip currents, beach evolution and morphology), they are not appropriate for applications in which reliable prediction of the vertical structure of flow field is critical. Therefore, recent years have seen a significantly increased use of 3-D flow models (e.g. POM, EFDC, ROMS, CH3D, Delft3D) in coastal engineering applications. Note that two types of formulations are used to incorporate the wave-induced effects in flow models: (1) radiation stress formulations, and (2) vortex-force formulations. The first category formulations are used with the flow equations given in terms of Lagrangian velocities (e.g. in POM and EFDC models), and the wave-induced forcing in these equations appears as the divergence of radiation stresses. In contrast, the vortex-force formalism appears (as a vortex force and a Bernoulli head) in the flow equations given in terms of Eule-

rian velocities (e.g. in ROMS model). Both approaches have been found to perform satisfactorily by Moghimi et al. [26] and Kumar et al. [27, 28], who compared wave-induced quantities obtained using both types of formulations for a number of applications. In addition, Lane et al. [29] stated that the two formulations are formally equivalent. In the present study, we focus only on the first category of formulations. More details regarding the vortex-force formulations can be found elsewhere in [30] and [31].

With regards to the radiation stress formulations, Xia et al. [32] and Mellor [33] suggested that the use of 2-D RST with 3-D flow models is inadequate, and therefore they extended the concept of the conventional 2-D RST into three dimensions. Recently, Sheng and Liu [34] also reported inconsistencies in the flow pattern simulated using the 2-D RST with a 3-D flow model for the cases of wave propagation over a reef and a sloping beach.

In the pioneering work of Mellor [33], an expression for the vertically-dependent (3-D) RST was proposed while deriving a closed set of equations for 3-D wave-current interactions. Some inconsistencies in their RS formulation were reported by Ardhuin and Bennis [35]; Mellor [36, 37, 38] later addressed these inconsistencies and corrected their original RS formulation by using a more accurate expression for the pressure term which was not treated properly in [33]. Mellor [38] also emphasized that the vertically-integrated form of M11 is consistent with [23] and [39]. (The corrected formulation in [37, 38] hereafter referred to as M11). Despite some ongoing debate (e.g. [27], [40], [26]) regarding the accuracy of M11 in shoaling regions, it has been used satisfactorily with 3-D circulation models for a broad set of practical applications (e.g. [41], [42], [34], [27], [43]). Recently, Mellor [44] proposed a modification to M11 in unpublished works. (The modified M11 hereinafter referred to as M13). Unlike M11, the M13 formulation has not been thoroughly validated against field or

experimental data. Although Mellor [45] applied it to a hypothetical case of a sloping beach with no wave breaking and found good agreement between the modeled and analytical set-up/down results, they did not discuss the accuracy of the modeled velocity field.

Apart from M11 and M13, an expression for 3-D RST tensor (hereafter L04) was derived by Lin [46]; the treatment of pressure term in their work differs from the one used by Mellor [37] in the derivation of M11. Another formulation for 3-D RST was derived by Xia et al. [32] using an entirely different approach; however, in a detailed study by Sheng and Liu [34], severe anomalies (e.g. spurious undertow profile over a sloping beach) were reported in the modeled flow field computed using the approach of [32].

While the above developments aim to extend the 2-D RST into 3-D, it should be noted that, like other related works (e.g. [47]) they all are limited to purely progressive wave fields, and the formulations are best suited for phase-averaged models. As a result, their applicability in regions of wave reflection, diffraction and caustics, especially in the presence of structures and bathymetric irregularities, is questionable. Such situations are often encountered in practice. For example, in the presence of breakwaters and seawalls, partial or full standing waves lead to the formation of equilibrium scour/deposition profiles ([48], [49], [50], [51]) and beach cusps ([52],[53]). For such complex problems, [24] and [54] proposed, in 2-D, the relevant RSTs. These RSTs have been used to simulate flow field around breakwaters (e.g. [55]). In the context of 3-D RST, Zhang and Liu [56] did introduce a formulation for standing waves; however, the derivation is based on the inconsistent approach developed by Xia et al. [32] (mentioned above) and uses an erroneous expression for the pressure term. In addition, their formulation pertains only to the strictly one-dimensional standing wave cases. (See discussion later for more details).

To overcome the above limitations, here we address the development of an expression for a "generalized" 3-D RST, i.e. a vertically-dependent formulation suitable for an arbitrary linear wave field and applicable to complex domains where reflection, diffraction, and focusing may not be ignored. Such a formulation is intended to be consistent with phase-resolving models for which the wave potential Φ has the form

$$\Phi = Re\left(\phi(x,y)\frac{\cosh k(h+z)}{\cosh kd}exp(-i\omega t)\right) \tag{1.1}$$

where $k(x,y)$ is wave number and is related to wave frequency ω and local depth $h(x,y)$ through the linear dispersion relation; $d = h + \hat{\eta}$ is total water depth, and $\hat{\eta}$ is set-up/down. Notice that similar to other notable works (e.g. [23], [36], [32]), the vertical structure of the wave field in Eq. (1.1) is based on linear theory; however, unlike previous works, no assumption regarding the nature of the complex potential $\phi(x,y)$ in Eq. (1.1) is employed in the derivation of new generalized RST. Three different approaches used in the derivation of M11, M13 and L08 are considered in this study for deriving a new generalized formulation for 3-D RST.

In particular, the above expression for Φ (Eq. 1.1) is consistent with elliptic models based on the standard mild-slope equation of [1, 2]. Such models have been utilized for a wide range of harbor and coastal engineering applications that require simulation of wave transformation around structures and in arbitrarily-shaped domains. Being inherently fully-dispersive, they are applicable to all water depths, enabling them to readily handle short as well as long wavelengths. The generalized expression for the "vertically-integrated" (2-D) RST, which was derived by Bettess and Bettess [24], is consistent with Φ obtained from elliptic models, and the new formulation described here may be considered as a 3-D extension of their formulation. In fact, by vertical integration of the generalized formulation, the formulation

of Bettess and Bettess [24] (herein referred to as BB2D) is recovered. Moreover, the new formulation transforms to M11 for a progressive wave field over a flat bottom. Finally, it can also be used to derive new analytical expressions for the 3-D RST in cases of full/partial standing waves in 1-D for which the wave field $\phi(x, y)$ is available.

Despite these advantages, the generalized 3-D RS formulation, unlike the M11, involves the computation of second-order derivatives which can perhaps be a source of numerical errors. Such an issue was raised by Dingemans et al. [25] with regards to the 2-D generalized RS formulation of Bettess and Bettess [24] which also involve the computation of second-order derivatives. Therefore, to investigate the behavior of the new generalized formulation, and to address this issue of numerical errors, we consider the coupling of an elliptic model with a 3-D circulation model and a depth-integrated (2-D) circulation model to simulate wave-induced setup/down current field in complex scenarios discussed above. The results obtained using the BB87, and an alternative approach proposed by Dingemans et al. [25] (hereafter reffeblack to as D87) which ignores the computation of higher-order terms in the BB87 are also included for comparisons in some cases.

1.4 Research Objectives and Dissertation Outline

1. The first objective here is to develop a finite element model based on the ENMSE which is capable of simulating nonlinear wave transformation in complex harbor domains and nearshore regions. This objective will be accomplished in a systematical manner by completing the following list of tasks:

    - For a preliminary investigation of the ENMSE, a finite difference model is first developed using an efficient and unconditionally-stable Alternating Direction Implicit (ADI) scheme. The numerical problems associated with convergence, iterative procedure, etc. (owing to the nonlinearities) are

then addressed.

- An effective method for boundary treatment is developed which involves the internal generation of waves using source function method and wave absorption using dissipative sponge layers.
- The numerical model together with the boundary treatment method is then validated by simulating wave environment for a variety of practical wave conditions encounteblack in harbor and nearshore regions.
- Next, a framework for the development of a finite element model based on Galerkin formulation is proposed, and an effective algorithm for numerical solution is designed that can be used to extend existing linear finite element mild slope models to incorporate nonlinear wave-wave interaction effects.
- The finite element model with the above mentioned boundary treatmnet method is then validated using test cases and is applied to simulate nonlinear wave transformation for a field case of Ponce de Leon Inlet located in Florida.

2. The second objective is to design a mechanism that can be used to simulate 3-D wave-induced flow field in regions with significant wave reflection, diffraction and focusing effects. This will be achieved in the following manner:

   - A new formulation for generalized vertically dependent wave RST is first derived using first principles. The generalized formulation is applicable to an arbitrary linear wave field (including reflection, diffraction effects) obtained using elliptic models.

- A coupled system of an elliptic model and a 3-D flow model is then developed which can be forced with vertically dependent wave-induced forcing and can simulate wave-induced setup/down and current field in complex scenarios.
- Finally, the coupled system with the generalized vertically dependent wave RST is applied to a number of application involving breakwaters and sloping beaches.

Introduction and literature review will be provided in Chapter 1. A brief background on linear elliptic models and the second-order ENMSE will be given in Chapter 2. This chapter will also describe well-accepted boundary treatment method for linear elliptic models, newly proposed boundary treatment method for the nonlinear model, convergence issues with the ENMSE, and the derivation of an alternative equation with improved convergence. Chapter 3 will include the development of a finite difference model which is consideblack for the preliminary investigation of ENMSE by simulating nonlinear wave transformation in a variety of cases. The development of a finite element model including an iterative solution scheme will be discussed in Chapter 4. Next, The new generalized 3-D formulation for vertically dependent RS is derived from first principles in Chapter 5; its expression in terms of the complex surface elevation ϕ from the elliptic models will also be presented in this section. In addition, the new generalized formulation will be related to other RS formulations (e.g. Mellor, 2008; Bettess and Bettess, 1987; Dingemans et al., 1987; Longuet-Higgins and Stewart, 1964), and a new expression for vertically-dependent RS for a standing wave case will be derived. A brief discussion pertaining to the salient features of the 3-D circulation model used in this study will be provided in Chapter 6. The suitability of some relevant formulations with the coupled system of

elliptic model and the 3-D circulation model is next examined in Chapter 6 by simulating wave-induced circulation for a series of test cases involving wave reflection and diffraction effects. A brief discussion about the physical mechanism of wave-induced circulation, and the results of wave-induced setup/down and current field are also included for these test cases. Finally, the conclusion and the recommendations for future work are provided in Chapter 7.

Figure 1.1: Los Angeles/Long Beach Harbor area.

2. LINEAR AND NONLINEAR ELLIPTIC MILD SLOPE EQUATION

Phase-resolving wave models, as discussed earlier in Chapter 1, are well suited to domains with complex bathymetric and geometric features where the effects of wave diffraction and reflection can be important. These mass-balance models are in general based on water wave boundary value problem for inviscid and irrotational wave motion given by

$$\nabla_h{}^2\phi + \Phi_{zz} = 0; \quad -h \le z \le \tilde{\eta}, \tag{2.1}$$

$$\Phi_z = -\nabla_h h.\nabla_h \Phi; \quad z = -h, \tag{2.2}$$

$$g\tilde{\eta} + \Phi_t + \frac{1}{2}\left(\nabla_h \Phi\right)^2 + \frac{1}{2}\left(\Phi_z\right)^2; \quad z = \tilde{\eta}, \tag{2.3}$$

$$\tilde{\eta}_t - \Phi_z + \nabla_h \tilde{\eta} \cdot \nabla_h \Phi = 0; \quad z = \tilde{\eta}, \tag{2.4}$$

where the Cartesian coordinate system (x, y, z) is located on the still waver level (SWL), with z measured positive upwards from the SWL; Φ denotes three-dimensional complex wave potential; $\tilde{\eta}$ denotes surface elevation; ∇_h is the gradient operator in the horizontal Cartesian coordinates (x, y); g is the acceleration due to gravity; and subscripts denote differentiation.

This dissertation focuses mainly on the phase resolving models based on elliptic mild slope equation. The linear form of this equation was first proposed by [1, 2] and has since been utilized for a wide range of applications. A second-order extension of this equation [20, 21] was later proposed to incorporate triad wave interaction effects. In this chapter, we first briefly discuss some relevant features of the linear mild slope models, and later we discuss the second-order ENMSE, an alternative equation with improved convergence, and a new method for boundary treatment.

2.1 Linear Elliptic Wave Models

The standard mild-slope equation of Berkhoff [1, 2] is based on first-order (in $\epsilon = ka$ (where k is wave number and a is a characteristic wave amplitude) truncation of vertically integrated water wave boundary problem given in Eqs. (2.1-2.4). Some variants of this linear equation have also been developed to incorporate steep-slope effects [3], and nonlinear mechanisms such as wave-current interaction [6], wave breaking [7] and amplitude dispersion [10]. For nearshore regions, the wave-breaking effects significantly alter the wave transformation and wave-induced circulation, and the following extension (e.g. Booij, 1981; de Giro-lamo et al., 1988; Massel, 1992; Isobe, 1999) which incorporates breaking effects in terms of a parameterized dissipation function is mostly used:

$$\nabla_h \cdot \left(CC_g \nabla_h \hat{\phi} \right) + \left(k^2 CC_g + i\omega\gamma \right) \hat{\phi} = 0 \tag{2.5}$$

where C and C_g are phase and group velocity respectively; and γ is the parameterized breaking dissipation factor; and $\hat{\phi}$ denotes two-dimensional complex surface elevation. Note that Eq. (2.5) is valid under the mild-slope assumption $|\nabla h|/kh \leq 1$. This assumption can however be relaxed by incorporating the steep-slope effects ([3]) which allows Eq. (2.5) to handle slopes as steep as 1:2. The time-harmonic 3-D complex velocity potential Φ is defined in terms of $\hat{\phi}$ using

$$\Phi = Re \left(\hat{\phi}(x, y) \frac{\cosh k(h+z)}{\cosh kh} exp(-i\omega t) \right) + CC \tag{2.6}$$

where CC denotes complex conjugate.

The wave height (H), surface elevation ($\tilde{\eta}$) and wave propagation angle (θ) at all grid locations is obtained from complex $\hat{\phi}$ using

$$H = \frac{2\omega}{g}\left|\hat{\phi}\right|, \tag{2.7}$$

$$\tilde{\eta} = -\frac{1}{g}\frac{\partial \Phi}{\partial t} \quad \text{at } z = 0 \tag{2.8}$$

and

$$\theta = arctan\left(\frac{\partial s/\partial y}{\partial s/\partial x}\right), \tag{2.9}$$

where $s(x, y)$ denotes the phase of the complex surface elevation $\phi(x, y)$ and follows the relation $\phi = (H/2)exp(is)$. Actually, the above expression for θ is valid only for a progressive wave field; at locations where wave reflection, diffraction and focusing occurs, the use of Eq. (2.9) may produce spurious results. In fact, in such situations the wave propagation angle is not defined. The components of wave velocity $(\tilde{u}_\alpha, \tilde{w})$ and the dynamic pressure $\tilde{p}_d$ under waves is defined using the following relations from linear wave theory:

$$(\tilde{u}_\alpha, \tilde{w}) = Re\left(\frac{\partial \hat{\phi}}{\partial x_\alpha}\frac{\cosh k(h+z)}{\cosh kd}exp(-i\sigma t), k\hat{\phi}\frac{\sinh k(h+z)}{\cosh kd}exp(-i\omega t)\right) \tag{2.10}$$

$$\tilde{p}_d = \rho\omega\hat{\phi}\frac{\cosh k(h+z)}{\cosh kd}exp(-i\omega t) \tag{2.11}$$

where α, β denote horizontal coordinates.

For elliptic equation, many parameterizations for breaking dissipation factor γ have been proposed [7] and have rigourously been verified against field data (e.g. Larson, 1995; Kamphuis, 1994). Since the breaking dissipation factor, in general, is a function of wave height which is not known *a priori*, Eq. (2.5) must be solved

using iterations. The performance of some of these breaking models with the elliptic equation was investigated by Zhao et al. [7] who developed an iterative technique for implementing these breaking models with the elliptic equation. A similar technique is used in this study to obtain numerical solution; more details regarding the iterative procedure and the convergence issues are discussed in [7].

2.2 Boundary Conditions

A typical coastal domain, on which the elliptic equation (Eq. 2.5) is solved, is shown in Fig. 2.1. For the completeness of the boundary-value problem, two types of boundary conditions: (1) along coastlines and structural boundaries, and (2) along the artifical open-ocean boundaries are generally assigned. Mathematical details regarding these boundary conditions are also provided in [11, 7]. A short description regarding the boundary conditions at closed and an open-ocean boundaries (see Fig. 2.1) is provided here for use in later discussions.

2.2.1 Closed Boundary Condition

Model domains are enclosed by closed boundaries represented by arbitrary shaped coastlines or surface-penetrating structures like breakwaters, jetties, pier legs, sea-walls, etc. Along closed boundaries, the following condition has mostly been used:

$$\frac{\partial \hat{\phi}}{\partial n} = \left(\frac{1 - K_r}{1 + K_r} \right) \hat{\phi} \tag{2.12}$$

where n is the normal directed outward to the boundary and K_r is the reflection coefficient which varies between 0 and 1. $K_r = 1$ represents perfectly reflecting boundary, whereas $K_r = 0$ corresponds to a fully-absorbing boundary.

2.2.2 Open Boundary Condition

Along the open ocean boundary, denoted by a semi-circle or a full outgoing waves must leave the domain. The open boundary condition which is based on parabolic approximation is given by:

$$\frac{\partial \hat{\phi}}{\partial r} + p\hat{\phi} + \frac{\partial^2 \hat{\phi}}{\partial \theta^2} = 0 \tag{2.13}$$

where

$$p = \frac{k^2 r^2 + K_0^2 r^2 + ik_0 r + 1/4}{2ik_0 r^2};$$

$$q = \frac{1}{2ik_0 r^2};$$

and k_0 can be computed using the mean water depth along the open boundary. As shown in Fig. 2.1, the elliptic equation applies in the domain, and the boundary condition in Eq. 2.13 is applied only along the semi-circular or circular open boundary.

2.3 Elliptic Nonlinear Mild-Slope Equation (ENMSE)

Starting from the fully-nonlinear boundary value problem for the inviscid and irrotational wave motion, and using a Taylor series expansion about the still water level (SWL) to second-order with parameter $\epsilon = ka$ (where k is wave number and a is a characteristic wave amplitude), a nonlinear time-dependent wave transformation model for the wave propagation over mildly-sloping depths was derived by Kaihatu and Kirby [20]:

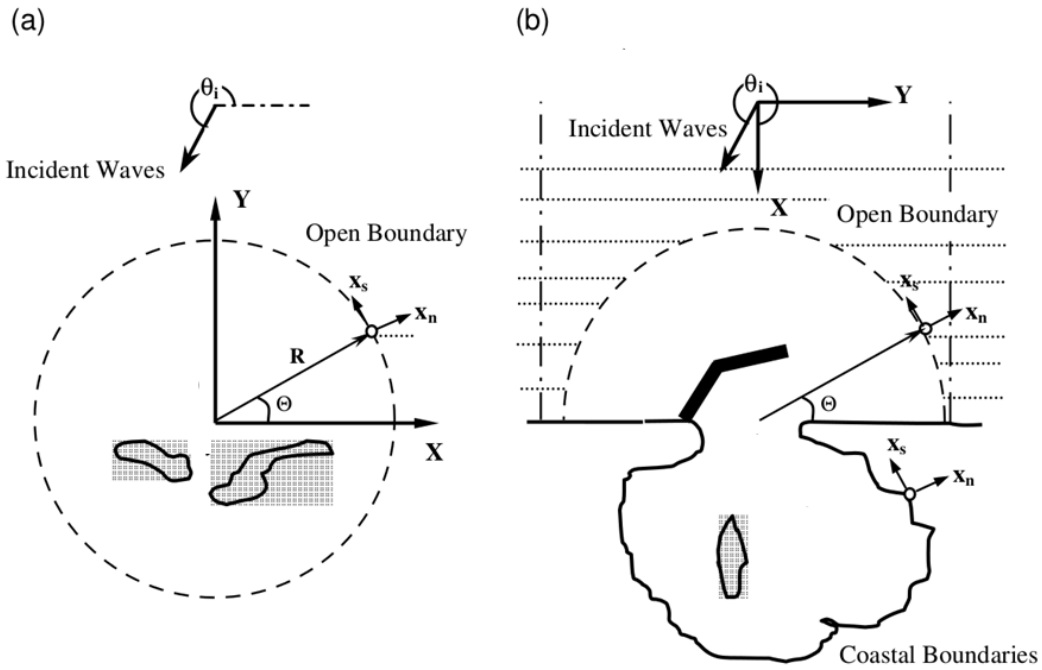

Figure 2.1: Definition sketch of a typical wave model domain. (a) Open-sea problem; (b) coastal/harbor problem.

.

$$\tilde{\phi}_{n_{tt}} - \nabla_h \cdot [(CC_g)_n \nabla_h \tilde{\phi}_n] + {\omega_n}^2 \left(1 - \frac{C_{gn}}{C_n}\right) \tilde{\phi}_n$$
$$= \frac{1}{2} \left\{ \sum_l \sum_m \left[\frac{\omega_l^2 + \omega_m^2}{g^2} \left(\tilde{\phi}_{l_t} \tilde{\phi}_{m_t} \right)_t - \frac{\omega_l^2 \omega_m^2}{g^2} \left(\tilde{\phi}_l \tilde{\phi}_m \right)_t \right] \right.$$
$$\left. - \sum_l \sum_m \left[\left(\nabla_h \tilde{\phi}_l \cdot \nabla_h \tilde{\phi}_m \right)_t + \nabla_h \cdot \left(\tilde{\phi}_{l_t} \nabla_h \tilde{\phi}_m \right) + \nabla_h \cdot \left(\tilde{\phi}_{m_t} \nabla_h \tilde{\phi}_l \right) \right] \right\}_n \quad (2.14)$$

where ∇_h is the two-dimensional gradient operator in the horizontal Cartesian coordinates (x, y); and g is the acceleration due to gravity. Eq. (2.14) represents a set of N coupled hyperbolic equations where the subscript $n(= 1, 2, ..., N)$ represents the n^{th} frequency component. C_n and C_{gn} are phase and group velocity, respectively, for the n^{th} frequency component, whose expressions are given by linear wave theory; and the complex time-dependent wave potential function $\tilde{\phi_n}$ has an assumed relationship with the resultant velocity potential Φ

$$\Phi(x, y, z, t) = \sum_{n=1}^{N} f_n(z) \tilde{\phi_n}(x, y, t) \quad (2.15)$$

where z is the vertical coordinate starting at the SWL; and the wave angular frequency ω_n and the wave number k_n for the n^{th} frequency component are related by the linear dispersion relation. The function $f_n(z) = \cosh(k_n(h + z))/\cosh(k_n h)$, where h denotes water depth. A detailed derivation of Eq. (2.14) can be found in [20]. The notation $\{\}_n$ on the right hand side of Eq. (2.14) is due to the nonlinear coupling (triad interactions) between component n and two other spectral components (l and m). Using Eq. (2.14) along with time-harmonic wave behavior, i.e.

$$\tilde{\phi_n}(x, y, t) = \frac{\hat{\phi_n}(x, y)}{2} e^{-i\omega_n t} + \frac{\hat{\phi_n^*}(x, y)}{2} e^{i\omega_n t} \quad (2.16)$$

and using the definition of resonant triad interactions (to define a relationship between l, m and n)

$$\omega_n = \pm\ \omega_l \pm \omega_m \tag{2.17}$$

Kaihatu and Kirby [20] obtained the following nonlinear elliptic model:

$$\begin{aligned}
&\nabla_h \cdot [(CC_g)_n \nabla_h \hat{\phi_n}] + k_n^2 (CC_g)_n \hat{\phi_n} \\
&\qquad = -\frac{i}{4}\left[\sum_{l=1}^{n-1} 2\omega_n \nabla_h \hat{\phi}_l \cdot \nabla_h \hat{\phi}_{n-l} + \omega_{n-l}\hat{\phi}_{n-l}\nabla_h^2\hat{\phi}_l\ + \omega_l \hat{\phi}_l \nabla_h^2 \hat{\phi}_{n-l}\right. \\
&\qquad\qquad \left. + \frac{\omega_l \omega_{n-l}\omega_n}{g^2}(\omega_l^2 + \omega_l\omega_{n-l} + \omega_{n-l}^2)\hat{\phi}_l\hat{\phi}_{n-l}\right] \\
&\qquad - \frac{i}{2}\left[\sum_{l=1}^{N-n} 2\omega_n \nabla_h \hat{\phi}_l^* \cdot \nabla_h \hat{\phi}_{n+l} - \omega_l \hat{\phi}_l^* \nabla_h^2 \hat{\phi}_{n+l} + \ \omega_{n+l}\hat{\phi}_{n+l}\nabla_h^2\hat{\phi}_l^*\right. \\
&\qquad\qquad \left. - \frac{\omega_l\omega_{n+l}\omega_n}{g^2}(\omega_l^2 - \omega_l\omega_{n+l} + \omega_{n+l}^2)\hat{\phi}_l^*\hat{\phi}_{n+l}\right]
\end{aligned} \tag{2.18}$$

The above equation (or the ENMSE) can be seen as the second-order nonlinear extension of the standard elliptic mild-slope equation of Berkhoff et al. [1]. The right hand side in Eq. (2.18) contains quadratic nonlinear terms (hereafter referred to as $QNLs$). The same equation, in non-dimensional form, was derived separately by Tang and Ouellet [21]. As noted earlier, the parabolic approximation has been used in the past to obtain solutions; here we simulate nonlinear wave transformation using the complete and more general ENMSE.

It is noted that the ENMSE is a system of nonlinear, second-order (both in x and y), elliptic partial differential equations and requires conditions on all boundaries. Therefore, the physical characteristics of the ENMSE differ from the parabolic models, which require no conditions on the "downwave" boundary. As a result, it requires a different iterative procedure for the linearization (for numerical solution purposes) of the nonlinear problem. In parabolic models, the solution marches from one row

to the next, and solutions on the previous row are used to estimate the nonlinear terms. Sometimes, for greater accuracy, the nonlinearities are "centered" between the current row and the row for which the solution is sought; then, "estimates" of the solution on the latter row are needed, resulting in an iterative process [21]. In elliptic models, the solution over the entire domain is obtained at the same time, and the standard iterative procedure used to handle nonlinear mechanisms (e.g. wave breaking in [7], wave-current interactions in [6]), requires all nonlinear parameters to be predetermined (i.e. the equation is "linearized") at all grid points based on the previous iteration. This is somewhat comparable, in principle, to the latter scheme used for parabolic approximations. However, even in the case of breaking, Zhao et al. [7] found that this approach needed adjustment: a solution with no breaking created large wave heights in shallow regions, which resulted in excessively large estimates for the breaking parameters. As a result, the following solution yielded very small wave heights, which led, in the following round, to (nearly) no breaking and large wave heights, and eventually to an oscillating pattern. They resorted to averaging the solutions to estimate the nonlinearities.

Obviously, the success of any iterative procedure depends on the magnitude of the nonlinearities. To gage the likelihood of success of this general approach, the one-dimensional form of ENMSE is used for a preliminary investigation. The one-dimensional nonlinear equation, along with boundary conditions, was solved using second-order finite differences. (Details regarding the boundary conditions are included in Section 2.3). It was found that the ENMSE, when solved using the nonlinear iterative procedure, encounters convergence problems even for the simple problem of wave decomposition (into different harmonics) over a flat bottom (viz. the wave tank experiments of Chapalain et al. [16]). The ENMSE failed to converge and provide a stable solution. For this particular problem, analysis revealed that the

convergence issue is most probably an artifact of the iterative procedure. For an aid to comprehension, the modeled amplitudes of the four harmonics at the first and third iteration are shown in Fig. 2.2. During the first step of the iterative procedure, the $QNLs$ are assumed zero, and the systems of equations is solved to obtain linear "approximation" (see Fig. 2.2) of $\hat{\phi}_n$. In the second step, the linear solution is used to calculate $QNLs$, and the resulting boundary value problem is solved for the next set of approximate solutions. However, in the third iteration, the $QNLs$ for the first harmonic, both analytically as well as numerically, are found to oscillate at a spatial frequency of k_1, which is exactly equal to the natural frequency of the first harmonic (plots not shown for brevity). This resembles a resonance-like situation in harmonic systems, and the solution for the first harmonic increases linearly with distance along the wave tank (see Fig. 2.2) while other harmonics grow through wave interaction effects. This increase is clearly nonphysical, since the total energy of the system should be conserved. As a consequence, the solution diverges within the next few iterations due to the incompatibility of the iterative scheme with the ENMSE.

To overcome this problem, either the above boundary-value problem must be solved with a modified iterative procedure, or some suitable alterations must be introduced in the governing equation Eq. (2.18). For this study, we consider latter approach and derive an alternative equation in the following section.

2.3.1 An Alternative Approach

An alternative equation is derived from Eq. (2.5) by applying multiple-scale analysis, a perturbation technique used as a tool for solving weakly nonlinear problems. In the framework of mild-slope equation based models, Li [58] used this approach to derive an alternative (evolution-type) form of linear elliptic mild-slope equation. Following Li [58], we introduce a slow time variable $\bar{t} = \varepsilon t$ so that the complex veloc-

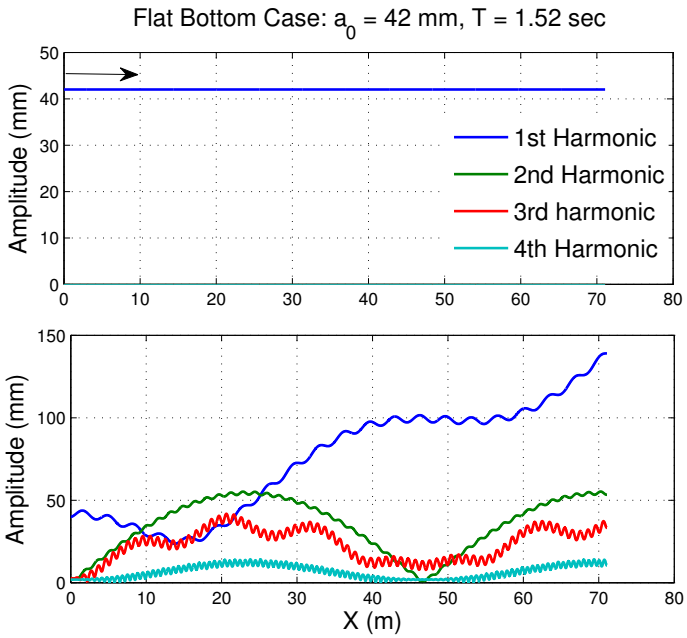

Figure 2.2: Convergence issues with ENMSE. (Top) Modeled amplitudes at first iteration, and (b) modeled amplitudes at third iteration.

ity potential function in Eq. (2.5) now also depends on the slow variable $\bar{t}$ as follows:

$$\tilde{\phi}_n(x,y,t,\bar{t}) = \frac{\hat{\phi}_n(x,y,\bar{t})}{2} e^{-i\omega_n t} + \frac{\hat{\phi}_n^*(x,y,\bar{t})}{2} e^{i\omega_n t}. \tag{2.19}$$

Given two distinct time scales t and $\bar{t}$, the derivatives with respect to t (e.g [57]) in Eq. (2.5) must now be replaced by

$$\frac{\partial}{\partial t} \rightarrow \frac{\partial}{\partial t} + \varepsilon \frac{\partial}{\partial \bar{t}} \tag{2.20}$$

and

$$\frac{\partial^2}{\partial t^2} \rightarrow \frac{\partial^2}{\partial t^2} + 2\varepsilon \frac{\partial^2}{\partial t \partial \bar{t}} + \varepsilon^2 \frac{\partial^2}{\partial \bar{t}^2}. \tag{2.21}$$

Note that in comparison to the derivation by Li [58], Eq. (2.5) contains additional complex nonlinear terms on the right-hand side which require careful treatment. By

incorporating the definition of resonant triad interactions, we obtain a nonlinear equation of the form

$$-\varepsilon^2\frac{\partial^2\hat{\phi}_n}{\partial\bar{t}^2}+2i\varepsilon\omega_n\frac{\partial\hat{\phi}_n}{\partial\bar{t}}+\nabla_h\cdot[(CC_g)_n\nabla_h\hat{\phi}_n]+k_n^2(CC_g)_n\hat{\phi}_n$$
$$=\{QNLs\}_n+\{HOTs\}_n \tag{2.22}$$

where, coincidentally, the derivation yields nonlinear terms on the RHS which are identical to the ones described previously, and $HOTs$ represent the higher-order terms in $O(\varepsilon^2)$ or higher. Ignoring all the small terms of $O(\varepsilon^2)$ and higher and, for convenience, replacing $\bar{t}$ by t results in

$$2i\omega_n\frac{\partial\hat{\phi}_n}{\partial t}+\nabla_h\cdot[(CC_g)_n\nabla_h\hat{\phi}_n]+k_n^2(CC_g)_n\hat{\phi}_n=\{QNLs\}_n \tag{2.23}$$

which is an evolution-type nonlinear mild-slope equation that, in the linear case ($N=1$ and $QNLs=0$), reduces to the evolution equation derived by [58]. Note that Eq. (2.23) represents a system of N coupled nonlinear, parabolic partial differential equations (parabolic in the sense of the two-dimensional heat equation), but it does not inherit the limitations of the parabolic approximation of the elliptic mild-slope equation. In fact, the steady-state form of Eq. (2.23) returns Eq. (2.18), and when marched to steady state, Eq. (2.23) should provide a simulation of all desired phenomena such as wave reflection, diffraction, refraction, wave-wave interaction, etc. In addition, Eq. (2.23) should be considered as a pseudo time-dependent equation which is different from hyperbolic time-dependent models (e.g. [54, 59]).

2.3.2 Surface Elevation

From linear theory, the first-order dynamic free-surface boundary condition

$$\Phi_t+g\eta=0 \tag{2.24}$$

may be used to estimate the resultant time-dependent surface profile η using

$$\eta(x,y,t) = \sum_{n=1}^{N} A_n(x,y)e^{-i\omega_n t} + CC \tag{2.25}$$

where $\hat{\phi}_n$ is the steady-state wave potential solution for n^{th} frequency component, and A_n is the corresponding complex wave amplitude expressed as

$$A_n(x,y) = \frac{i\omega_n}{g}\hat{\phi}_n(x,y). \tag{2.26}$$

With nonlinear parabolic mild-slope models, it is noted that [20, 70] the first-order approximation may lead to underestimation of wave energy transfer at higher frequencies. A second-order correction for parabolic models was therefore derived by Kaihatu [71]. Here, to derive a similar correction for the present model, we use the second-order dynamic free-surface condition

$$\eta = -\frac{1}{g}\Phi_t - \frac{1}{2g}(\nabla_h\Phi)^2 - \frac{1}{2g}(\Phi_z)^2 + \frac{1}{g}\Phi_t\Phi_{zt} \tag{2.27}$$

and follow Kaihatu's procedure to obtain a corrected expression for surface profile η in the form:

$$\eta(x,y,t) = \sum_{n=1}^{N} B_n(x,y)e^{-i\omega_n t} \tag{2.28}$$

where B_n is the corrected wave amplitude for n^{th} harmonic given by

$$\begin{aligned} B_n(x,y) = A_n(x,y) \\ - \frac{1}{4g}\left[\sum_{l=1}^{n-l} \nabla_h\hat{\phi}_l \cdot \nabla_h\hat{\phi}_{n-l} + \frac{\omega_l\omega_{n-l}}{g^2}(\omega_l^2 + \omega_l\omega_{n-l} + \omega_{n-l}^2)\hat{\phi}_l\hat{\phi}_{n-l}\right] \\ + \frac{1}{2g}\left[\sum_{l=1}^{N-n} \nabla_h\hat{\phi}_l^* \cdot \nabla_h\hat{\phi}_{n+l} - \frac{\omega_l\omega_{n+l}}{g^2}(\omega_l^2 - \omega_l\omega_{n+l} + \omega_{n+l}^2)\hat{\phi}_l^*\hat{\phi}_{n+l}\right] \end{aligned} \tag{2.29}$$

in which the second and the third terms on the right-hand side, which physically represent the effect of triad interactions, arise from second-order terms in Eq. (2.27).

Note that the definition of resonant triad interactions has also been utilized in the derivation of Eq. (2.29) so that it is consistent with Eqs. (2.18) and (2.23).

The numerical modeling of Eq. (2.23) using finite difference method, the improved convergence properties of Eq. (2.23), and the preliminary invesstigation of this equation are discussed in the next chapter.

3. PRELIMINARY INVESTIGATION USING FINITE DIFFERENCE MODEL

3.1 Finite Difference Model

To perform a preliminary investigation of the nonlinear equation, and to establish a new method for boundary treatment, a finite difference model based on Alternating Direction Implicit (ADI) scheme is developed. a discussion regarding The solution procedure using this scheme, the boundary treatment method, and the investigation of the model using a variety of test cases is presented in the subsequent sections.

3.1.1 Solution Procedure

Li [58] used the ADI scheme to solve an evolution-type mild-slope equation (the linearized form of Eq. (2.23)). A schematic of the ADI scheme is shown in Fig. 3.1. The finite difference discretization of the nonlinear equation in Eq. (2.23) for two sweeps of the ADI scheme are given by:

$$-2i\omega\left(\frac{\hat{\phi}_{i,j}^{n+1/2}-\hat{\phi}_{i,j}^{n}}{\Delta t/2}\right)+\left(CC_g\right)_{i,j}\delta_x^2\hat{\phi}_{i,j}^{n+1/2}+\frac{1}{2}k_{i,j}^2\hat{\phi}_{i,j}^{n+1/2}$$
$$+\left(CC_g\right)_{i,j}\delta_y^2\hat{\phi}_{i,j}^{n}+\frac{1}{2}k_{i,j}^2\hat{\phi}_{i,j}^{n}+\delta_x\hat{\phi}_{i,j}^{n+1/2}\delta_x\left(CC_g\right)_{i,j}+\delta_y\hat{\phi}_{i,j}^{n}\delta_y\left(CC_g\right)_{i,j}=0$$

$$-2i\omega\left(\frac{\hat{\phi}_{i,j}^{n+1/2}-\hat{\phi}_{i,j}^{n}}{\Delta t/2}\right)+\left(CC_g\right)_{i,j}\delta_x^2\hat{\phi}_{i,j}^{n+1/2}+\frac{1}{2}k_{i,j}^2\hat{\phi}_{i,j}^{n+1/2}$$
$$+\left(CC_g\right)_{i,j}\delta_y^2\hat{\phi}_{i,j}^{n+1}+\frac{1}{2}k_{i,j}^2\hat{\phi}_{i,j}^{n+1}+\delta_x\hat{\phi}_{i,j}^{n+1/2}\delta_x\left(CC_g\right)_{i,j}+\delta_y\hat{\phi}_{i,j}^{n+1}\delta_y\left(CC_g\right)_{i,j}=0$$

where

$$\delta_x^2\hat{\phi}_{i,j}^{n}=\frac{\hat{\phi}_{i-1,j}^{n}-2\hat{\phi}_{i,j}^{n}+\hat{\phi}_{i+1,j}^{n}}{\Delta x^2}$$

$$\delta_y^2\hat{\phi}_{i,j}^{n}=\frac{\hat{\phi}_{i,j-1}^{n}-2\hat{\phi}_{i,j}^{n}+\hat{\phi}_{i,j+1}^{n}}{\Delta y^2}$$

Importantly, in both sweeps of the ADI scheme, a tri-diagonal system of equations is formed which can effectively be solved using the very efficient Thomas algorithm. This obviates the need to store large matrices and related issues that arise in the solution of elliptic systems (see the review by Panchang and Demirbilek [11]). Li [58] showed, using von Neumann's stability analysis, that the numerical scheme is unconditionally stable for linear problems and has second-order accuracy both in time and space. Following Li [58], the ADI scheme with finite-difference method is used for this study, and the domain is descretized using regular grids with uniform spacing in each direction. However, the nonlinear terms, which make the equation non-homogeneous, can create some restrictions on the time-steps, possibly if the nonlinear changes imposed on the scheme between time-steps are large.

To resolve nonlinearities, we start with an initial guess, $\hat{\phi}_n = 0$ say, at $t = 0$. For the linearization of the problem in a numerical sense, the $QNLs$ at the grid points are calculated using the solution obtained at the previous step. The derivative terms in the $QNLs$ are calculated using second-order finite differences, and the discretization of the linear part using ADI scheme is same as given in [58]. The marching process continues until the steady-state is achieved for all frequency components under consideration. Unlike nonlinear elliptic models (e.g. [7]) where one first obtains a linear solution and then performs iterations to get the final nonlinear (e.g. with breaking) solution, here we simply march in time. There are no iterations involved between two successive time steps. $QNLs$ at a particular time-step are calculated using the solution at previous time step.

In order to handle nearshore applications, a dissipative breaking mechanism may be added in the governing equation. The formulas for the nonlinear breaking mechanism are provided in later Section 4.2, however the breaking parameter also depends on the wave height (to be calculated). Thus, breaking compounds the nonlinear

complications of the present model. However, no special treatment is needed. In fact, at each step of the marching process, both the $QNLs$ and the breaking factor are updated simultaneously using the solution at previous step, which makes the process efficient.

3.1.2 Boundary Treatment

To complete the boundary value problem, two types of boundary conditions, similar to those used with linear models discussed in Chapter 2, may be considered: (1) along physical boundaries such as structures and coastlines, characterized as fully or partially reflecting, and (2) along artificial open-ocean boundaries intended to be fully transmitting to incident and outgoing scattered waves. Most engineering applications, as shown in Fig. 3.2, may be categorized either as open-sea problems where the modeled domain is surrounded all over by artificial open-ocean boundaries (ABCDA in Fig. 3.2), or coastal/harbor applications where artificial open-ocean boundaries (HIEF in Fig. 3.2) are connected to shoreline or harbor boundaries (FGH).

For evolution type mild-slope models, Li [58] concluded that the boundary conditions typically used with elliptic models can be successfully used with evolution type models. Therefore they were first examined for the case of wave propagation over a flat bottom, including decomposition into higher harmonics, as studied by [16]. The boundary conditions usually used with elliptic models [11, 60, 61] consist of approximate representations of incoming waves and outgoing waves, and combinations of these on some boundaries. While this approach provided a reasonable match to the data of Chapalain et al. [16], some spurious oscillations were seen in the results (see Fig. 3.3). Experiments showed that the magnitude of the oscillations depended on the location of the boundaries; they appeared to diminish if the boundaries were

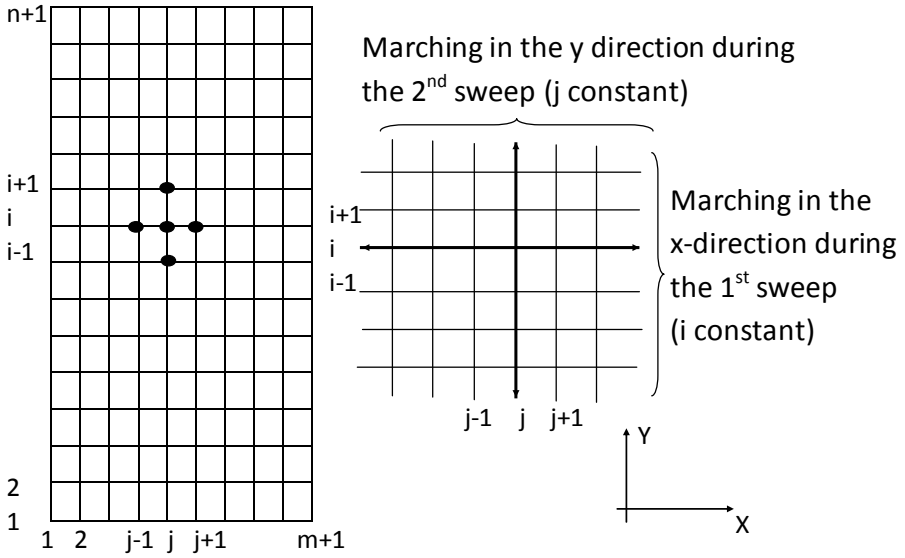

Figure 3.1: A schematic of ADI scheme.

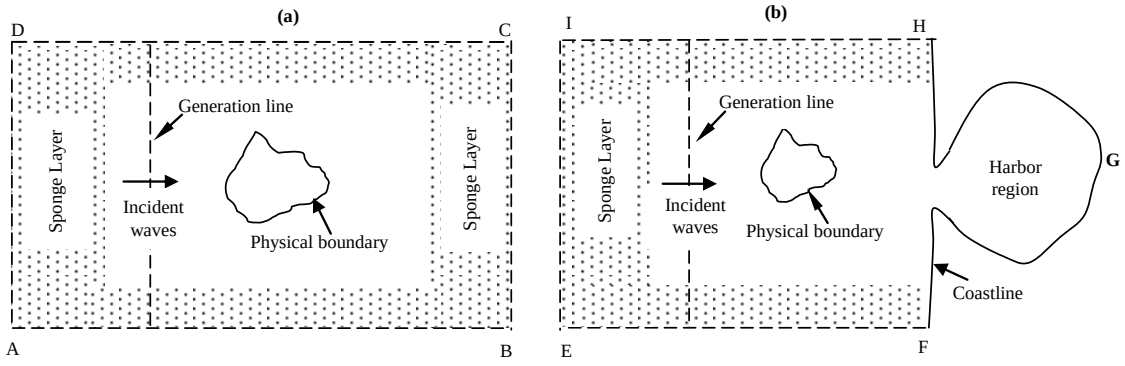

Figure 3.2: Definition sketch of computational domain. (a) Open-sea problem; (b) coastal/harbor problem.

placed, fortuitously, near locations where the magnitude of the higher harmonics was negligibly small (i.e. at the quasi-sinusoidal nodes, where, as discussed by [16], the

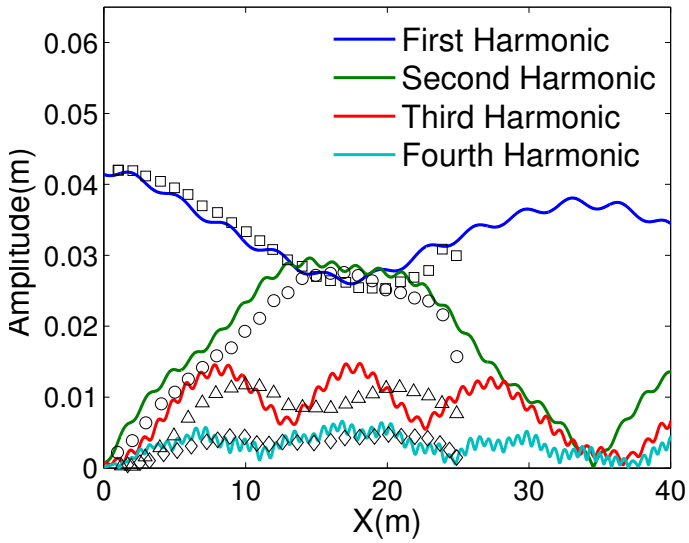

Figure 3.3: Definition sketch of a typical wave model domain

.

wavefield is almost linear (sinusoidal)). Of course, in general problems, such locations are not known *a priori*. These oscillations were attributed to the separation of the wave components inherent in this treatment of the boundaries, and resulting problems can be expected to be even more pronounced for other complex applications.

To preserve the generality of the present nonlinear model, we considered the option of supplementing the linear boundary conditions with a sponge layer, which can substantially dissipate wave energy near domain boundaries, so that spurious wave reflections can be minimized. Sponge layers have largely been used in nonlinear Boussinesq models [18, 62], and with hyperbolic mild-slope models in some instances (e.g. [59, 63]). For our purposes, an extension of Eq. (2.23) is derived. Starting from the time-dependent, two-equation model of [54] which accounts for dissipative sponge layer, we first derive a hyperbolic mild-slope model by following the standard

procedure given in [59]. The hyperbolic model is then converted to the evolution-type model by factoring out time-harmonicity and introducing the slowly-varying time variable discussed earlier. This leads to:

$$2i\omega_n \frac{\partial \hat{\phi}_n}{\partial t} + \nabla_h \cdot [(CC_g)_n \nabla_h \hat{\phi}_n] + k_n^2 (CC_g)_n \hat{\phi}_n + i\omega_n D \hat{\phi}_n = \{QNLs\}_n \quad (3.1)$$

where the last term on the left hand side of Eq. (3.1) is due to the dissipative sponge layer. The dissipation factor D for a given x inside the layer is assumed to be:

$$D = C_1 \frac{exp\left[(|x - x_s|/|x_e - x_s|)^{C_2}\right] - 1}{exp(1) - 1} \quad (3.2)$$

where x_s and x_e are the coordinates of starting and ending points of the sponge layer region, and , C_1 and C_2 are application-dependent coefficients. The width of sponge layer is generally 1.5-2.0 times the wavelength of the smallest (or primary) frequency component [18, 64]. Usually sharp variations in the dissipation factor inside the layer may send spurious backscattered waves into the domain. Therefore, coefficients C_1 and C_2 for a particular application are selected in a manner that spurious reflection and/or diffraction effects due to wave propagation inside the layer do not affect the solutions in the region of interest. In most cases, this can be ascertained by simulating the performance of sponge layers for the smallest (or primary) frequency component by using the linear version of Eq. (3.1).

The performance of the sponge layers is examined using flat bottom case of [16] mentioned earlier. The results shown in Fig. 3.4 are now devoid of small-scale spurious oscillations and compare well with the laboratory data for all the four modeled harmonics.

Note that it is straightforward to implement sponge layers along the downwave and lateral boundaries of the domain. Along the upwave boundary, a sponge layer will not only suppress the outgoing waves but also the specified incident waves.

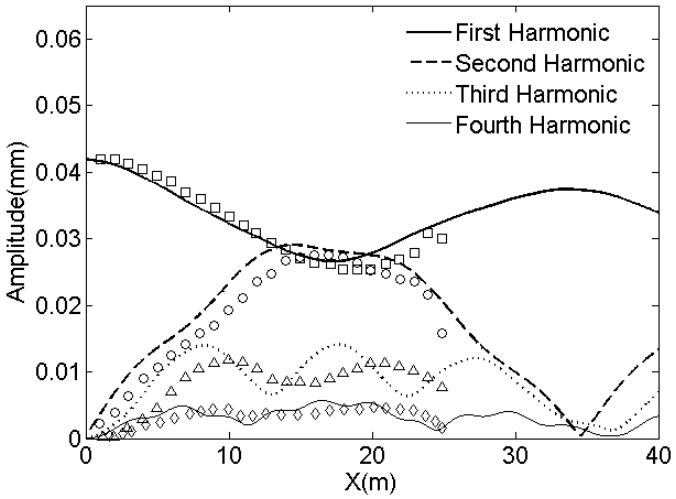

Figure 3.4: Improved modeled results with sponge layer along downwave boundary. Markers represent experimental data of Chapalain et al. [16].

Therefore, its use necessitates a mechanism for the internal generation of waves with Eq. (2.24).

Internal wave generation is mostly limited to time-dependent models (e.g. [54, 18, 62, 65, 66]). Two types of methods, the source function method and the line (delta) source method, have been used successfully; however, Kim et al. [67] reported that the line source method may produce noisy solutions with some equations. For linear elliptic models, extensions for the source function method [68] and the line source method [69] are derived and used for regular waves. Following the tedious but straightforward derivation procedure given in [68], we obtain an extension of Eq. (2.24) which has an additional (source) term $\{S\}_n$ added to the $\{QNLs\}_n$ on the right-hand side. For nonlinear problems, the source function may be needed for all frequency components under consideration, and its expression for the n^{th} frequency component is

$$S(x,y) = D_n exp\left[-\gamma(x-x_i)^2\right] \tag{3.3}$$

where parameter γ is related to the width of source function; x_i denotes the center coordinate of source region; and the magnitude D_n of the source function for n^{th} frequency component is calculated using

$$D_n = \frac{2A_{in}\omega_n}{\sqrt{\frac{\pi}{\gamma}} exp\left(\frac{-k_n^2}{4\gamma}\right)} \tag{3.4}$$

where A_{in} is the incident wave amplitude for n^{th} frequency component. The factor of 2 in Eq. (3.3) accounts for two-way wave generation. The component that travels toward the upwave boundary is dissipated together with the outgoing scattered waves generated inside the modeling region.

Numerical simulations were performed to obtain criteria for the selection of γ. In general, γ should be selected in a way that the width of the source function is as small as possible; however, a sufficient number of grid points is always needed to properly resolve the source region. For the present model, we recommend γ in the range of $80/\lambda^2$ to $320/\lambda^2$ which implies a source region width of 0.25λ to 0.5λ where λ is the wavelength. This range for γ is similar to one used in Boussinesq models [62, 18] with a slightly different approach for internal wave generation. Unlike linear problems which appeared less sensitive to γ values, for nonlinear problems, erroneous contributions to the $QNLs_n$ due to nonlinear interactions inside the source region should be minimized by selecting an appropriate value of γ. (See Section 3.1 for more details). These criteria are used in all cases considered later in this paper.

3.2 Model Validation

A variety of tests which cover many practical situations usually encountered in coastal/harbor engineering applications are considered. By way of preliminary testing, the model was verified (with $QNLs = 0$) for linear problems for which analytical/other solutions are known. Good agreement is found between modeled results

and analytical solutions, and the computational scheme (ADI) is found to be efficient for these linear problems. Results for these linear problems are not shown for brevity.

Four additional tests are selected from the literature for data-model or inter-model comparisons, and also to verify the performance of various model features such as sponge layers, internal wave generation, nonlinear wave breaking, etc. The tests involve: (1) the combined effects of wave reflection and wave-wave interactions in the vicinity of a submerged shelf (breakwater); (2) the transformation of a wave spectrum (from deep to shallow water) due to nonlinear wave shoaling and breaking over a plane sloping beach; (3) nonlinear refraction and diffraction effects with the generation of higher harmonics in two dimensions; and (4) nonlinear harbor resonant interactions, i.e. harbor resonance in the presence of resonant triad interactions, which is a particularly demanding test.

3.2.1 Waves around Submerged Breakwater

Wave reflection in the presence of structures may significantly alter the nature of the wave-field. One of the main features of the present model, as discussed earlier, is to simultaneously handle wave back-scattering and nonlinear interactions. Experimental data and numerical results [72] from a fully-nonlinear x-z plane model are available for validation. Besides the generation of higher harmonics, a high degree of backscattering renders this a good test for the effectiveness of the internal wave generation and the sponge layers as described earlier. Note that the internal wave generation method has not been exercised with nonlinear mild-slope models in the past. In particular, with nonlinear parabolic mild-slope models, the upwave boundary treatment is much simpler, because the wave-field is expected to be predominantly progressive. The experimental setup together with the configuration of submerged shelf is shown in Fig. 3.5. The submerged shelf has steep sides (slope

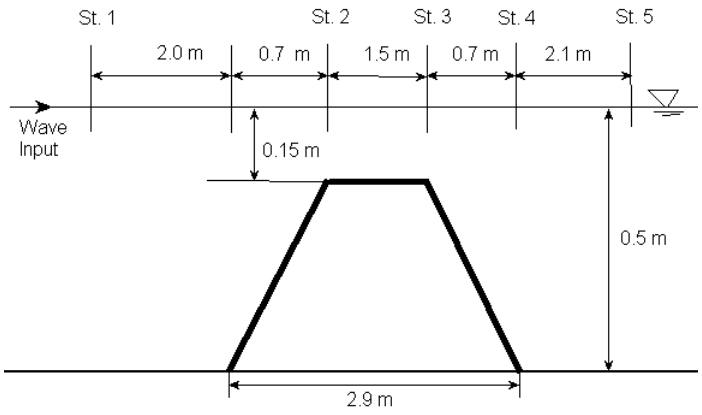

Figure 3.5: Experimental setup of Ohyama et al. [72].

1:2) that cause waves to reflect back. In the shallow region over the shelf, nonlinear interactions become prevalent and higher harmonics are generated. These harmonics then travel towards the downwave boundary where the linear boundary condition is used together with a sponge layer. The sponge layer, which is 1.5 times as wide as the wavelength (= 2.42 m) of the fundamental harmonic ($T = 1.34$ s), absorbs most of the wave energy and minimizes undesired wave oscillations caused by the linear boundary condition. The incident harmonics are generated inside the domain along a wave generation line located at the wavemaker position ($X = -28.3$ m) in the experiments. The higher harmonics are assumed to have zero input wave amplitude at the generation line. Although this case contains no variations in the $y-$direction, the two-dimensional model developed here was used. A 1200 X 4 grid ($\Delta x/L_{min}$ = 0.08 and $\Delta y/L_{min} = 0.50$) was used along with a "time" step of $\Delta t/T_{min}$ =0.80 where L_{min} is the minimum wavelength (near wavemaker region) and T_{min} is the minimum period among all the harmonics under consideration; about 1200 steps are required to obtain steady-state solution which takes approximately 17 s to finish on a 3.33 GHz single-processor computer with 4 GB RAM.

The spatial variation of three harmonics for Case 2 ($A_{i1} = 0.025$ m) from Ohyama et al. [72] is shown in Fig. 3.6, along with their data and their fully nonlinear model (an $x - z$ plane potential-flow based model which is theoretically more accurate than the present second-order nonlinear model). The results obtained with the present model correlate reasonably well with the fully nonlinear model results and also with the experimental data. Significant wave back-scattering on the upwave side of the shelf can be observed in all the plots shown in Fig. 3.6.

Results are presented for different values of γ to understand the significance of correctly selecting γ to ensure the accuracy of the modeled results. Based on the criteria discussed in Section 2.3, all values of γ in the range of 13.0 to 54.0 are found to produce satisfactory results. Sample results for $\gamma = 25$ are shown in Fig. 3.6(a) and Fig. 3.6(b). Good agreement is observed between modeled results for $\gamma = 25$ and the fully-nonlinear model results (see Fig. 3.6(b)). However, for a value outside the range (i.e. $\gamma = 2$), the large width of the source function (not shown here) near the wave generation line causes spurious nonlinear interactions near the generation line ($X = -28.3$ m in Fig. 3.6(a)) and consequently affects the overall model results. The results (for the three harmonics) shown with dashed line in Fig. 3.6(a) are quite different from the fully-nonlinear model results.

3.2.2 Spectral Transformation over Sloping Beach

Depth-induced wave breaking and shoaling, especially in shallow regions with prevalent near-resonant interactions, play a critical role in nearshore wave transformation. To investigate the present model's ability to simulate nearshore wave environment, we consider Case 2 in [73] which has been used by researchers (e.g. [20, 74]) to understand breaking and shoaling properties of irregular waves, and also to verify their numerical models. For this case, the incident wave condition is ob-

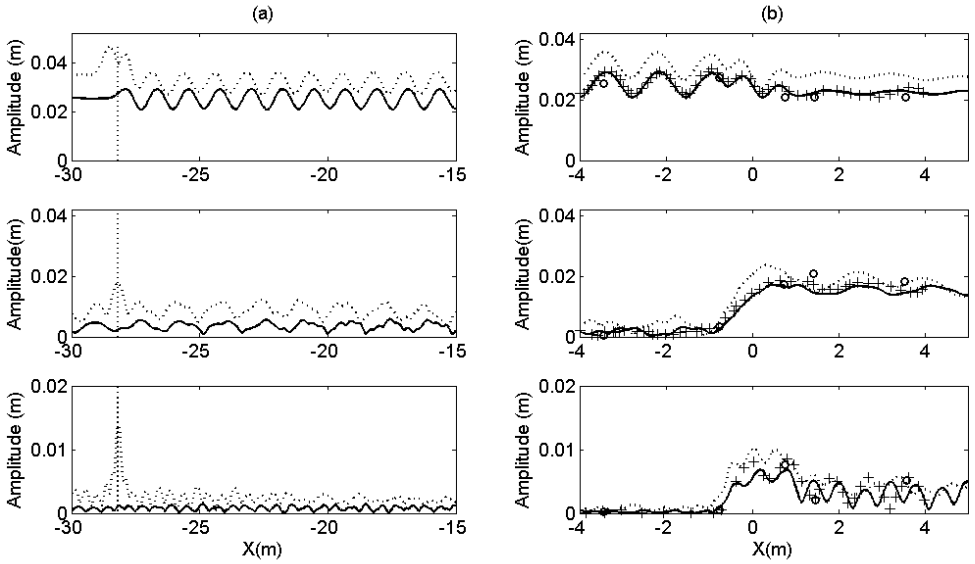

Figure 3.6: (a) Modeled amplitudes near internal generation line $X = -28.30$ m. (b) Comparison of modeled amplitudes with data near submerged shelf. Present model with $\gamma = 2$ ($\cdots$); present model with $\gamma = 25$ (—); data form Ohyama et al. [72] ($\circ\,\circ$), and fully-nonlinear model (++). (Top) First harmonic; (middle) second harmonic; (bottom) third harmonic.

tained using a Pierson-Moskowitz-type spectrum with a peak frequency of 1 Hz in deeper ($h = 0.47$ m) portion of the tank. The experimental setup with a sloping bottom is shown in Fig. 3.7.

With regards to Case 2, Kaihatu and Kirby [20] concluded that most shallow water models over-predict shoaling approximately at all frequencies; because, the peak frequency of the input spectrum corresponds to $kh = 1.96$, which lies outside the range of applicability of shallow water models. Their nonlinear parabolic mild-slope model, with linear characteristics of a fully-dispersive model, provided results that depict good agreement with the experimental data. With no significant wave reflection and diffraction effects, and with the same dispersive characteristics as the nonlinear parabolic mild-slope model, we anticipate the present model to replicate

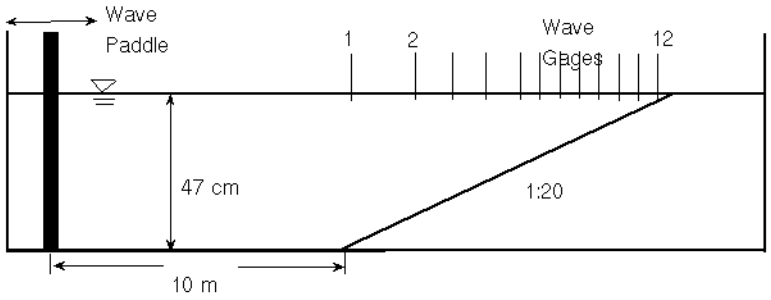

Figure 3.7: Experimental setup of experiments of Mase and Kirby [73].

a similar agreement. However, Case 2 is more demanding and challenging for the present model as it uses a completely different and more complex solution procedure in comparison to the parabolic model. The input wave spectrum is truncated to contain frequencies in the range 0 to 2.5 Hz. A total of 255 frequency components are considered, and higher frequencies with little energy are ignored. A sponge layer along the downwave boundary is optional here, because the amplitudes become small at this boundary due to breaking dissipation. The present two-dimensional model is used with a 2000 X 3 grid ($\Delta x/L_{min} = 0.04$ and $\Delta y/L_{min} = 1.0$) and a "time" step of $\Delta t/T_{min}$ =0.08; to obtain steady-state solution, about 8000 steps are required which takes around 2.5 h to finish on the same computer mentioned earlier. We note that the model given by Eq. (2.23) does not include a dissipative mechanism to account for wave breaking; therefore, following [20], we revise Eq. (2.23) to include a dissipation mechanism as follows:

$$2i\omega_n \frac{\partial \hat{\phi}_n}{\partial t} + \nabla_h \cdot [(CC_g)_n \nabla_h \hat{\phi}_n] + ik_n (CC_g)_n \alpha_n \hat{\phi}_n + k_n^2 (CC_g)_n \hat{\phi}_n = \{QNLs\}_n \quad (3.5)$$

where the third term on the left hand side in Eq. (3.5) is due to breaking dissipation, and

$$\alpha_n = \alpha_{n0} + \left(\frac{f_n}{f_{peak}}\right)^2 \alpha_{n1}, \quad (3.6)$$

$$\alpha_{n0} = F\beta(x), \tag{3.7}$$

$$\alpha_{n1} = (\beta(x) - \alpha_{n0}) \frac{f_{peak}^2 \sum_{n=1}^{N} |A_n|^2}{\sum_{n=1}^{N} f_n^2 |A_n|^2}, \tag{3.8}$$

$$\beta(x) = \frac{3\sqrt{\pi}}{2\sqrt{g}h} \frac{B^3 f_{peak} H_{rms}^5}{\gamma_0^4 h^5}, \tag{3.9}$$

$$H_{rms} = 2\sqrt{\sum_{n=1}^{N} |A_n|^2}, \tag{3.10}$$

where f_{peak} is the peak spectral frequency; f_n is the n^{th} frequency; $\beta(x)$ is a probabilistic decay function which defines the depth dependence of breaking dissipation, and was developed by [75]. Note that for this mechanism to be consistent with the present model, the dissipation factor $\beta(x)$ in [20] has been multiplied by a factor of 2. Parameters B and γ_0 are set to 1 and 0.6 respectively. F is a weighting factor; $F = 0.0$ indicates uniform dissipation over all frequencies, whereas, $F = 1.0$ (used here) allows frequency-squared weighted dissipation. More details about the dissipative mechanism can be found elsewhere [75, 71]. The primary objective here is to include a dissipative mechanism in the present model. Note that in the category of mild-slope models, this type of dissipative mechanism (based on the frequency-squared weightage) has hitherto been exercised only with parabolic models.

The modeled spectral transformation of the input wave spectrum due to nonlinear energy transfer between frequency components is shown in Fig. 3.8. In these plots, results are compared with the experimental data at three wave-gauges located in deep (47 cm), intermediate (20 cm), and shallow (5 cm) water depth. The present model is able to capture most of the salient features of deep-to-shallow water transformation observed in the experimental results. For example, the peak-frequency shift toward a lower frequency, the reduction in the wave energy near the peak frequency region,

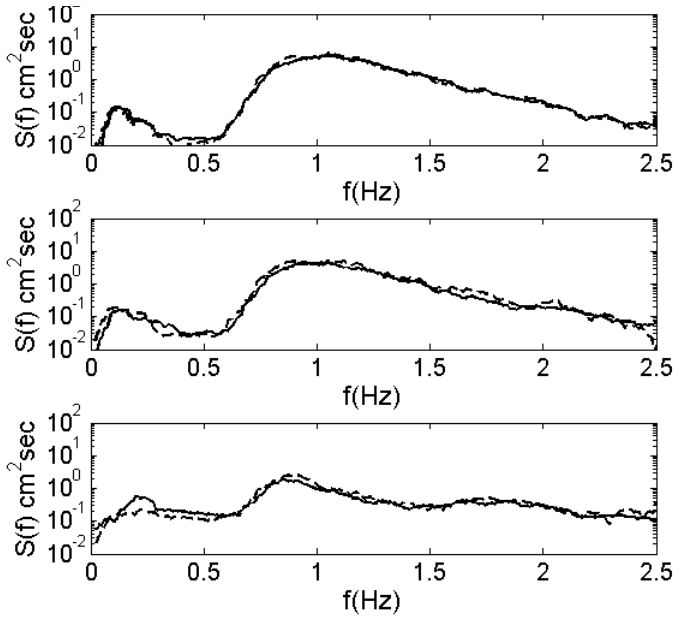

Figure 3.8: Comparison of wave spectrum for Case 2 of Mase and Kirby [73]. Experimental data (- - -) and modeled results (—) for $h = 47$ cm (top), $h = 20$ cm (middle), and $h = 5$ cm (bottom).

and the increase in wave energy at low and high frequencies, are modeled reasonably well. As expected, the model results are also quite comparable with the nonlinear parabolic model [20] results (not shown here). Overall the results in Fig. 3.8 detail the effectiveness of the breaking model and the numerical iterative procedure with the present model. It is encouraging that the nonlinear breaking model, when used with the present evolution-type model, does not require any modifications in the iterative procedure described earlier. However, nonlinear breaking with linear elliptic mild-slope models, as described by Zhao et al. [7], requires additional iterations which significantly increase computational efforts.

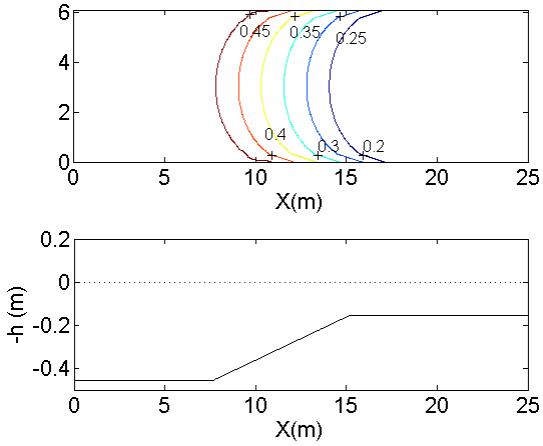

Figure 3.9: Bottom contours (top) and centerline bathymetry (bottom) of Whalin [77].

3.2.3 Wave Propagation over Semicircular Shoal

Whalin [77] performed a series of experiments to study wave-focusing over a slowly varying depth profile. Many researchers (e.g. [78, 74, 79, 20]) have since used Whalin's experimental data to verify their model's capability to simulate nonlinear wave diffraction and refraction with the generation of higher harmonics.

The wave tank used in Whalin's experiments had a length of 25.60 m and a width of 6.10 m. The topography consists of a semicircular shoal (also called a topographic lens) on a slope in the central portion of the tank (Fig. 3.9). Three sets of experiments were conducted by Whalin, by generating waves with periods $T = 1, 2$ and 3 s using a wave-maker situated in the deeper part of the wave tank ($h = 0.46$ m). The present model is applied to all the cases considered by Whalin [77] in his experiments. However, in this paper we only discuss results for the cases included in Table 6.1 (i.e. $T = 1$ and 2 s). The $T = 1$ s case demonstrates the advantages of the present model over the parabolic model of Kaihatu and Kirby [20]. The low

Table 3.1: Input wave parameters for the experiments of Whalin [77]

T (s)	a_0 (cm)	$\varepsilon = ka$	kh
2	1.06	0.0168	0.730
2	1.46	0.0237	0.730
1	0.98	0.0410	1.965
1	1.95	0.0815	1.965

period challenges the assumption of slow spatial variation inherent in the parabolic approximation, which, therefore, could not produce reliable solutions. For $T = 2$ s, we expect the present model to provide results comparable with their parabolic model as there is negligible back-scattering of waves, and the waves propagate mostly along the x-direction.

As in the case of [20, 21], three harmonics for the $T = 2$ s case and two harmonics for the $T = 1$ s case are found to be sufficient. For all numerical simulations, the internal wave generation method is used with the generation line located near $X = 0.0$ m, and a dissipative sponge layer is placed in the offshore region. The free parameter γ, for all simulations, is based on the criteria discussed earlier in Section 2.3. The higher-harmonics are assumed to have zero incident wave amplitude at the generation line. Near the downwave boundary, a dissipative sponge layer is used that forces the waves to dissipate energy and vanish before they interact with the downwave boundary.

Modeled results along the centerline $Y = 3.078$ m for the $T = 2$ s case are compared with experimental data in Fig. 3.10 for $a_0 = 1.06$ cm and in Fig. 3.11 for $a_0 = 1.49$ cm. It can be seen in these plots that the wave-field is roughly linear near the wave-maker boundary; however, due to wave focusing over the shoaling region, the nonlinear interactions become significant and the higher-harmonics start to grow.

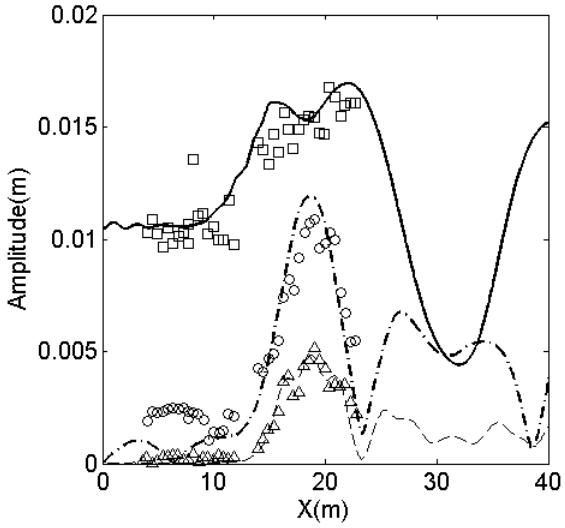

Figure 3.10: Comparison of wave amplitudes along the centerline of the tank for $T = 2.0$ s and $a_0 = 1.06$ cm. Modeled first harmonic (—), second harmonic (- · -), third harmonic (- - -). Data of Whalin [77]: first harmonic (□), second harmonic (o), third harmonic (△).

Whalin [77] also reported a rapid growth of higher-harmonics in the focusing zone. Good agreement is found (especially for $a_0 = 1.06$ cm case) between the modeled results and experimental data for all three harmonics shown in Fig. 3.11. The present model results are nearly identical to those resulting from the parabolic model (not shown here) of Kaihatu and Kirby [20]; this is to be expected, since, as mentioned above, the wave-field is slowly-varying and devoid of significant wave reflection.

Similarly, modeled results and data for $T = 1$ s case are presented in Fig. 3.12 for $a_0 = 0.98$ cm, and in Fig. 3.13 for $a_0 = 1.95$ cm. The high value of the dispersion parameter ($kh = 1.965$) in this case may violate the shallow-water approximation inherent in the conventional Boussinesq models. However, modeled results (for $a_0 = 1.95$ cm) are comparable with the results obtained using higher-order Boussinesq models [80] with improved dispersive characteristics (i.e. valid up to $kh = 6.0$).

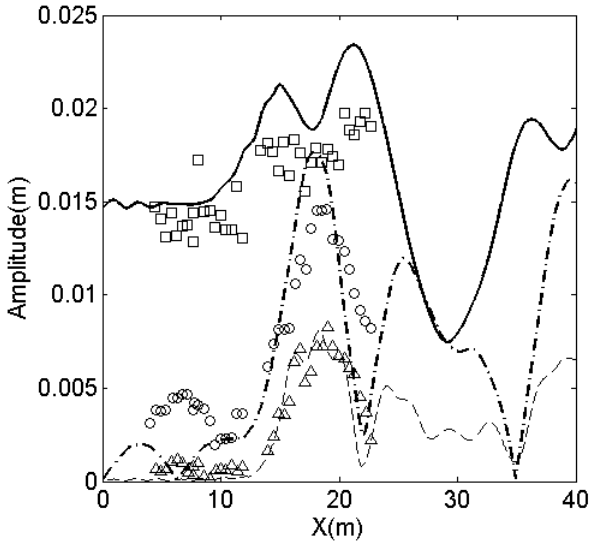

Figure 3.11: Comparison of wave amplitudes along the centerline of the tank for $T = 2.0$ s and $a_0 = 1.49$ cm. Modeled first harmonic (—), second harmonic (- · -), third harmonic (- - -). Data of Whalin [77]: first harmonic (□), second harmonic (o), third harmonic (△).

Note that the oscillating wavefield pattern near the shoaling region for the $T = 1$ s case should not be confused with the spurious oscillations caused by the approximate boundary conditions. It is not possible to conclude from Whalin's data [77] whether these modulations should be present or not; but, according to [79], these oscillations are due to the interactions between bound and free harmonics inside the shoaling region. The results of Liu and Tsay [78], however, do not show such modulations because their model does not allow harmonic interactions. With a 1200 X 40 grid ($\Delta x/L_{min} = 0.33$ and $\Delta y/L_{min} = 0.48$ for $T = 1$ s; $\Delta x/L_{min} = 0.14$ and $\Delta y/L_{min} = 0.22$ for $T = 2$ s) and a "time" step of $\Delta t/T_{min}$ =0.20, a total of 200 and 150 steps are sufficient to achieve steady state for $T = 1$ s and $T = 2$ s, respectively. On the same computer, the computational time for both cases is less than 60 s.

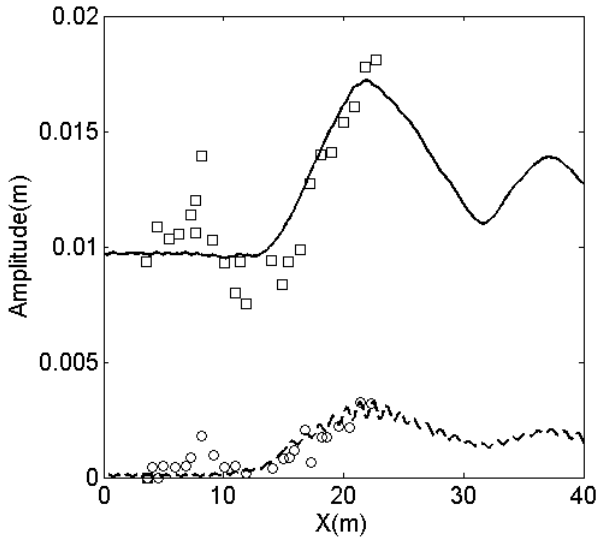

Figure 3.12: Comparison of wave amplitudes along the centerline of the tank for $T = 1.0$ s and $a_0 = 0.98$ cm. Modeled first harmonic (—), second harmonic (- - -). Data of Whalin [77]: first harmonic (□), second harmonic (o).

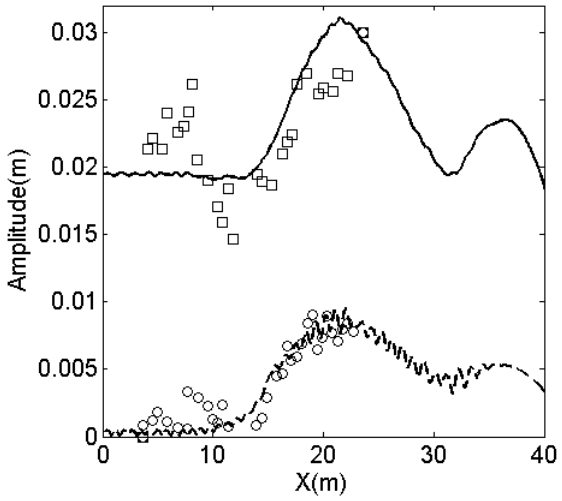

Figure 3.13: Comparison of wave amplitudes along the centerline of the tank for $T = 1.0$ s and $a_0 = 1.95$ cm. Modeled first harmonic (—), second harmonic (- - -). Data of Whalin [77]: first harmonic (□), second harmonic (o).

3.2.4 Nonlinear Harbor Interactions

Harbor resonance in the presence of wave-wave interactions may have a significant impact on harbor design applications. Rogers and Mei [17], in a rigorous experimental and numerical study, investigated the effects of nonlinear energy transfer on resonant excitations inside idealized rectangular harbors with narrow harbor region (see Fig. 6.10). For modeling purposes, they divided the nonlinear problem into two one-dimensional problems: first, for the narrow bay region, they used conventional shallow water equations, and second, for the outer region, they applied linear wave theory. A matching condition, also called the impedance condition, was used at the junction of two sub-domains. However, they acknowledged the poor performance of the impedance condition for higher harmonics and suggested that more general models be developed. They also conducted a set of experiments for a fixed fundamental frequency with varying harbor lengths and incident wave amplitudes. Three harbor lengths in their experiments corresponded to the first three resonant peaks of the fundamental frequency. Here we use their experiments to examine the present model's capabilities to simulate nonlinear harbor interactions in the presence of strong reflection caused by harbor walls and coastlines. As discussed previously, parabolic approximation based models are inappropriate in such situations.

In a more recent study, Woo and Liu [18] used a Boussinesq-type model with improved dispersive and nonlinear characteristics to simulate harbor interactions. They simulated harbor interactions for three different bay configurations with one set of incident amplitudes; however, with the presnet model, we only consider the longest bay configuration due to numerical limitations discussed later.

The computational domain for a 1:10 prototype harbor model (similar to [18]) of the experiments with the longest bay configuration is shown in Fig. 3.14. Only half

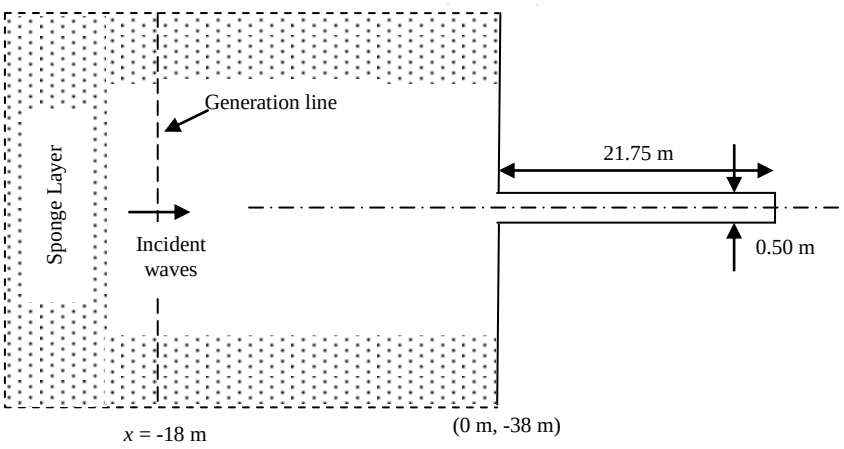

Figure 3.14: Computational domain for nonlinear harbor problem. Figure not drawn to scale.

the domain is considered for computations, for reasons of symmetry. The prototype model has a uniform water depth of 1.53 m all over the domain. All harbor walls, including the coastline, are assumed to be fully reflecting. Therefore, the internal wave generation method, with γ based on the criteria discussed in Section 2.3, is used for upwave boundary treatment, and the scattered waves are absorbed using a two wavelength-wide sponge layer placed near the generation line.

There appears to be some lack of clarity in [17] regarding the input, as noted by Woo and Liu [18]. To derive input conditions, we utilize measurements of standing wave amplitudes and phase differences available from the experiments conducted by [17] with the bay mouth closed. Based on this information, and by simulating these experiments with the present model, we observe that it is sufficient to assign amplitudes for the first two wave harmonics. The third harmonic is assumed to have zero incident amplitude and is allowed to grow through nonlinear interactions. A similar approach was used by Woo and Liu [18] in their study. Two separate cases with different incident amplitudes but for the same wave frequencies and bay length

of 21.75 m are simulated. For numerical simulations, the primary and secondary harmonics have incident amplitudes of 0.0305 m and 0.0074 m respectively for the first case, and 0.0206 m and 0.0019 m respectively for the second case. In both cases, wave periods for primary and secondary harmonics are 4.90 s and 2.45 s respectively. These incident harmonics are input at the wave generation line located at $x = -18$ m (shown in Fig. 3.14).

It is observed that the wavefield inside the bay is mostly one-dimensional (not shown) which is consistent with the experiments. The modeled results along the bay axis ($y = 0.0$) for both cases are compared with the experimental data of [17] in Figs. 3.15 and 3.16 for all wave harmonics. The existence of nodes and antinodes inside the bay is due to the standing wave formation. Although the model behaves satisfactorily for both cases, some mismatch between the model results and the experimental data is observed in the vicinity of bay entrance. The second harmonic is over-predicted near the entrance. A similar discrepancy was observed by Woo and Liu [18] for the first case with their Boussinesq-type model. They reported strong gradients near the bay entrance which also generated high-frequency wiggles near the bay entrance. To overcome this issue with their finite-element model, they suggested rounding of the boundary near the corner, to avoid singularities at corner nodes. With the present model, although we do not observe high-frequency wiggles for both cases, examination reveals that the $QNLs$ in Eq. (9) attain large values, especially for higher harmonics in the vicinity of the entrance. This is most probably due to the accumulation of numerical errors associated with the computation of higher-order derivatives at the corner and nearby boundary nodes. Fortunately, the effect of these errors on model results is mostly local, and the solution away from the entrance is not affected significantly. As shown in Figs. 3.15 and 3.16, the modeled harmonics are in good agreement with the experiments for $x \geq 6$ m. A thin friction

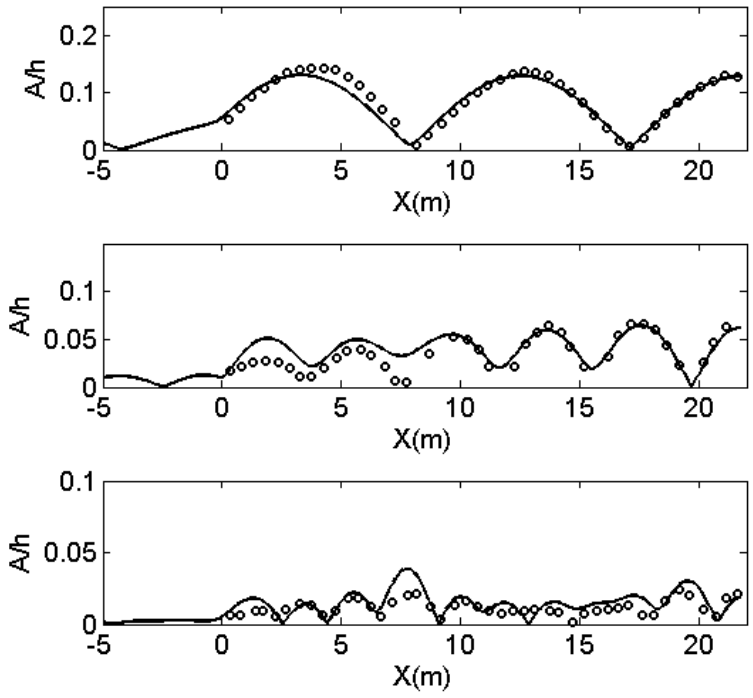

Figure 3.15: Comparison of wave amplitudes along the longitudinal axis of the bay for the first case. Modeled harmonics (—) and experimental data (o) of Rogers and Mei [17]. (Top) First harmonic; (middle) second harmonic; (bottom) third harmonic.

layer with uniformly low friction factor near the entrance region marginally reduced these numerical errors; however, eventually using finite elements (as is the case with many existing linear mild-slope models such as CGWAVE and PHAROS) or other methods that allow the use of boundary-fitted unstructured grids may ameliorate this effect. (Note that the errors near the entrance are owing to the approximate numerical (finite-difference) method and not due to the governing equation).

A domain with 1000 X 400 grid ($\Delta x/L_{min} = 0.016$ and $\Delta y/L_{min} = 0.023$) and a temporal resolution of ($\Delta t/T_{min} = 0.09$ s is found satisfactory in both cases; the steady-state solution is obtained in 9000 steps. An abundant number of grids are

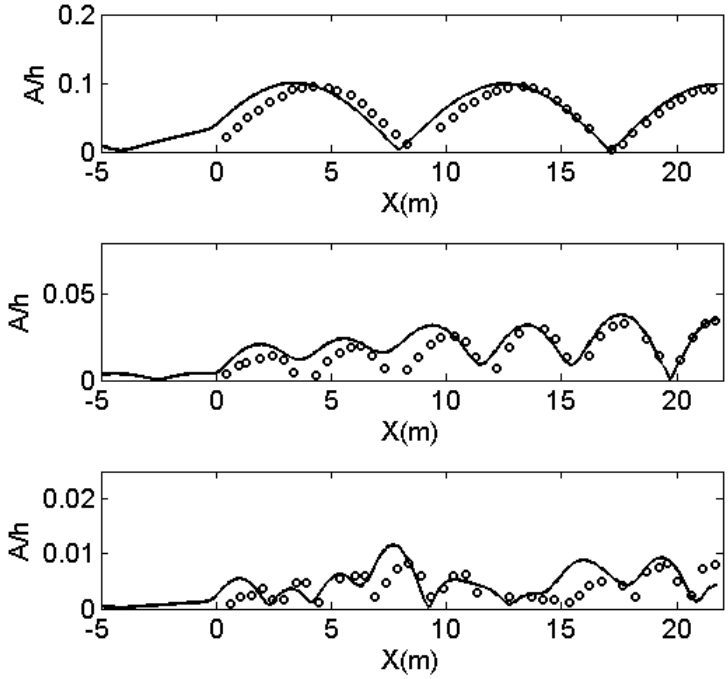

Figure 3.16: Comparison of wave amplitudes along the longitudinal axis of the bay for the second case. Modeled harmonics (—) and experimental data (o) of Rogers and Mei [17]. (Top) First harmonic; (middle) second harmonic; (bottom) third harmonic.

used especially in y-direction to properly resolve inner bay and the region near bay mouth. However, the number of grid points can significantly be reduced with a model that allows variable grid density within a domain (as in case of [18]).

Note that the transformation (reduction) of the modeled amplitude of primary harmonic (results shown in [17]) due to nonlinear interactions is most significant for the longest bay case in [17]; therefore, the longer bay configuration has perhaps provided sufficient challenges to test various features as well as nonlinear aspects of the present model. The model used in this dissertation is also discussed by Sharme et al. [81].

3.3 Summary and Conclusions

This study describes the development of an approach to simulate nonlinear wave transformation in the presence of wave reflection, diffraction, refraction, breaking, etc. The proposed model would be applicable to a wide range of practical wave conditions encountered in harbor and coastal engineering applications. Since linear elliptic equation models (e.g. MIKE21-EMS, CGWAVE, PHAROS, etc) are widely used for harbor applications, an initial foray is made into extending such models to include wave-wave interactions. It is expected that the findings of this research will contribute to the eventual development of a new generation of elliptic harbor wave models. The second-order extension of nonlinear elliptic mild-slope equation was first considered; however, convergence issues inspired the derivation of an evolution-type equation. The ADI scheme with finite-difference method is found to perform satisfactorily for all the validation cases. Boundary conditions typically used for elliptic (linear) wave models were found to be unsatisfactory. A combination of these boundary conditions with dissipative sponge layers and internal wave generation techniques was therefore established and validated for the present model. Further, the "marching" process used in the evolution scheme enables one to compute the nonlinear terms for both wave-wave interactions and breaking simultaneously without requiring an "iterative" process in the usual sense of the word, as described in previous work [6, 12]. Various model features are verified for a variety of wave conditions ranging from deep to shallow water conditions. Reasonable agreement found between data and model results, and superior model performance in some cases, suggest that the proposed approach will enhance the applicability of the elliptic mild-slope wave models. In addition, this preliminary investigation of the nonlinear mild-slope equation paves the way for the development of more sophisticated finite-element based

nonlinear models capable of handling arbitrary shaped domains in a more accurate manner.

Future efforts to extend the present model to handle multidirectional input and steep bathymetric variations may also be warranted. Motivation for such extensions come from the works of Athanassoulis and Belibassakis [82], Belibassakis and Athanassoulis [83] and Toledo and Agnon ([84]) who developed different forms of wave transformation models with improved capabilities to handle steep slopes. Although their models (in the context of nonlinear waves) are primarily applied to domains with one-dimensional bottom variations and are devoid of the mechanisms like breaking dissipation, internal generation, etc., they allow the incorporation of steep bathymetric variations encountered in practice. A study combining developments discussed in the present study with the models in [83, 84] will certainly benefit reseach community and wave modelers.

4. FINITE ELEMENT MODEL

4.1 Introduction

As discussed earlier in Chapter 2, modeling nonlinear wave-wave interactions in the presence of reflection, diffraction, and harbor resonance is critical for studies related to harbor design and tranquility. Many finite-element (FE) models (e.g. CGWAVE) based on the standard elliptic mild-slope equation of Berkhoff [1, 2] have been developed. Such FE models are well known for efficient handling of complex harbor and nearshore processes. Nonlinear mechanisms such as breaking, wave-current interactions, amplitude dispersion and wave-direction-dependent boundary conditions are also incorporated in these models. For harbor design problems, the FE models which allow the use of unstructured grids are preferred over finite-difference models. The use of unstructured grids allows accurate delineation of domain boundaries (e.g. harbor walls, arbitrary-shaped coastlines, structural boundaries), ensuring proper imposition of boundary conditions. This is important for appropriate handling of wave reflection and diffraction effects in the vicinity of domain boundaries. In addition, for such models, the mesh density can easily be refined (in a region of interest) for improved accuracy. Owing to these advantages, the FE models have been successfully applied to simulate wave transformation in complex harbor domains (e.g. Los Angeles/Long Beach harbor [11]; Douglas Harbor [5]; Venice Harbor, [12] and around coastal structures present in nearshore regions.

Yet, it must be noted that the governing equation for the existing FE models is Eq. (2.5) or its extensions which are only suitable for linear waves. Importantly, nonlinear wave-wave interactions are completely ignored in these models. However, as discussed in Chapter 1, these nonlinear interactions are known to be quite significant especially

in shoaling regions and in harbors.

In this Chapter, we discuss the development of an approach that extends the existing FE models to incorporate nonlinear wave-wave interaction effects. In Chapter 2, we considered the second-order extension [20, 21] of the standard mild-slope equation for the development of a finite-difference model. The finite-difference model uses an effective method for boundary treatment (using internal generation and dissipative sponge layers) and provides stable solutions with good convergence properties. Here, for the FE model, we use the same boundary value problem discussed in Chapter 2. The methodology discussed here will improve the applicability of the existing FE models mentioned above.

The structure of this Chapter is as follows: After presenting the boundary-value problem in Section 4.2, we discuss the finite-element formulation in Section 4.3. The numerical solution scheme used in the model is also discussed in this section. Two cases are considered for model validation in Section 4.5. The model is then applied to simulate nonlinear wave transformation in Ponce de Leon Inlet, FL. Concluding remarks and recommendations for future work are provided in Section 4.6.

4.2 The Boundary-Value Problem

A typical harbor domain where the boundary value problem is solved is shown in Fig. 4.1. The governing equation for the computational region Ω is same as in the finite-difference model, i.e.

$$\begin{aligned} &2i\omega_n \frac{\partial \hat{\phi}_n}{\partial t} + \nabla_h \cdot [(CC_g)_n \nabla_h \hat{\phi}_n] + k_n^2 (CC_g)_n \hat{\phi}_n + ik_n (CC_g)_n \alpha_n \hat{\phi}_n \\ &+ i\omega_n D\hat{\phi}_n = \{QNLs\}_n + \{S\}_n \end{aligned} \tag{4.1}$$

where $\{QNLs\}_n$ represents quadratic nonlinear terms defined earlier in Chapter 2. Eq. (4.1) also includes terms related to breaking, friction and source function

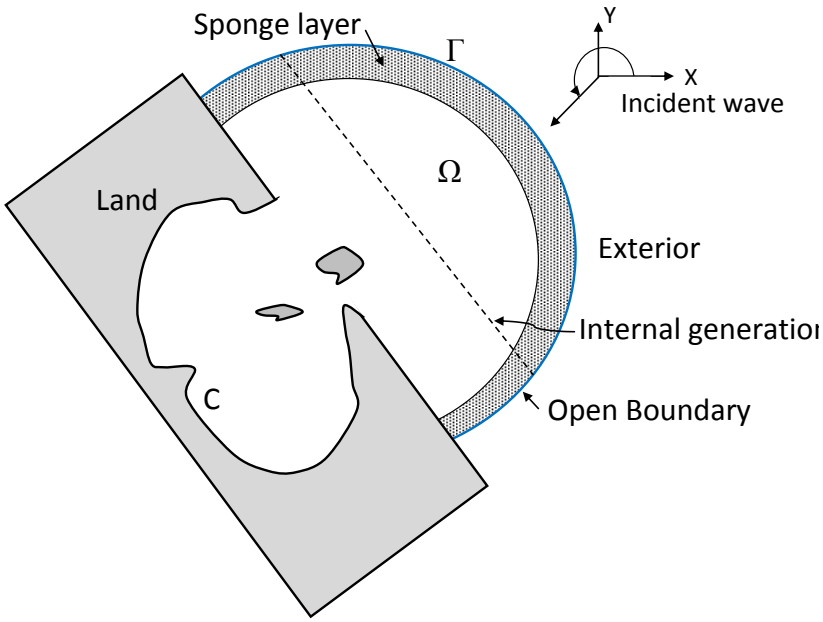

Figure 4.1: A typical harbor domain

associated with the internal wave generation. More details regarding the breaking factor α_n, friction factor D_n and source function $\{S\}_n$ can be found in Chapter 3.

For the completeness of the boudary-value problem, linear boundary conditions (discussed earlier in Chapter 2) are imposed along the domain boundary Γ which is comprised of closed boundary Γ_c and open boundary Γ_o segments. These approximate boundary conditions are supplemented with internal wave generation and sponge layers for improved boundary treatment. Note that, in comparison to the existing FE models based on the linear elliptic equation, only the governing equation has been modified, but the boundary conditions remain same. The development of the FE model based on the boundary value problem discussed above is presented in the next section.

4.3 Development of a Finite Element Model

To develop a finite element model over a two-dimensional computational region Ω enclosed by boundary Γ, we first redefine the boundary value problem (discussed above) in a concise form: The governing equation

$$2i\omega_n \frac{\partial \hat{\phi}_n}{\partial t} + \nabla_h \cdot [a \nabla_h \hat{\phi}_n] + b\hat{\phi}_n = f_n(x, y, t) \tag{4.2}$$

where

$$a = (CC_g)_n ;$$

$$b = i\omega_n D_n + k_n^2 (CC_g)_n + ik_n (CC_g)_n \alpha_n;$$

$$f_n = \{QNL\}_n + \{S\}_n ;$$

and the generalized boundary condition

$$q_n \equiv \frac{\partial \hat{\phi}_n}{\partial n} = \hat{q}_n \quad \text{on } \Gamma. \tag{4.3}$$

Note that the function f_n on the right hand side in Eq. (4.2) has contributions due to nonlinear interaction effects in $\{QNL\}_n$ and source function $\{S\}_n$; b includes frictional and breaking dissipation effects. Eq. (4.3) is the generalized form of the standard linear boundary conditions applied at the closed boundary (Γ_c) and open boundary (Γ_o) segments. The boundary-value problem discussed above is a parabolic time-dependent problem. The development of a Galerkin finite-element model of such problems, in general, involves two main steps: (1) semidiscretization, and (2) time approximation. (Details regarding such models can be found in [85]). In the semidiscretization step, a weak formulation of the boundary value problem over an

element Ω^e is first established:

$$\int\int_{\Omega^e}\left[v\left(2i\omega_n\frac{\partial\hat{\phi}_n}{\partial t}+b\hat{\phi}_n-F_n\right)-a\nabla_h\hat{\phi}_n\cdot\nabla_h v\right]dxdy-\oint_{\Gamma^e}\left(\tilde{a}\frac{\partial\hat{\phi}_n}{\partial n}\right)vdxdy=0 \tag{4.4}$$

where $v(x,y)$ is a weight function and the spatial approximation of the dependent variable $\hat{\phi}_n$ over finite elements is then defined in the form

$$\hat{\phi}_n(x,y,t)=\sum_{j=1}^{m}\hat{\phi}^e_{nj}(t)N^e_j \tag{4.5}$$

where $\hat{\phi}^e_{nj}$ represents the value of $\hat{\phi}_n$ at location (x_j,y_j) in an element e. N^e_j for $j=1,2,..m$ is shape function. In Eq. (4.5), it is assumed that the time dependence of the dependent variable $\hat{\phi}_n$ is separable from its spatial variation. The substitution of Eq. (4.5) in the weak form results in a set of ordinary differential equations (ODEs) in time:

$$\sum_{j=1}^{m}\left(M^e_{ij}\frac{d\hat{\phi}^e_{nj}}{dt}+K^e_{ij}\hat{\phi}^e_{nj}\right)-f^e_{ni}-Q^e_i=0\quad(i,j=1,2,...m) \tag{4.6}$$

or, in matrix form

$$[M^e]\left\{\dot{\hat{\phi}}^e_n\right\}+[K^e]\left\{\hat{\phi}^e_n\right\}=\{F^e_n\} \tag{4.7}$$

where $\{F^e_n\}=\{f^e_n\}+\{Q^e\}$, and the element matrices $[M^e]$, $[K^e]$, $\{f^e\}$ and $\{Q^e\}$ are defined using

$$M^e_{ij}=2i\omega_n\int_{\Omega^e}N_iN_jdxdy, \tag{4.8}$$

$$K^e_{ij}=\int_{\Omega^e}\left\{-a\nabla_hN_i\cdot\nabla_hN_j+bN_iN_j\right\}dxdy, \tag{4.9}$$

$$f^e_i=\int_{\Omega^e}f_nN_idxdy \tag{4.10}$$

and

$$Q_i^e = \int_{\Omega^e} q_n N_i dx dy. \tag{4.11}$$

In this study, triangular finite elements for which shape function N_i is a linear function are considered for spatial discretization. More details regarding shape functions and the computation of element matrices can be found in [85].

In the second "time-approximation" step, the time discretization of the ODEs in Eq. (4.6) is obtained by using a finite-difference scheme. We consider the commonly used "α *family of approximation*" method [85] in which a weighted average of the time derivative is defined using

$$(1-\alpha)\left\{\dot{\hat{\phi}}^e\right\}_s + (1-\alpha)\left\{\dot{\hat{\phi}}^e\right\}_{s+1} = \frac{\left\{\hat{\phi}^e\right\}_{s+1} - \left\{\hat{\phi}^e\right\}_s}{\Delta t_{s+1}} \tag{4.12}$$

where subscript s denotes values at time t_s. Using this approximation, the ODE in Eq. (4.6) is transformed (at any time t_s) into a set of algebraic equations:

$$\left[\hat{K}^e\right]_{s+1}\left\{\hat{\phi}_n^e\right\}_{s+1} = \left\{\hat{F}_n^e\right\}_{s,s+1} \tag{4.13}$$

where

$$\left[\hat{K}^e\right]_{s+1} = [M^e] + \alpha\Delta t\,[K^e]_{s+1}\,;$$

$$\left\{\hat{F}_n^e\right\}_{s,s+1} = \Delta t\left(\alpha\left\{F_n^e\right\}_{s+1} + (1-\alpha)\left\{F_n^e\right\}_s\right) + \left([M^e] - (1-\alpha)\Delta t\,[K^e]_s\right)\left\{\hat{\phi}_n^e\right\}_s.$$

Different values of α in the equations above give different well-known approximations:

$$\alpha = \begin{cases} 0, & \text{the forward difference scheme; conditionally stable} \\ 1/2, & \text{the Crank-Nicolson scheme; unconditionally stable} \\ 2/3, & \text{the Galerkin scheme; unconditionally stable} \\ 1, & \text{the backward difference scheme; unconditionally stable} \end{cases}$$

For the present study, we use the backward-difference scheme (i.e. $\alpha = 1$) to obtain a set of algebraic equation similar to Eq. 4.13. Next, the element matrix form in Eq. 4.13 is assembled over all elements to get the assembled matrix form:

$$\left[\hat{K}\right]_{s+1} \left\{\hat{\phi}_n\right\}_{s+1} = \left\{\hat{F}_n\right\}_{s,s+1} \tag{4.14}$$

where $[\hat{K}]$ and $\hat{F}_n$ are the assembled matrices; . $\left\{\hat{\phi}_n\right\}_{s+1}$ is the solution of the boundary value problem at time t_{s+1}.

4.4 Solution Algorithm

The set of algebraic equations in Eq. 4.14 can be solved at any time step using the standard iterative methods (e.g. Successive over-relaxation method, Gauss-Seidel method) or Krylov subspace methods (e.g. Conjugate gradient method, generalized minimal residual method). Here we use the standard Conjugate Gradient method (see [86]) to obtain solutions at all time steps. For linear elliptic models, this method is known to perform very well even for complex domains.

Since the standard Conjugate method requires $\left[\hat{K}\right]_{s+1}$ to be symmetric and positive-definite, we first use the Gauss transformation, i.e. multiply Eq. 4.14 by

$\left[\hat{K}^*\right]_{s+1}$, the complex conjugate transpose of $\left[\hat{K}\right]$:

$$\left[\hat{K}^*\right]_{s+1}\left[\hat{K}\right]_{s+1}\left\{\hat{\phi}_n\right\}_{s+1} = \left[\hat{K}^*\right]_{s+1}\left\{\hat{F}_n\right\}_{s,s+1}. \tag{4.15}$$

The matrix $\left[\hat{K}^*\right]_{s+1}\left[\hat{K}\right]_{s+1}$ is always symmetric and positive-definitive. Following Panchang et al. [86], the solution of Eq. 4.15 is obtained using the following algorithm:

1. To obtain solution at time t_{s+1}, start the iterative procedure with $\hat{\phi}_n$ (solution at $t = t_s$) for all grid points where the solution is desired. An initial guess for $\hat{\phi}_n$ is needed for $t = 0$;
2. At $i = 0^{th}$ iteration, compute for all points $r_0 = \hat{F}_n - \hat{K}\phi_{n,0}$ and $p_0 = \hat{K}^* r_0$
3. Compute for the i^{th} iteration:

$$\alpha_i = \frac{\left|\hat{K}^* r_i\right|^2}{\left|\hat{K} p_i\right|^2}$$

4. Update at all points $\phi_{n,i+1} = \phi_{n,i} + \alpha_i p_i$
5. Check for convergence of solution.
6. Compute for all points $r_{i+1} = r_i - \alpha_i \hat{K} p_i$.
7. Compute for the i^{th} iteration:

$$\beta_i = \frac{\left|\hat{K}^* r_{i+1}\right|^2}{\left|\hat{K}^* r_i\right|^2}.$$

8. Compute at all points $p_{i+1} = \hat{K}^* r_{i+1} + \beta_i p_i$.
9. Set $i = i + 1$ and go to step 3.

More details pertaining to the algorithm above are given in [86].

4.5 Model Validation

For preliminary testing, the model was first successfully verified (with $QNLs = 0$) for linear problems. (Results for these problems are not shown for brevity.) Two test cases considered earlier in Chapter 3 for the validation of finite-difference model are used again for data-model comparisons. The tests involve: (1) two-dimensional nonlinear shoaling over a topographic lens; and (2) nonlinear harbor resonant interactions in a rectangular harbor.

4.5.1 Wave Propagation over Semicircular Shoal

Many researchers (e.g. [74], [79], [20]) have considered experimental data of [77] to validate their model's capability to simulate nonlinear wave shoaling. The set-up for Whalin's experiments is shown in Fig. 3.9. The wave tank had a length of 25.60 m and a width of 6.10 m, and the topography consists of a semicircular shoal in the central portion of the tank (Fig. 3.9). Whalin conducted tests for incident periods of $T = 1, 2$ and 3 s. The present FE model is applied to the $T = 1$ s case with incident amplitude of 1.95 cm. Two harmonics are found to be sufficient for this case. For numerical simulation, the internal wave generation method is used with the generation line located near $X = 0.0$ m, and the sponge layers are placed to absorb waves near the offshore and the coastal boundaries. The higher-harmonics are assumed to have zero incident wave amplitude at the generation line. A similar boundary treatment approach was used earlier for the validation of the finite-difference model.

Modeled results along the centerline $Y = 3.078$ m are compared with experimental data in Fig. 4.2. It can be seen in the plot that the modeled wave-field compares very well with the experimental data. Moreover, the modeled amplitudes shown in Fig. 4.2 are mostly similar to the amplitudes obtained using the finite-difference

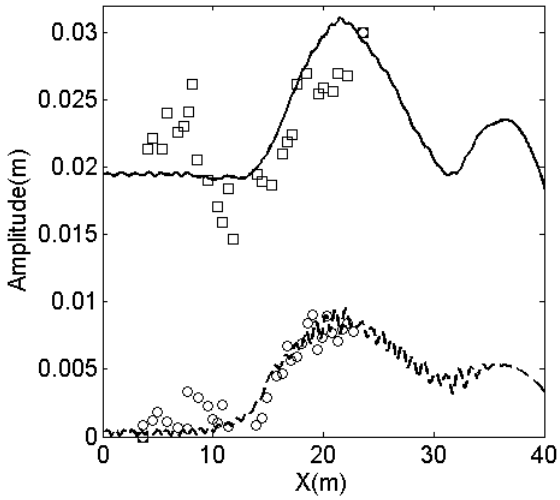

Figure 4.2: Comparison of wave amplitudes along the centerline of the tank for $T = 1.0$ s and $a_0 = 1.95$ cm. Modeled first harmonic (—), second harmonic (- - -). Data of Whalin [77]: first harmonic (□), second harmonic (o).

model in Chapter 3.

For an unstructured grid with 7100 triangular elements, and a "time" step of $\Delta t/T_{min}$ =0.20, a total of 200 steps are sufficient to achieve final steady-state solution on a computer with 2 GB RAM and a 3 GHz processor. The computational time to reach steady-state is less than 5 mins. At each time step, 1000 iterations are found sufficient. For larger time steps, more number of iterations are generally required.

4.5.2 Nonlinear Harbor Interactions

As discussed in Chapter 3. wave-wave interactions have a significant impact on harbor design applications. Rogers and Mei [17] and Woo and Liu [18] investigated the effects of nonlinear energy transfer on resonant excitation inside rectangular harbors. Here we again consider the experimental data of [17] to examine the newly developed FE model. All harbor walls, including the coastline, are fully reflecting. Two test cases with same input wave conditions but different bay lengths (21.75 m

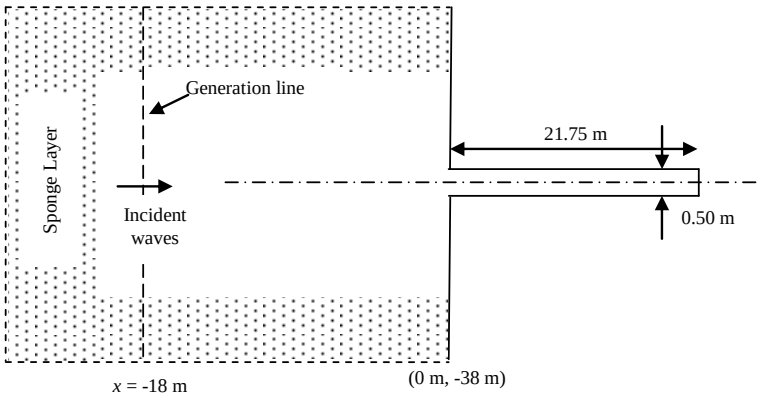

Figure 4.3: Computational domain for nonlinear harbor problem. Figure not drawn to scale.

and 13.70 m) are considered. The computational domain (for a 1:10 prototype harbor model) with the longest bay configuration is shown in Fig. 4.3. The model has a uniform water depth of 1.53 m all over the domain. Similar to Woo and Liu [18], three input harmonics are used. The primary and secondary harmonics have incident amplitudes of 0.035 m and 0.01 m respectively for the two bay configurations. Wave period for the fundamental harmonic is 4.90 s. The wave generation line (at x = -18 m) and the sponge layers are shown in Fig. 4.3. A similar boundary treatment approach was used earlier with the finite-difference model.

For the two cases, the modeled wave-fields along the bay axis ($y = 0.0$) are compared with the experimental data in Figs. 4.4-4.5. The formation of nodes and antinodes is consistent with the data of Rogers and Mei [17]. Although the model behaves satisfactorily for both cases, some mismatch between the modeled amplitudes and the experimental data is observed. In comparison to the results shown earlier in Chapter 3 (for the longer bay case), in this case, the rounding of corners at bay mouth improves modeled results near the bay entrance. In the second case, some mismatch is observed between the modeled first harmonic and experimental data in

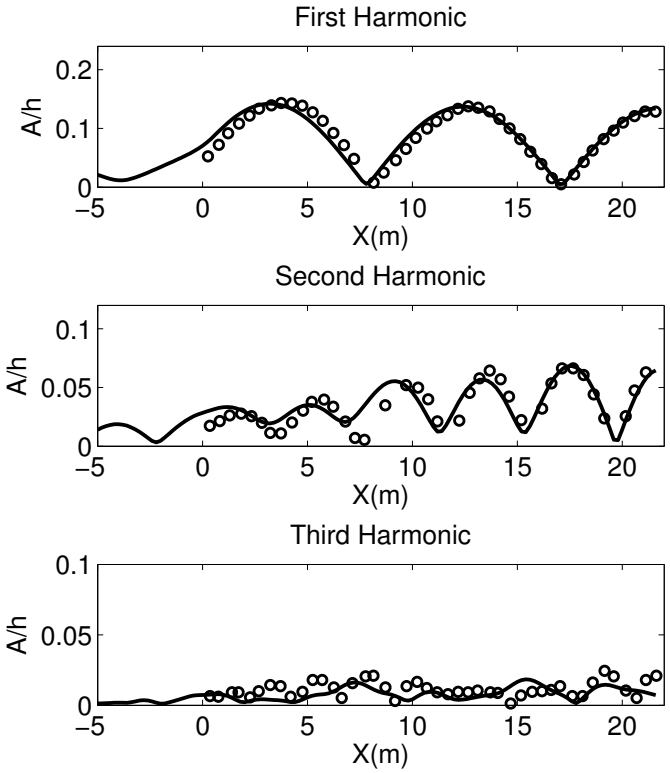

Figure 4.4: Comparison of wave amplitudes along the longitudinal axis of the bay for the first case. Modeled harmonics (—) and experimental data (o) of Rogers and Mei [17]. (Top) First harmonic; (middle) second harmonic; (bottom) third harmonic.

Fig. 4.5. However, this discrepancy is consistent with Woo and Liu [18] and Rogers adn Mei [17]. According to Rogers and Mei [17], harbor entrance losses (ignored here) are more important for the shorter bay case than for the longer bay case. On the other hand, wave-wave interactions are more dominant inside the longer bay. A proper handling of harbor entrance losses may improve modeled results in the second case.

An unstructured grid with 12,310 triangular elements and a temporal resolution of ($\Delta t/T_{min} = 0.09$ s is found satisfactory; the steady-state solution is obtained in

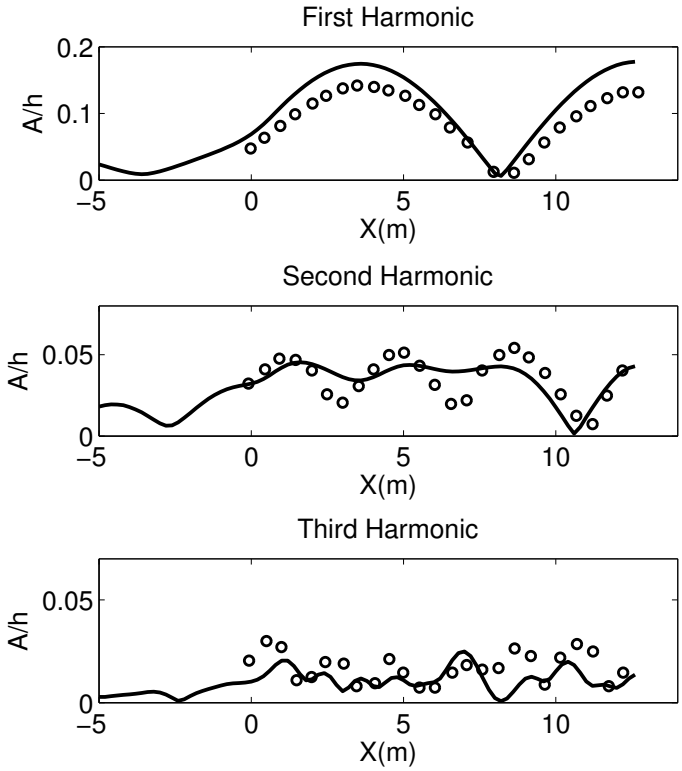

Figure 4.5: Comparison of wave amplitudes along the longitudinal axis of the bay for the second case. Modeled harmonics (—) and experimental data (o) of Rogers and Mei [17]. (Top) First harmonic; (middle) second harmonic; (bottom) third harmonic.

5000 steps. High-resolution mesh is used near the bay entrance.

4.6 Modeling Wave Transformation in Ponce de Leon Inlet

Ponce de Leon Inlet is located near Orlando in Florida. As shown in Fig. 4.6, the bathymetry at Ponce de Leon Inlet consists of a navigation channel, jetty, large ebb shoal, and inlet. The U.S. Army Engineer Research and Development Center conducted an experimental study using a 1:100-scale physical model in which the north jetty was modeled like a vertical wall with stones sloped around it, and the south jetty was not included. Wave data collected during these experiments have

been used by researchers (e.g. [87], [88]) for model validation. Shi et al. [88] successfully validated their Boussinesq model against data. Since we do not have access to the experimental data, in this study we use the BOUSS-2D model to validate the performance of newly developed FE model. BOUSS-2D is a sophisticated model that solves Boussinesq-type equations and is widely used for harbor and coastal applications.

Two different cases are considered for modeling purposes. The incident wave direction is normal to the offshore boundary $Y = 0.0$. Coastline is chosen to be fully absorbing, and the jetty is fully reflective. In the first case, a monochromatic wave with height $H_{m0} = 0.78$ m and period $T = 15$ s is input. A total of four harmonics are considered. The internal wave generation method is used with the generation line located near $Y = 0.0$ m, and the dissipative sponge layers are placed along the open-ocean boundaries to minimize spurious wave reflections from the boundaries. Wave breaking is simulated using the breaking model of [75]. Details regarding the breaking model are provided earlier in Chapter 3.

The finite element mesh for this case contains of about 210000 nodes and 420000 elements. Modeled significant wave heights obtained using the present FE model and the BOUSS-2D model are compared in Fig. 4.7. Very good agreement is observed between the results obtained using two models. Wave reflection effects near the inlet and nonlinear shoaling effects over the shoal are well captured by the present FE model. Wave heights are also compared (see Fig. 4.8) along the two arrays (Array 1 and array 2 shown in Fig. 4.6) and a good agreement is observed. Moreover, snapshots of the modeled free surface elevation obtained from the two models are shown in Fig. 4.9.

In the second case, a shallow water TMA spectrum with 15 s peak period and $H_{m0} = 0.98$ m is considered as input. Detailed analysis of this case is in progress;

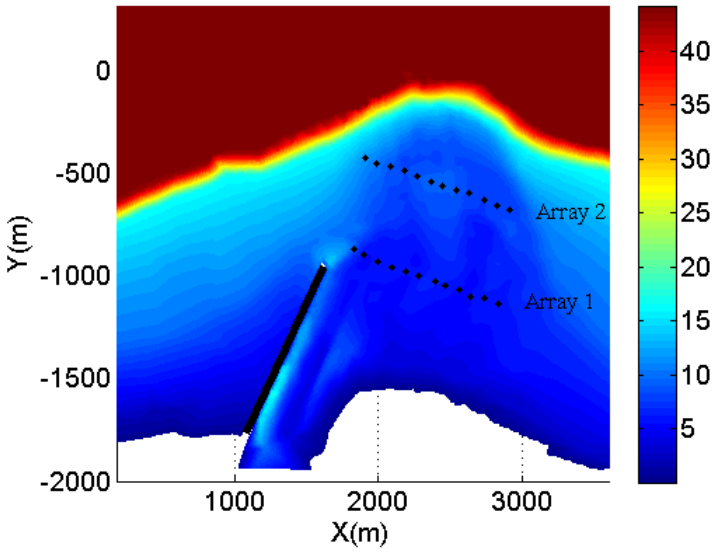

Figure 4.6: Ponce de Leon Inlet bathymetry (in m).

some preliminary results are discussed here. The finite element mesh for this case contains of about 650000 nodes and 910000 elements. For the present model, the wave spectrum is divided into 25 wave components. Modeled significant wave heights obtained using the present FE model and the BOUSS-2D model are compared in Fig. 4.10. Although the present model performs reasonably well, some mismatch especially near the jetty and shoal region is observed. A possible reason is that the BOUSS-2D model uses a well resolved TMA spectrum. In future, we consider using a large number of wave components for more reliable results.

4.7 Conclusions and Recommendations

This study describes the development of a finite-element model based on the second-order extension of the standard elliptic mild-slope equation. The proposed model is capable of simulating nonlinear wave transformation in complex harbor and coastal domains. The model, using unstructured grids, allows accurate imposition of

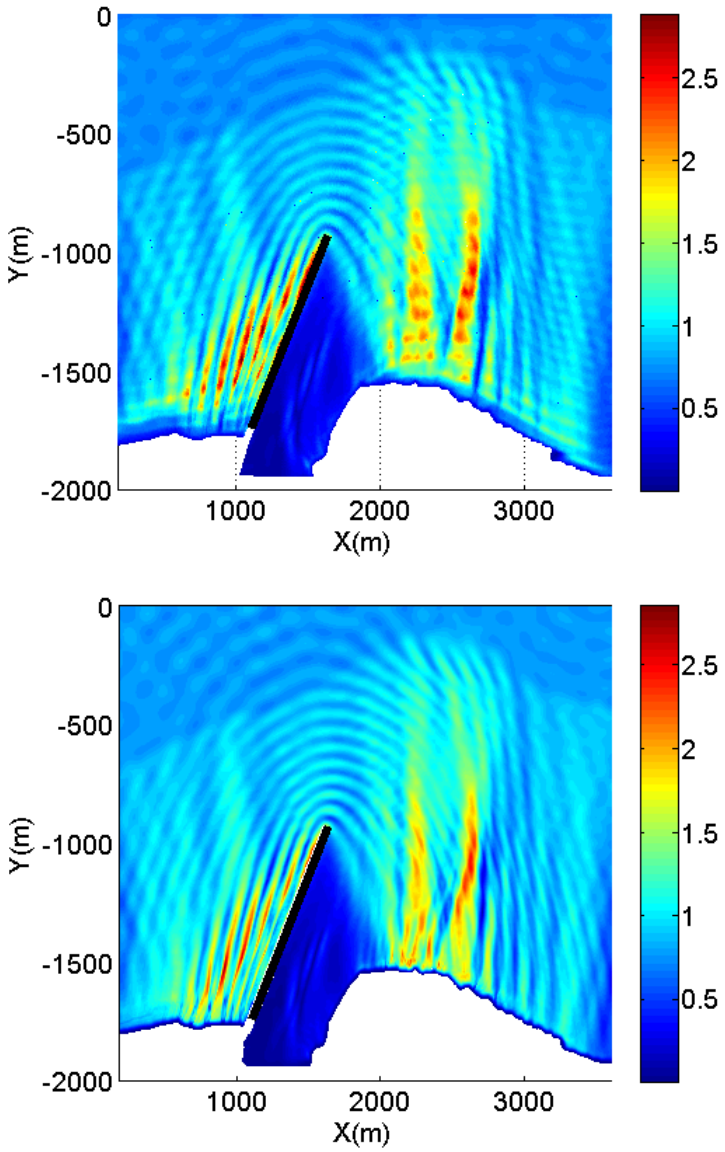

Figure 4.7: Wave height comparison. Modeled SWH using the present model (top) and using BOUSS-2D (bottom).

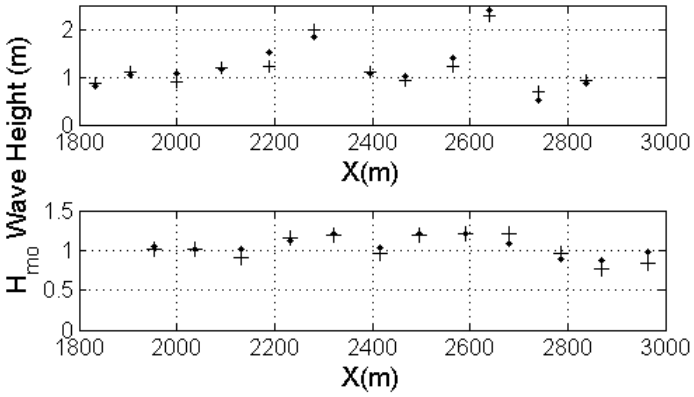

Figure 4.8: Comparison of wave heights along Array 1 (top) and Array 2 (bottom). Present FE model (··); BOUSS-2D model (+ +).

boundary conditions and handling of reflection/diffraction. For effective boundary treatment, the commonly used linear boundary conditions are supplemented with internal wave generation method and dissipative sponge layers. Model performance is verified for two different cases involving nonlinear shoaling and harbor resonance. The model is also applied to a real application involving arbitrary shaped boundaries and complex bathymetric features. Satisfactory model performance suggests that the proposed approach will enhance the applicability of the existing finite-element models based on the elliptic mild-slope equation.

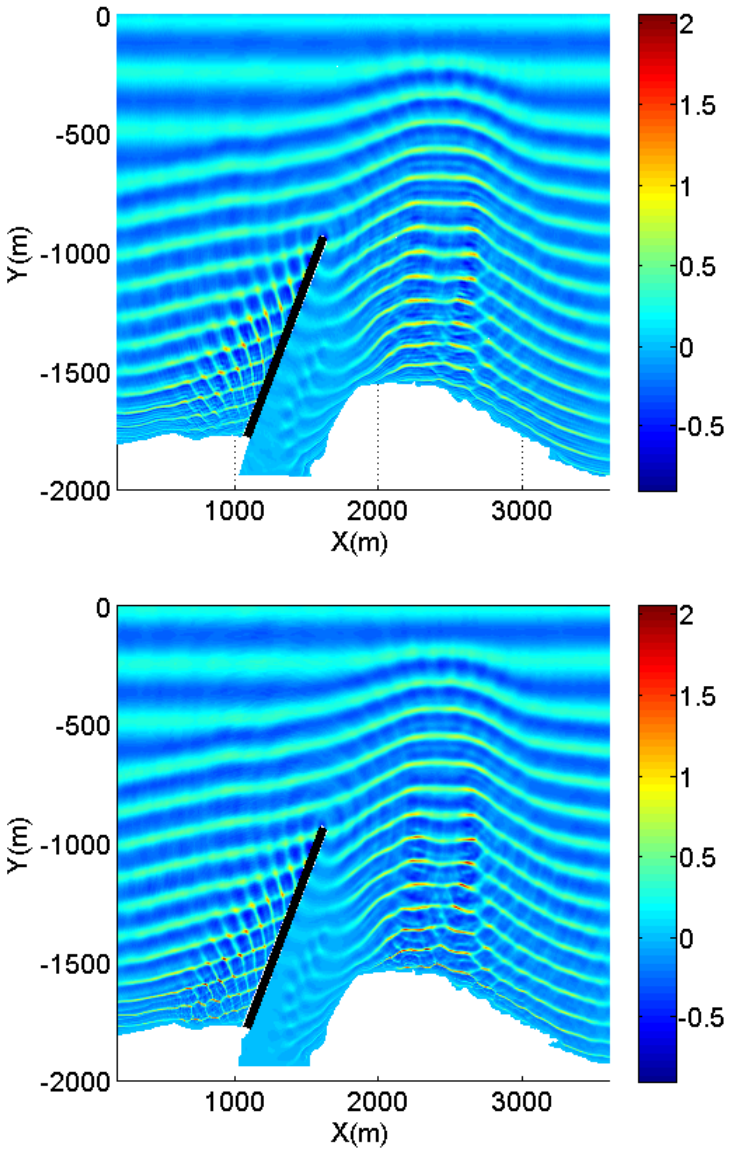

Figure 4.9: Modeled surface elevations using the present model (top) and using BOUSS-2D (bottom).

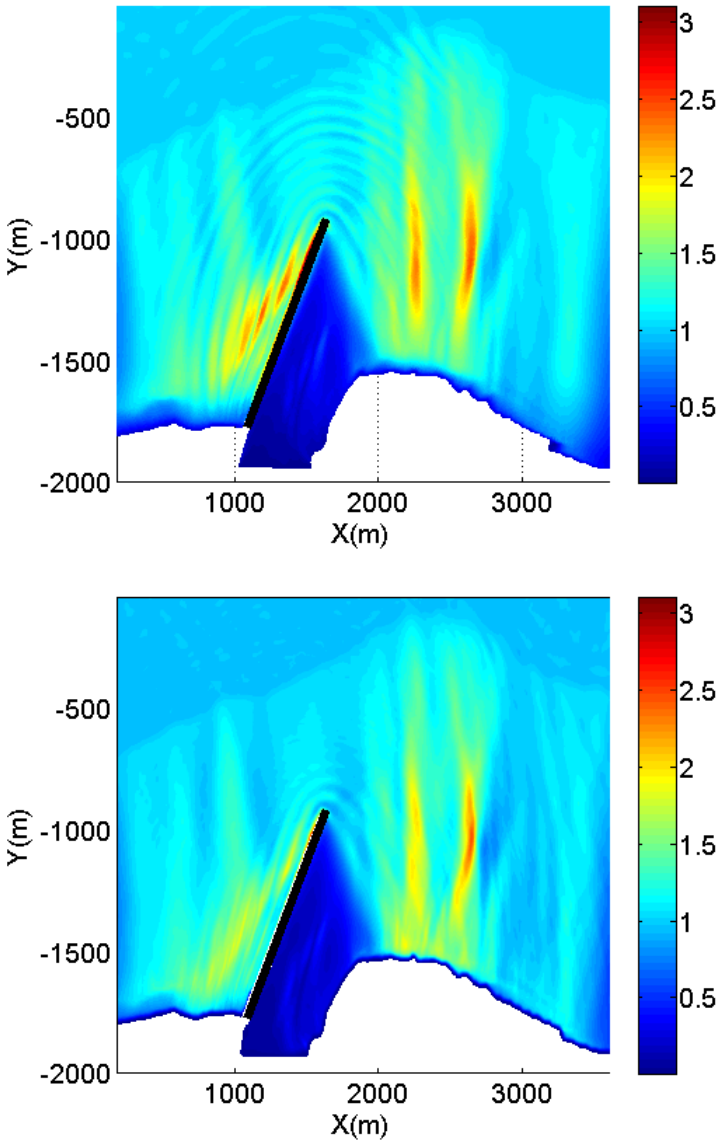

Figure 4.10: Wave height comparison. Modeled SWH using the present model (top) and using BOUSS-2D (bottom).

5. GENERALIZED VERTICALLY DEPENDENT RADIATION STRESS TENSOR

Many theoretical, analytical and experimental studies pertaining to wave-induced circulation in nearshore regions have been conducted over the last few decades. Different expressions for wave radiation stress tensor have been developed for progressive waves. In this Chapter, a discussion pertaining to the performance of three 3-D RSTs (M11, M13 and L08) for progressive waves is first provided in Section 5.1. A brief background on elliptic wave models is provided in Section 5.2. An expression for wave-induced pressure distribution for an arbitrary wave field is developed in Section 5.3. The new generalized formulation for 3-D RST is derived in Section 5.4; its expression in terms of the complex potential ϕ obtained from the elliptic models is also presented in this section. In Section 5.5, the generalized formulation is related to other RST formulations (e.g. [36], [24], [23]), and a new analytical expression for the vertically-dependent RST for a full/partial standing wave case is obtained.

5.1 Evaluation of Existing Approaches for 3-D RSTs

As discussed above, different approaches to obtain 3-D RSTs for linear progressive waves are available. Three approaches used for deriving M13, M11 and L08 are relevant to this study. We briefly evaluate these approaches before they are considered for the derivation of new generalized 3-D RSTs in Section 4. Consistent with the flow equations in [45], M13, M11 and L08 are expressed mathematically in the form

$$S_{\alpha\beta} = kE\left(\frac{k_\alpha k_\beta}{k^2}F_{CS}F_{CC} - \delta_{\alpha\beta}F_{SC}F_{SS}\right) + \delta_{\alpha\beta}\Im(\sigma) \tag{5.1}$$

where σ is the conventional sigma coordinate. The first term in Eq. (5.1) is same for M13, M11 and L08 with

$$F_{CS} = \frac{\cosh kd(1+\sigma)}{\sinh kd}; \quad F_{CC} = \frac{\cosh kd(1+\sigma)}{\cosh kd};$$

$$F_{SC} = \frac{\sinh kd(1+\sigma)}{\cosh kd}; \quad F_{SS} = \frac{\sinh kd(1+\sigma)}{\sinh kd},$$

but $\Im(\sigma)$ in the last term differs. For M11, $\Im(\sigma)$ is surface singular (non-zero only at surface) such that $\Im(\sigma) = \delta(\sigma)E/(2d)$ where

$$\delta(\sigma)= 0 \text{ if } \sigma\neq 0, \text{ and } \int_{-1}^{0} \delta(\sigma)d\sigma=1.$$

For M13, $\Im(\sigma) = \frac{E}{2d}\frac{\partial}{\partial\sigma}\left(2F_{CC}F_{SS} - F_{SS}^2\right)$, and for L08, $\Im(\sigma) = \frac{Ek}{2}\left(2F_{CS}F_{SS}\right)$. Note that the term $\Im(\sigma)$ in M11 is a surface singular term; however, for both M13 and L08, this term varies over the vertical. More details regarding the three formulations are provided in Section 5.

For a preliminary evaluation, we consider a sloping beach case [34] which involves wave breaking over a slope (1:40). As shown in Fig. 5.2(a), the wave tank is 150 m long, and the water depths at the deepest and the shallowest portion of the tank are 2.1 m and 0.1 m respectively. The incident wave has a height of 0.6 m and a period of 5 s. Modeled wave height shown in Fig. 5.2(b) is obtained by solving the wave energy equation. The wave-induced flow field (set-up/down and currents) is simulated using the EFDC model with radiation stresses obtained using M13, M11 and L08. (Details pertaining to the EFDC model are provided later in Section 6).

The modeled set-up/down (not shown here) from the three approaches compares very well with the analytical solution [34]. This is expected, because the analytical solution is based on the standard 2-D RST [23], and all three formulations on vertical

integration transform to the standard 2-D RST. However, for a complete evaluation, it is also important to examine modeled currents obtained using M13, M11 and L08.

Modeled currents are plotted in Figs. 5.2(c-e). For comparison, analytical solutions or other data are not available, but as mentioned earlier, M11 has been found to perform satisfactorily by researchers for applications involving sloping beaches. As shown in Figs. 5.2(c-e), the current fields obtained using M11 and L08 predict undertow inside surfzone. This seems physical, because undertow generally occurs for breaking waves over sloping beaches. In contrast, M13 produces a reverse undertow which does not seem correct. There are some minor differences between the magnitudes of currents obtained using M11 and L08.

At this point, although we do not have a definite answer regarding why M13 could not produce satisfactory results in this case, but it is obvious that the discrepancy in the modeled results arises due to the term $\Im(\sigma)$ which is defined differently for the three formulations. This issue regarding M13 and $\Im(\sigma)$ is discussed in Sections 5.

5.2 The Elliptic Wave Model

Phase-resolving models based on the standard mild-slope equation of Berkhoff [1, 2] are often used to simulate the transformation of small-amplitude waves inside harbors and around coastal structures. Models of this type have also been used by Karambas et al. (2007) and Newell et al. (2005) to simulate the wave-induced currents in complex domains. Breaking, which significantly alters the wave-induced circulation in nearshore regions, is included in terms of a parameterized dissipation function to obtain:

$$\nabla_h \cdot (CC_g \nabla_h \phi) + \left(k^2 CC_g + i\omega\gamma\right)\phi = 0 \tag{5.2}$$

where $\phi(x, y)$ denotes two-dimensional complex surface elevation as in Eq. (1.1); ∇_h is the gradient operator in the horizontal Cartesian coordinates (x, y); g is the acceleration due to gravity; C and C_g are phase and group velocity respectively; and γ is the parameterized breaking dissipation factor. Note that Eq. (5.2) is the vertically-integrated form of the 3-D Laplace equation ($\nabla^2\Phi = 0$ where Φ is the complex velocity potential) and is valid under the mild-slope assumption $|\nabla h|/kh \leq 1$. This assumption can however be relaxed by incorporating steep-slope effects [3]. The time-harmonic 3-D complex velocity potential Φ is related to $\phi(x, y)$ using Eq. (1.1).

For the elliptic equation (Eq. 5.2), many parameterizations for breaking dissipation factor γ have been tested [7]; since the breaking dissipation factor, in general, is a function of wave height which is not known *a priori*, Eq. (5.2) must be solved through iteration, as described by Zhao et al. [7]. Similar techniques are used in this study to obtain numerical solution; details regarding the iterative procedures, convergence issues, etc. may be found in [7]. For brevity, details regarding numerical strategies for solving Eq. (5.2) and boundary conditions are not provided here; they may be found elsewhere in [11].

Once $\phi(x, y)$ is estimated, the wave height (H) and surface elevation ($\tilde{\eta} = \tilde{\eta}_1 \cos\omega t + \tilde{\eta}_2 \sin\omega t$ where $\tilde{\eta}_1$ and $\tilde{\eta}_2$ are the real and imaginary parts of $\tilde{\eta}$ respectively) at all grid locations are obtained from $\phi(x, y)$ using

$$H = \frac{2\omega}{g} |\phi| \tag{5.4a}$$

and

$$\tilde{\eta} = -\frac{1}{g} \left(\frac{\partial \Phi}{\partial t} \right)_{z=0} = \frac{\omega}{g} (\phi_1 \sin\omega t - \phi_2 \cos\omega t) \tag{5.4b}$$

where ϕ_1 and ϕ_2 are the real and imaginary parts of the complex potential $\phi(x, y)$

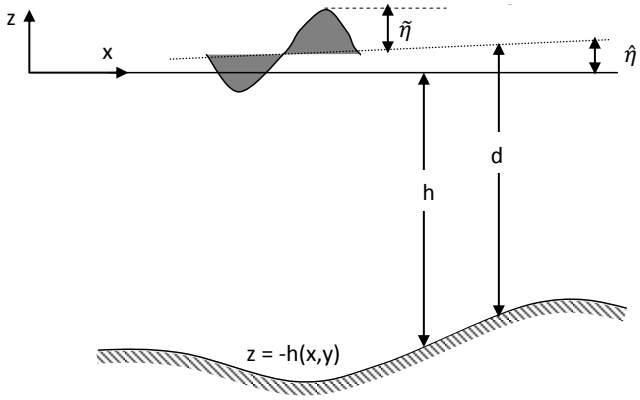

Figure 5.1: Wave field schematic.

respectively. The components of wave velocity $(\tilde{u}_\alpha, \tilde{w})$ and the dynamic pressure $\tilde{p_d}$ is defined using the following relations from linear wave theory:

$$(\tilde{u}_\alpha, \tilde{w}) = Re\left(\frac{\partial\phi}{\partial x_\alpha}\frac{\cosh k(h+z)}{\cosh kd}exp(-i\omega t), k\phi\frac{\sinh k(h+z)}{\cosh kd}exp(-i\omega t)\right) \tag{5.5}$$

$$\tilde{p}_d = -\rho\frac{\partial\phi}{\partial t} = \rho\omega\phi\frac{\cosh k(h+z)}{\cosh kd}\left(\phi_1 \sin\omega t - \phi_2 \cos\omega t\right) \tag{5.6}$$

where α, β denote the horizontal coordinates. Note that the above relations for wave quantities apply to any arbitrary linear wave field.

5.3 The Generalized Pressure Distribution

We develop an expression for pressure applicable to an arbitrary wave field. The pressure treatment is critical to the derivation of new generalized 3-D RST in the next section. We start with the z-direction momentum equation for irrotational and

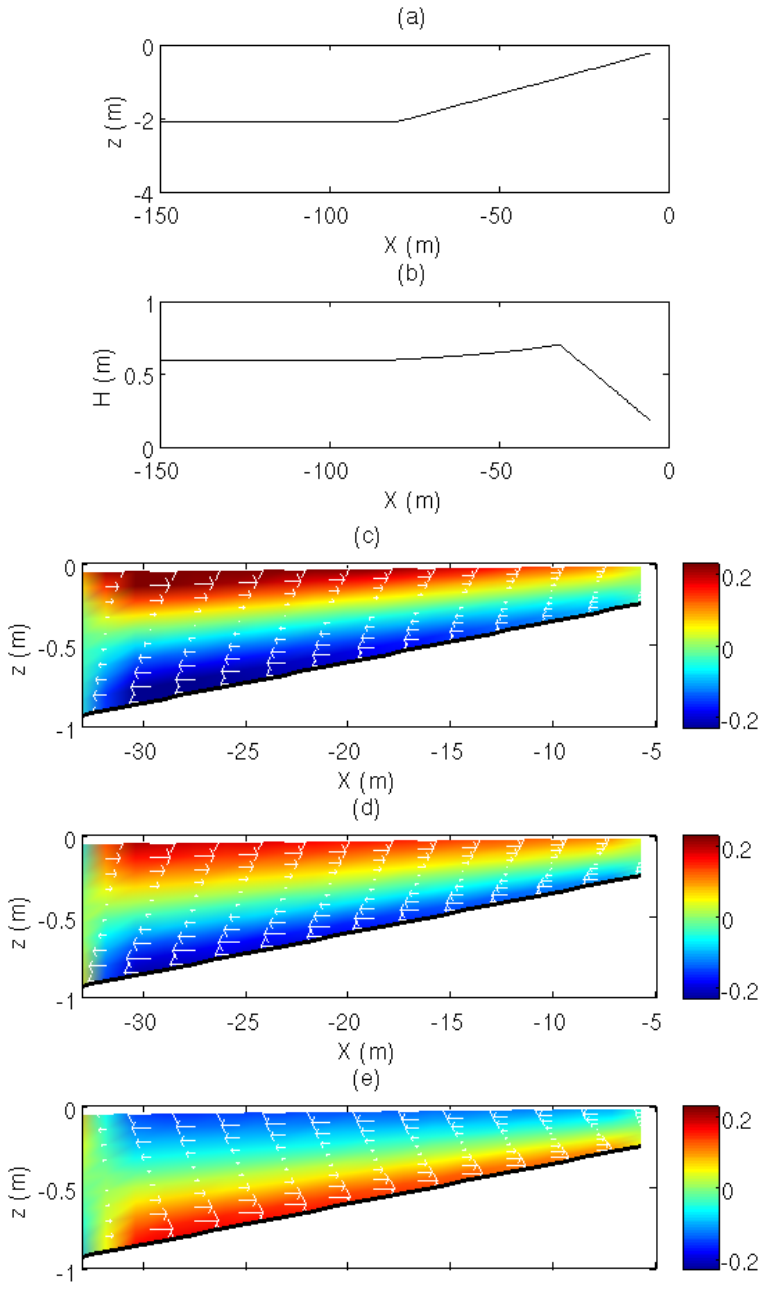

Figure 5.2: Bottom Profile (a) and Modeled wave height (b); Modeled current field using M11 (c), using L08 (d) and using M13 (e).

inviscid wave motion:

$$\frac{\partial \tilde{w}}{\partial t} + \frac{\partial}{\partial x_\beta}\left(\tilde{u}_\beta \tilde{w}\right) + \frac{\partial}{\partial z}\left(\tilde{w}^2\right) = -\frac{1}{\rho}\frac{\partial p}{\partial z} - g \qquad -h < z < \eta \tag{5.7}$$

where $(\tilde{u}_\alpha, \tilde{w})$ are the components of wave velocity. The total free surface elevation (η), as shown in Fig. 1, receives contributions from the waves $(\tilde{\eta})$ and the set-up/down $(\hat{\eta})$ such that $\eta = \hat{\eta} + \tilde{\eta}$. Wave quantities $(\tilde{u}_\alpha, \tilde{w})$ and $\tilde{\eta}$ may belong to an arbitrary wave field. The equation above is then vertically integrated from an arbitrary z to $z = \eta$ as follows:

$$\int_z^\eta \frac{\partial \tilde{w}}{\partial t} dz + \frac{1}{\rho}\int_z^\eta \frac{\partial p}{\partial z} dz + \int_z^\eta \frac{\partial}{\partial x_\beta}\left(\tilde{u}_\beta \tilde{w}\right) dz + \int_z^\eta \frac{\partial \tilde{w}^2}{\partial z} dz + \int_z^\eta g dz = 0 \quad -h < z < \eta \tag{5.8}$$

which simplifies by the application of Leibniz integral rule and kinematic free-surface BC to yield

$$p + \rho\tilde{w}^2 + \rho g(z - \eta) - \rho\frac{\partial}{\partial t}\int_z^\eta \tilde{w} dz - \rho\frac{\partial}{\partial x_\beta}\int_z^\eta \left(\tilde{u}_\beta \tilde{w}\right) dz = 0; \qquad -h < z < \eta. \tag{5.9}$$

Next, using periodicity of wave field, the equation above is wave-averaged to obtain

$$\overline{p} + \rho\overline{\tilde{w}^2} + \rho g(z - \hat{\eta}) - \rho\overline{\frac{\partial}{\partial x_\beta}\int_z^\eta \left(\tilde{u}_\beta \tilde{w}\right) dz} = 0; \qquad -h < z < \hat{\eta}$$

where the overbar denotes wave average (or time average over one wave cycle). The wave-averaged contribution due to the fourth term in Eq. (5.9) is nil. Since the second-order (in ka) integrand in the last term of the equation above has a higher-order (negligible) contribution in the region $-|\tilde{\eta}| < z - \hat{\eta} < |\tilde{\eta}|$, the upper limit of integration is changed from $z = \eta$ to $z = \hat{\eta}$ so that the averaging operator can be

transferred inside the integral:

$$\overline{p} + \rho\overline{\tilde{w}^2} + \rho g(z - \hat{\eta}) - \rho\frac{\partial}{\partial x_\beta}\int_z^{\hat{\eta}} \left(\overline{\tilde{u}_\beta \tilde{w}}\right) dz = O(\epsilon^3); \qquad -h < z < \hat{\eta}. \tag{5.10}$$

Note that the pressure treatment in the equations above mostly follows [24], [23], [36]. In contrast, Mellor ([36, 37, 44]) did not include the last term on the LHS in Eq. (5.10) by assuming wave field to be purely progressive. Here we do not employ any such assumption regarding the nature of the wave field so that generality is preserved. Moreover, for the development of 3-D RSTs for progressive waves, different approaches for pressure treatment have been used. To obtain M13, Mellor [44] used an approximation of Eq. (5.9) to define pressure in the region $-h \leq z \leq \eta$. Mellor [37] and Lin [46] used Eq. (5.10) in combination with hydrostatic assumption (in the region $-|\tilde{\eta}| < z - \hat{\eta} < |\tilde{\eta}|$) to obtain M11 and L08 respectively.

5.4 The Generalized Vertically Dependent RST

We derive the vertically dependent generalized RSTs (in terms of the complex potential ϕ) applicable to an arbitrary linear wave field. The derivation process mostly follows Mellor [33, 44] who developed a coupled wave-current system in terms of mean drift velocity (Eulerian current plus the Stokes Drift).

We start with the conservation equations

$$\frac{\partial u_\alpha}{\partial x_\alpha} + \frac{\partial w}{\partial z} = 0, \tag{5.11}$$

$$\frac{\partial u_\alpha}{\partial t} + \frac{\partial}{\partial x_\beta}\left(u_\alpha u_\beta\right) + \frac{\partial}{\partial z}\left(u_\alpha w\right) = -\frac{1}{\rho}\frac{\partial p}{\partial x} \quad \text{and} \tag{5.12}$$

$$\frac{\partial w}{\partial t} + \frac{\partial}{\partial x_\beta}\left(u_\beta w\right) + \frac{\partial}{\partial z}\left(w^2\right) = -\frac{1}{\rho}\frac{\partial p}{\partial z} - g, \tag{5.13}$$

where $x_\alpha \equiv (x, y)$; $u_\alpha = \hat{u}_\alpha + \tilde{u}_\alpha$; $w = \hat{w} + \tilde{w}$; $(\hat{u}_\alpha, \hat{w})$ are the components of current

velocity and $(\tilde{u}_\alpha, \tilde{w})$ are the components of wave velocity. For convenience, Coriolis, baroclinic, pressure-slope transfer and turbulent-mixing effects are ignored in this section.

Next, to obtain flow equations in terms of mean drift velocity as in [33] and [44], we use the following transformation that maps Cartesian coordinates (x_α, z, t) to wave-following coordinates $(x^*_\alpha, \bar{z}, t^*)$:

$$x_\alpha = x^*_\alpha, \tag{15a}$$

$$t = t^* \quad \text{and} \tag{15b}$$

$$z = s(x^*_\alpha, \bar{z}, t^*), \tag{15c}$$

where

$$s(x^*_\alpha, \bar{z}, t^*) = \bar{z} + \tilde{s} \quad \text{and} \tag{15d}$$

$$\tilde{s} = \int \tilde{w} dt; \tag{15e}$$

s defines a material surface, and $\tilde{s}$ is the vertical displacement of material surface due to waves. $s = \hat{\eta} + \tilde{\eta}$ for $\bar{z} = \hat{\eta}$ and $s = -h$ for $\bar{z} = -h$. The transformation is same as the one used in [33] and [44] except for two minor differences: (1) $\bar{z}$ in Eqs.(15a-15e) is equivalent to $\hat{\eta} + \sigma D$ in [44], and (2) $\tilde{s}$ in Eq. (15e) corresponds to an arbitrary wave field, not simply to a progressive wave field as in [33] and [44]. Based on the transformation, any quantity $\psi(x_\alpha, z, t)$ can be transformed to $\psi^*(x^*_\alpha, s, t^*)$ using

$$\frac{\partial \psi}{\partial t} = \frac{\partial \psi^*}{\partial t^*} - \frac{\partial \psi^*}{\partial \bar{z}} \frac{s_t}{s_{\bar{z}}}, \tag{5.16}$$

$$\frac{\partial \psi}{\partial x_\alpha} = \frac{\partial \psi^*}{\partial x^*_\alpha} - \frac{\partial \psi^*}{\partial \bar{z}} \frac{s_x}{s_{\bar{z}}} \quad \text{and} \tag{5.17}$$

$$\frac{\partial \psi}{\partial z} = \frac{\partial \psi^*}{\partial \bar{z}} \frac{1}{s_{\bar{z}}}, \tag{5.18}$$

where $s_t = \partial s/\partial t = \partial \tilde{s}/\partial t$; $s_{\bar{z}} = \partial s/\partial \bar{z} = (1 + \partial \tilde{s}/\partial \bar{z})$ and $s_\alpha = \partial s/\partial x_\alpha = (\partial \bar{z}/\partial x_\alpha + \partial \tilde{s}/\partial x_\alpha)$. (Detailed derivation of Eqs. (5.16-5.18) can be found in [44]. For convenience, we drop asterisks.

Next, using the transformation relations given in Eqs. (5.16-5.18), the flow equations (Eqs. 5.11-5.13) are first transformed and then wave-averaged to yield

$$\frac{\partial s_{\bar{z}}}{\partial t} + \frac{\partial s_{\bar{z}} u_\alpha}{\partial x_\alpha} + \frac{\partial w'}{\partial \bar{z}} = 0 \tag{5.19}$$

$$\frac{\partial}{\partial t}\left(\overline{s_{\bar{z}} u_\alpha}\right) + \frac{\partial}{\partial x_\beta}\left(\overline{s_{\bar{z}} u_\alpha u_\beta}\right) + \frac{\partial}{\partial \bar{\bar{z}}}\left(\overline{u_\alpha w'}\right) = -\frac{1}{\rho}\frac{\partial}{\partial x_\alpha}\left(\overline{p s_{\bar{z}}}\right) + \frac{1}{\rho}\frac{\partial}{\partial \bar{z}}\left(\overline{p s_\alpha}\right) \tag{5.20}$$

where $w = w' + u_\alpha s_\alpha + s_t$ is defined following Mellor [33, 44]. (Similar equations in terms of sigma-coordinates are given in Mellor [44]). Next, we use the following relations from Mellor [44]:

$$\overline{s_{\bar{z}} u_\alpha} = U_\alpha, \tag{5.21}$$

$$\overline{s_{\bar{z}} u_\alpha u_\beta} = U_\alpha U_\beta + \overline{\tilde{u}_\alpha \tilde{u}_\beta} \quad \text{and} \tag{5.22}$$

$$\overline{w' u_\alpha} = \Omega U_\alpha, \tag{5.23}$$

where $U_\alpha = \hat{u}_\alpha + u_{s\alpha}$ is the horizontal mean drift velocity; $u_{s\alpha}$ is the Stokes Drift given by $u_{s\alpha} = \partial \overline{\tilde{u}_\alpha \tilde{s}}/\partial \bar{z}$. Inserting Eqs. (5.21-5.23) into Eqs. (5.19-5.20), we get the following set of flow equations:

$$\frac{\partial \hat{\eta}}{\partial t} + \frac{\partial U_\alpha}{\partial x_\alpha} + \frac{\partial w'}{\partial \bar{z}} = 0, \tag{5.24}$$

$$\frac{\partial U_\alpha}{\partial t} + \frac{\partial}{\partial x_\beta}\left(U_\alpha U_\beta\right) + \frac{\partial}{\partial z}\left(U_\alpha w'\right) = -\left(\frac{1}{\rho}\frac{\partial}{\partial x_\alpha}\left(\overline{p s_{\bar{z}}}\right) - \frac{1}{\rho}\frac{\partial}{\partial \bar{z}}\left(\overline{p s_\alpha}\right)\right) - \frac{\partial}{\partial x_\beta}\left(\tilde{u}_\alpha \tilde{u}_\beta\right). \tag{5.25}$$

So far the development of above equations is general. Now we consider different approaches for pressure treatment and simplify the RHS in Eq. (5.25). This leads to the new expressions for generalized 3-D RSTs. The approaches used by Mellor [44, 37] and Lin [46] are considered for pressure treatment, and the respective RSTs are hereinafter referred to as $S_{\alpha\beta}^{M13}$, $S_{\alpha\beta}^{M11}$ and $S_{\alpha\beta}^{L08}$.

5.4.1 Expression for $S_{\alpha\beta}^{M13}$

Mellor (2013a) simplified the last two terms in Eq. (5.9) using linear wave theory and obtained an expression for pressure applicable in the region $-h \leq z \leq \eta$. (The procedure applied by Mellor is equivalent to using Taylor's series approach for small amplitude waves). Following his approach, an expression for pressure applicable to arbitrary linear waves is obtained:

$$p = \rho g(\hat{\eta} - z) - \rho\tilde{w}^2 + \tilde{p}_d + \rho\frac{\partial}{\partial x_\beta}\int_z^{\hat{\eta}} (\tilde{u}_\beta\tilde{w})\, dz + \rho\frac{\partial}{\partial t}(w\tilde{\eta})\bigg|_{z=0} \tag{5.26}$$

where $\tilde{p}_d$ is the dynamic pressure given by Eq. (5.6). For any arbitrary wave field, the last term vanishes when wave-averaged. The integral term, however, vanishes on wave-averaging only for linear progressive waves.

Next, following Mellor [44], the transformed pressure in wave-following coordinates is given by

$$p = \rho g(\hat{\eta} - \bar{z}) - \rho g\tilde{s} - \rho\tilde{w}^2 + \left(\tilde{p}_d + \frac{\partial\tilde{p}_d}{\partial\bar{z}}\tilde{s}\right) + \rho\frac{\partial}{\partial x_\beta}\int_{\bar{z}}^{\hat{\eta}} \left(\overline{\tilde{u}_\beta\tilde{w}}\right) d\bar{z}, \tag{5.27}$$

which is then used to obtain

$$\overline{s_{\bar{z}}p} = \rho g(\hat{\eta} - \bar{z}) - \rho\tilde{w}^2 + \rho\frac{\partial}{\partial x_\beta}\int_{\bar{z}}^{\hat{\eta}} \left(\overline{\tilde{u}_\beta\tilde{w}}\right) d\bar{z} + \frac{\partial}{\partial\bar{z}}\left(\overline{\tilde{p}_d\tilde{s}} - \frac{g\overline{\tilde{s}^2}}{2}\right) \quad \text{and} \tag{5.28}$$

$$\overline{s_\alpha p} = \rho g(\hat{\eta} - \bar{z})\frac{\partial \bar{z}}{\partial x_\alpha} + \rho \frac{\partial \bar{z}}{\partial x_\alpha}\frac{\partial}{\partial x_\beta}\int_{\bar{z}}^{\hat{\eta}} \overline{\tilde{u}_\beta \tilde{w}} d\bar{z}. \tag{5.29}$$

Using these relations and after considerable algebra, the RHS of Eq. (5.25) is simplified in the form

$$-\frac{1}{\rho}\frac{\partial}{\partial x_\alpha}\left(\overline{ps_{\bar{z}}}\right) + \frac{1}{\rho}\frac{\partial}{\partial \bar{z}}\left(\overline{ps_\alpha}\right) - \frac{\partial}{\partial x_\beta}\left(\tilde{u}_\alpha \tilde{u}_\beta\right) = -g\frac{\partial \hat{\eta}}{\partial x_\alpha} - \frac{1}{\rho}\frac{\partial S^{M13}_{\alpha\beta}}{\partial x_\beta} + \rho \frac{\partial \bar{z}}{\partial x_\alpha}\frac{\partial}{\partial \bar{z}}\left(\frac{\partial}{\partial x_\beta}\int_{\bar{z}}^{\hat{\eta}} \overline{\tilde{u}_\beta \tilde{w}} d\bar{z}\right) \tag{5.30}$$

where

$$S^{M13}_{\alpha\beta} = \rho\left\{\left(\overline{\tilde{u}_\alpha \tilde{u}_\beta} - \delta_{\alpha\beta}\overline{\tilde{w}^2}\right) + \delta_{\alpha\beta}\int_z^{\hat{\eta}} \frac{\partial}{\partial x_\beta}\left(\overline{\tilde{u}_\beta \tilde{w}}\right) dz\right\} + \frac{\partial}{\partial \bar{z}}\left(\overline{\tilde{p}_d \tilde{s}} - \frac{g\overline{\tilde{s}^2}}{2}\right) \tag{5.31}$$

is the generalized 3-D RST obtained using the approach suggested by Mellor [44]. Notice that, in comparison to the other terms on the RHS of Eq. (5.31), the last term in Eq. (5.31) can be ignored. This is true for most coastal applications, because $\partial \bar{z}/\partial x_\alpha$ which is proportional to $\partial h/\partial x_\alpha$ at the bottom and $\partial \hat{\eta}/\partial x_\alpha$ on the surface, is usually small. For linear progressive waves, and for flat bottom cases, this term always vanishes.

On substituting Eqs. (5.30-5.31) into Eqs. 5.24-5.25), the flow equations similar to those in [44] are obtained. However, unlike [44], the expression for $S^{M13}_{\alpha\beta}$ given above is valid for an arbitrary linear wave field. For linear progressive waves over flat bottom (i.e. wave quantities obtained using Airy's theory), $S^{M13}_{\alpha\beta}$ transforms to M13.

Recall that M13 could not produce satisfactory results for the sloping beach case in Section 2. It may, therefore, be argued that the expression for $S^{M13}_{\alpha\beta}$ given above is also not adequate for arbitrary linear waves. The following hypothesis is given here to address this issue: Any vertical water column is comprised of two regions,

namely Region 1: $-h \leq z \leq 0$, and Region 2: $-|\tilde{\eta}| < z - \hat{\eta} < |\tilde{\eta}|$. It is clear form the derivation above that the second and the third term inside curly bracket in $S_{\alpha\beta}^{M13}$ corresponds to wave-averaged pressure contribution in Region 1, whereas, the last term corresponds to wave-averaged pressure contribution in Region 2. (The term $\overline{\tilde{u}_\alpha \tilde{u}_\beta}$ does not directly relate to pressure). The last term in M13 is an estimate of the last term in Eq. (5.31) using Airy's theory. As discussed earlier in Section 2, the last term in Eq. (5.1) for M13, which also corresponds to the pressure contribution in Region 2, is the source of spurious behavior in the sloping beach case. Therefore, it seems the use of Airy's theory to obtain pressure contribution in Region 2 is perhaps problematic. In fact, this hypothesis is also supported by Bennis et al. [**?**] who stated that Airy's theory does not correctly estimate terms such as $\tilde{p}_d \tilde{s}$; they in fact suggested using more sophisticated wave models (e.g. [**?**].

In summary, it is possible that the expression for $S_{\alpha\beta}^{M13}$ in Eq. (5.31) is correct, but it certainly does not work in the framework of linear theory. However, we do not have any proof for this conjecture, and since the present study is based on linear wave theory, we do not consider Eq. (5.31) further in this paper. Instead, we develop the generalized forms of M11 and L08 in the following discussion.

5.4.2 Expression for $S_{\alpha\beta}^{M11}$

Mellor (2011) used Eqs. (5.9, 5.10) for pressure treatment. To account for the pressure contribution in Region 2, they employed hydrostatic assumption as used by Longuet-Higgins and Stewart [23] and Bettess and Bettess [24]. Using Mellor's approach, one can express the RHS of Eq. (5.25) in the form

$$-\frac{1}{\rho}\frac{\partial}{\partial x_\alpha}\left(\overline{ps_{\tilde{z}}}\right) + \frac{1}{\rho}\frac{\partial}{\partial \bar{z}}\left(\overline{ps_\alpha}\right) - \frac{\partial}{\partial x_\beta}\left(\overline{\tilde{u}_\alpha \tilde{u}_\beta}\right) = T^{(1)} + T^{(2)} \tag{5.32}$$

where $T^{(1)}$ and $T^{(2)}$ pertain to the pressure contributions in Region 1 and Region 2 respectively. In wave-following coordinates, $T^{(1)}$ can easily be estimated by setting $\tilde{s} = 0$ (i.e. by excluding Region 2) in the RHS of Eq. (5.25) such that

$$T^{(1)} = -\frac{1}{\rho}\frac{\partial \overline{p}}{\partial x_\alpha} + \frac{1}{\rho}\frac{\partial \bar{z}}{\partial x_\alpha}\frac{\partial \overline{p}}{\partial \bar{z}} - \frac{\partial}{\partial x_\beta}\left(\overline{\tilde{u}_\alpha \tilde{u}_\beta}\right). \tag{5.33}$$

However, the development of term $T^{(2)}$, which corresponds to hydrostatic pressure contribution in Region 2, requires special treatment. Following Mellor [37], $T^{(2)}$ is defined in the form of a surface singular term:

$$T^{(2)} = -\frac{\partial E_D^{M11}}{\partial x_\alpha} \tag{5.34}$$

where E_D^{M11} relates to the wave-averaged integral of hydrostatic pressure

$$\overline{\int_{\hat{\eta}}^{\hat{\eta}+\tilde{\eta}} \rho g\,(\eta - z)\,dz} = \rho g \frac{\overline{\tilde{\eta}^2}}{2} \tag{5.35}$$

such that

$$E_D^{M11} = 0 \text{ if } \bar{z} \neq \hat{\eta}, \text{ and } \int_{-h}^{\hat{\eta}+} E_D^{M11} d\bar{z} = \frac{1}{2}\rho g \overline{\tilde{\eta}^2}.$$

After inserting $T^{(1)}$ and $T^{(2)}$ from Eqs. (5.33-5.34), and wave-averaged pressure $\overline{p}$ from Eq. (5.10), one obtains the RHS of Eq. (5.25) as

$$-\frac{1}{\rho}\frac{\partial}{\partial x_\alpha}\left(\overline{p s_{\bar{z}}}\right) + \frac{1}{\rho}\frac{\partial}{\partial \bar{z}}\left(\overline{p s_\alpha}\right) - \frac{\partial}{\partial x_\beta}\left(\overline{\tilde{u}_\alpha \tilde{u}_\beta}\right) = -g\frac{\partial \hat{\eta}}{\partial x_\alpha} - \frac{\partial S_{\alpha\beta}^{M11}}{\partial x_\alpha} + \rho \frac{\partial \bar{z}}{\partial x_\alpha}\frac{\partial}{\partial \bar{z}}\left(-\delta_{\alpha\beta}\overline{\tilde{w}^2} + \frac{\partial}{\partial x_\beta}\int_{\bar{z}}^{\hat{\eta}} \overline{\tilde{u}_\beta \tilde{w}} d\bar{z}\right) \tag{5.36}$$

where

$$S_{\alpha\beta}^{(M11)} = \rho\left\{\left(\overline{\tilde{u}_\alpha \tilde{u}_\beta} - \delta_{\alpha\beta}\overline{\tilde{w}^2}\right) + \delta_{\alpha\beta}\int_z^0 \frac{\partial}{\partial x_\beta}\left(\overline{\tilde{u}_\beta \tilde{w}}\right) dz\right\} + \delta_{\alpha\beta} E_D^{M11} \tag{5.37}$$

is the generalized 3-D RST obtained following Mellor [37]. It can be considered as the generalized form of M11. As discussed earlier with regards to Eq. (5.30), the last term in Eq. (5.36) is negligible for most coastal applications. (Similar term is present in [37]).

5.4.3 Expression for $S_{\alpha\beta}^{L08}$

The treatment of pressure in Lin [46] is same as in Mellor (2011); therefore, one can define RHS of Eq. (5.25) in the form of Eq. (5.32). The term $T^{(1)}$ is once again given by Eq. (5.33); however, the development of $T^{(2)}$ differs from [37]. Note that $T^{(2)}$ in Eq. (5.34) is a surface singular term, and the definition of wave-averaged integral (Eq. 5.35) in [37] is not consistent with the wave-following coordinate system. This has been debated by some researchers. Following Lin [46], here we obtain a new expression for $T^{(2)}$ in the form

$$T^{(2)} = -\frac{\partial E_D^{L08}}{\partial x_\alpha} \tag{5.38}$$

where E_D^{L08} relates to the following wave-averaged integral defined by Lin [46]:

$$Z = \overline{\int_{\hat{\bar{z}}}^{s} \rho g\,(s-\bar{z})\,dz'} = \rho g \frac{\overline{\tilde{\bar{s}}^2}}{2} = \rho g \frac{\overline{\tilde{\bar{\eta}}^2}}{2} \frac{\sinh^2 k\,(\bar{z}+h)}{\sinh^2 kd} \tag{5.39}$$

such that

$$E_D^{L08} = \frac{\partial Z}{\partial \bar{z}} = \rho g \frac{\overline{\tilde{\bar{\eta}}^2}}{2} \frac{k \sinh 2k\,(\bar{z}+h)}{\sinh^2 kd}. \tag{5.40}$$

Using the above expression for $T^{(2)}$ with $T^{(1)}$ from Eq. (5.33), one can get an

equation similar to Eq. (5.36); $S_{\alpha\beta}^{M11}$ must be replaced by $S_{\alpha\beta}^{L08}$ given in the form

$$S_{\alpha\beta}^{L08} = \rho\left\{\left(\overline{\tilde{u}_\alpha\tilde{u}_\beta} - \delta_{\alpha\beta}\overline{\tilde{w}^2}\right) + \delta_{\alpha\beta}\rho\int_z^0 \frac{\partial}{\partial x_\beta}\left(\overline{\tilde{u}_\beta\tilde{w}}\right)dz\right\} + \delta_{\alpha\beta}\left\{\rho g\frac{\overline{\tilde{\tilde{\eta}}^2}}{2}\frac{k\sinh 2k\,(\bar{z}+h)}{\sinh^2 kD}\right\}. \tag{5.41}$$

$S_{\alpha\beta}^{L08}$ can be considered as the generalized form of L08.

Once the generalized forms of M11 and L08 are derived, we can define these new generalized RSTs in the form similar to Eq. (5.1):

$$S_{\alpha\beta} = \rho\left\{\left(\overline{\tilde{u}_\alpha\tilde{u}_\beta} - \delta_{\alpha\beta}\overline{\tilde{w}^2}\right) + \delta_{\alpha\beta}\rho\int_z^0 \frac{\partial}{\partial x_\beta}\left(\overline{\tilde{u}_\beta\tilde{w}}\right)dz\right\} + \delta_{\alpha\beta}\Im(\bar{z}), \tag{5.42}$$

where $\Im(\bar{z}) = E_D^{M11}$ for $S_{\alpha\beta}^{M11}$, and $\Im(\bar{z}) = E_D^{L08}$ for $S_{\alpha\beta}^{M08}$.

Finally, to obtain a simplification of $S_{\alpha\beta}$, we separate the terms in $S_{\alpha\beta}$ and express them (using Eqs. 5.4b and 5.5) in terms of the wave solution ϕ from the elliptic wave model as follows:

$$\rho\left(\overline{\tilde{u}_\alpha\tilde{u}_\beta} - \delta_{\alpha\beta}\overline{\tilde{w}^2}\right) = \frac{\rho}{2}\left\{\left(\frac{\partial\phi}{\partial x_\alpha}\frac{\partial\phi^*}{\partial x_\beta} + \frac{\partial\phi^*}{\partial x_\alpha}\frac{\partial\phi}{\partial x_\beta}\right)\frac{\cosh^2 k(h+\bar{z})}{2\cosh^2 kd} - \delta_{\alpha\beta}k^2\phi\phi^*\frac{\sinh^2 k(h+\bar{z})}{\cosh^2 kd}\right\},$$

$$\rho\int_{\bar{z}}^{\hat{\eta}} \frac{\partial}{\partial x_\beta}\left(\overline{\tilde{u}_\beta\tilde{w}}\right)d\bar{z} = \frac{\rho}{8}\left(\frac{\partial}{\partial x_\beta}\left(A\frac{\partial\phi\phi^*}{\partial x_\beta}\right)\right)$$

where

$$A = \frac{\cosh 2kd - \cosh 2k(h+\bar{z})}{\cosh^2 kd},$$

and

$$\frac{1}{2}\rho g\overline{\tilde{\eta}^2} = \frac{\rho}{4}\frac{\omega^2}{g}\phi\phi^*.$$

The above terms are substituted back into Eq. (5.42) to get the final expression

for the vertically dependent RST given by

$$S_{\alpha\beta}^{G3D} = \frac{\rho}{2}\left\{\left(\frac{\partial\phi}{\partial x_\alpha}\frac{\partial\phi^*}{\partial x_\beta}+\frac{\partial\phi^*}{\partial x_\alpha}\frac{\partial\phi}{\partial x_\beta}\right)\frac{\cosh^2 k(h+\bar{z})}{2\cosh^2 kd}\right.$$
$$\left. - \delta_{\alpha\beta}k^2\phi\phi^*\frac{\sinh^2 k(h+\bar{z})}{\cosh^2 kd}\right\} + \delta_{\alpha\beta}\frac{\rho}{8}\left(\frac{\partial}{\partial x_\beta}\left(A\frac{\partial\phi\phi^*}{\partial x_\beta}\right)\right) + \delta_{\alpha\beta}\Im(\bar{z}) \tag{5.43}$$

where $\Im(\bar{z}) = E_D^{M11}$ for $S_{\alpha\beta}^{M11}$, and $\Im(\bar{z}) = E_D^{L08}$ for $S_{\alpha\beta}^{M08}$ where

$$E_D^{M11}= 0 \text{ if } \bar{z}\neq\hat{\eta}, \text{ and } \int_{-h}^{\hat{\eta}+} E_D^{M11}d\bar{z}=\frac{\rho}{4}\frac{\omega^2}{g}\phi\phi^*.$$

$$E_D^{L08} = \frac{\rho}{4}\frac{\omega^2}{g}\phi\phi^*\frac{k\sinh 2k\,(\bar{z}+h)}{\sinh^2 kd}.$$

5.5 Relation to Other Formulations

In this section, we relate the generalized formulation ($S_{\alpha\beta}^{G3D}$ in Eq. 5.43) with other 3-D as well as 2-D RSTs mentioned earlier in Section 1.

5.5.1 RST for Progressive Wave

For forward propagating waves over a flat bottom, expressed analytically using $\tilde{\eta}(t) = a_0\cos(kx-\omega t)$ (where a_0 = wave amplitude), Eq. (5.4b) yields the complex potential

$$\phi = \frac{a_0 g}{\omega}\,(\sin kx\cos\omega t - \cos kx\sin\omega t), \tag{5.44}$$

and on substitution in $S_{\alpha\beta}^{G3D}$ (Eq. 5.43), results in $S_{\alpha\beta}$ for M11 and L08 given by Eq. (5.1). (σ in Eq. 5.1 is related to $\bar{z}$ using $\bar{z} = \hat{\eta} + \sigma d$).

In particular, for a progressive wave field, the second term on the RHS of Eq. (5.43) vanishes, and the first term is uniformly distributed (independent of z) along the vertical direction. Moreover, the vertical integration of Eq. (5.43) yields the

standard 2-D RST of Longuet-Higgins and Stewart [23]:

$$S_{\alpha\beta}^{(2D)} = \left[\frac{k_\alpha k_\beta}{k^2}\frac{c_g}{c_p} + \delta_{\alpha\beta}\left(\frac{c_g}{c_p} - \frac{1}{2}\right)\right] E. \tag{5.45}$$

5.5.2 RST for Arbitrary Wave Field

For an arbitrary linear wave field, the G3D formulation can be seen as a 3-D extension of the 2-D BB2D formulation of [24]. When vertically integrated, G3D yields

$$S_{\alpha\beta}^{(G2D)} = \frac{\rho}{8}\left(\frac{\sinh 2kd + 2kd}{2k\cosh^2 2kd}\right)\left(\frac{\partial\phi}{\partial x_\alpha}\frac{\partial\phi^*}{\partial x_\beta} + \frac{\partial\phi^*}{\partial x_\alpha}\frac{\partial\phi}{\partial x_\beta}\right) + \delta_{\alpha\beta}\frac{\rho}{8}\left(\frac{\partial}{\partial x_\beta}\left(B\frac{\partial\phi\phi^*}{\partial x_\beta}\right)\right) + \delta_{\alpha\beta}\frac{\rho}{8}\left(\frac{2kd}{k\cosh^2 2kd}\right)k^2\left(\phi\phi^*\right) \tag{5.46}$$

where

$$B = \left(\frac{\cosh 2kd - \dfrac{\sinh 2kd}{2kd}}{k\cosh^2 2kd}\right),$$

which matches with BB2D, if the term B in Eq. (5.46) is constant over the domain, as in [24]. Since this is true only for domains with flat bottom, here we use more general Eq. (5.46) as a substitute for BB2D for subsequent numerical calculations.

5.5.3 RST for Full/Partial Standing Wave Field

For full/partial standing waves over a flat bottom, an expression for 3-D RST is not available in the literature. Although, for full standing waves, an effort was made by Zhang and Liu [56], they used the inconsistent approach proposed by Xia et al. [32]; also their treatment of the pressure term is erroneous (see discussion later). Using the general nature of G3D, a 3-D RST for full/partial standing waves over flat bottom, expressed analytically using $\tilde{\eta}(t) = Re\left(a_0 e^{i(kx-\omega t)} + Ra_0 e^{i(kx+\omega t)}\right)$ (where

R is reflection coefficient and a_0 is the amplitude of forward-propagating wave), is developed here. For this wave field, Eq. (5.4b) yields complex potential

$$\phi = \frac{a_0 g}{\omega} \{(1-R)\sin kx \cos \omega t - (1+R)\cos kx \sin \omega t\} \tag{5.47}$$

which on substitution in Eq. (5.43) gives

$$\begin{aligned} S_{\alpha\beta} = \rho g a_0^2 k \Bigg\{ & \frac{(1+R^2-2R\cos 2kx)\cosh^2 k(h+\bar{z})}{\sinh 2kd} - \delta_{\alpha\beta}\frac{(1+R^2+2R\cos 2kx)\sinh^2 k(h+\bar{z})}{\sinh 2kd} \\ & - \delta_{\alpha\beta}\left(\frac{\cosh 2kd - \cosh 2k(h+\bar{z})}{\sinh 2kd}\right) R\cos 2kx \Bigg\} + \delta_{\alpha\beta}\Im_S(\bar{z}) \end{aligned} \tag{5.48}$$

where $\Im_S(\bar{z}) = E_{DS}^{M11}$ following Mellor [37], and $\Im_S(\bar{z}) = E_{DS}^{L08}$ following Lin [46] where

$$E_{DS}^{M11} = 0 \text{ if } \bar{z} \neq \hat{\eta}, \text{ and } \int_{-h}^{\hat{\eta}+} E_D^{M11} d\bar{z} = \frac{\rho g a_0^2}{4}(1+R^2+2R\cos 2kx).$$

$$E_{DS}^{L08} = \frac{\rho g a_0^2}{4}(1+R^2+2R\cos 2kx)\frac{k\sinh 2k\,(\bar{z}+h)}{\sinh^2 kd}.$$

For $R = 0$, the above RST expression simplifies to M11, and for $R = 1$, it gives an RST expression for full standing waves over flat bottom which vertically integrates to yield the standard 2-D radiation stress components ($S_{xx}^{(2D)}, S_{xy}^{(2D)}, S_{yx}^{(2D)}$ and $S_{yy}^{(2D)}$) for standing waves (e.g. [54]) expressed as

$$S_{xx}^{(2D)} = \frac{1}{2}\rho g a^2 \left[1 + \frac{4kh}{sin2kh} - 2\coth 2kh \cos 2kx\right] \tag{5.49}$$

$$S_{yy}^{(2D)} = \frac{1}{2}\rho g a^2 \left[-\cos 2kx + \frac{4kh}{sin2kh}\sin^2 kx + 2\coth 2kh \cos 2kx\right] \tag{5.50}$$

$$S_{xy}^{(2D)} = S_{yx}^{(2D)} = 0 \tag{5.51}$$

It should be noted that the last term in the brackets on the RHS of Eq. (5.48) contributes to the total wave-induced forcing for full/partial standing waves ($R \neq 0$), but as mentioned earlier, it vanishes in the case of progressive waves ($R = 0$). A heuristic explanation may be provided for this as follows: this term physically means that some weight of the water column is transferred to the neighboring columns through the water motion. In the case of forward propagating waves, it has been suggested (Svendsen 2006; Longuet-Higgins and Stewart 1962) that this is not possible over a long period and each water column just carries its own weight; therefore, in the wave-averaged sense, this term is negligible for progressive waves. However, when the wave field is not purely progressive (e.g. for a standing wave), an individual water column may help carry the weight of neighboring water columns.

6. MODELING THREE-DIMENSIONAL WAVE-INDUCED FLOW

A brief discussion pertaining to the salient features of the 3-D circulation model used here is provided in Section 6.1. Application of the coupled system (the elliptic model, the new RST, and the circulation model) is described in Section 6.2 to examine wave-induced flow fields (set-up/down and currents) for a series of test cases involving wave reflection and diffraction. Summary and Conclusions are provided in Section 6.3.

6.1 3-D Flow Model

The wave-induced flow field driven by the 3-D RST is simulated using the EFDC model which has been widely used ([90], [89], [92], [91]) to simulate 3-D circulation, transport of pollutants and sediments in rivers and nearshore regions. The model solves the 3-D, vertically hydrostatic, turbulence-averaged equations of motion using Cartesian or curvilinear coordinates in the horizontal and sigma coordinates in the vertical. Various options for bottom friction, turbulence closure, wetting-drying are available. The model is characterized by the following set of equations:

$$\frac{\partial \hat{\eta}}{\partial t} + \frac{\partial U_\alpha d}{\partial x_\alpha} + \frac{\partial w'}{\partial \sigma} = 0 \tag{6.1}$$

$$\frac{\partial U_\alpha d}{\partial t} + \frac{\partial U_\alpha U_\beta d}{\partial x_\beta} + \frac{\partial U_\alpha w'}{\partial \sigma} + gd\frac{\partial \hat{\eta}}{\partial x_\alpha} = \frac{\partial}{\partial \sigma}\left(\frac{K_M}{d}\frac{\partial \hat{u}_\alpha}{\partial \sigma}\right) + \frac{\partial}{\partial x_\beta}\left[A_M d\left(\frac{\partial U_\alpha}{\partial x_\beta} + \frac{\partial U_\beta}{\partial x_\alpha}\right)\right] - \frac{F_\alpha(\sigma)}{\rho} \tag{6.2}$$

where $U_\alpha = \hat{u}_\alpha + u_{s\alpha}$ is the horizontal component of the mean flow velocity; w' is the vertical component of flow velocity in sigma coordinates; $\hat{\eta}$ is the surface elevation; $d = h + \hat{\eta}$ is total water depth; A_M and K_M are the horizontal and vertical eddy viscosity respectively. As suggested by Mellor [45], the vertical velocity gradient in the turbulent mixing term is $\partial\hat{u}_\alpha/\partial\sigma$ (not $\partial U_\alpha/\partial\sigma$). More details regarding the parameters A_M and K_M are available in [32]. In EFDC, the wave-induced forcing F_α is typically applied only on the surface (analogous to wind forcing). To accommodate depth-varying forcing at different sigma layers ($-1 \leq \sigma \leq 0$), here $F_\alpha(\sigma)$ is described as

$$F_\alpha(\sigma) = -\frac{\partial(dS_{\alpha\beta}(\sigma))}{\partial x_\beta}; \tag{6.3}$$

the expression for $S_{\alpha\beta}(\sigma)$ in terms of the sigma coordinates can be obtained by replacing $\bar{z}$ with $\hat{\eta} + \sigma d$ in Eq. (5.43).

The EFDC model can be used in single-layer or multi-layer modes to simulate 2DH and 3-D flow fields respectively. Using the EFDC model and the elliptic wave model, a coupled wave-current system is developed. (Only the "one-way" coupling between the wave model and the EFDC model is considered, i.e. the effect of currents on the waves is ignored.)

6.2 Validation

To investigate the performance of the generalized formulation (Eq. 5.43) with the coupled system, a number of cases covering many practical situations often encountered in coastal/harbor engineering applications are considered. They involve: (1) undertow due to a wave propagating over a plane beach; (2) wave-induced circulation associated with a standing wave; and (3) wave-induced flow around a detached breakwater with significant reflection, diffraction and breaking effects. The modeled results are compared with experimental data and results obtained using other

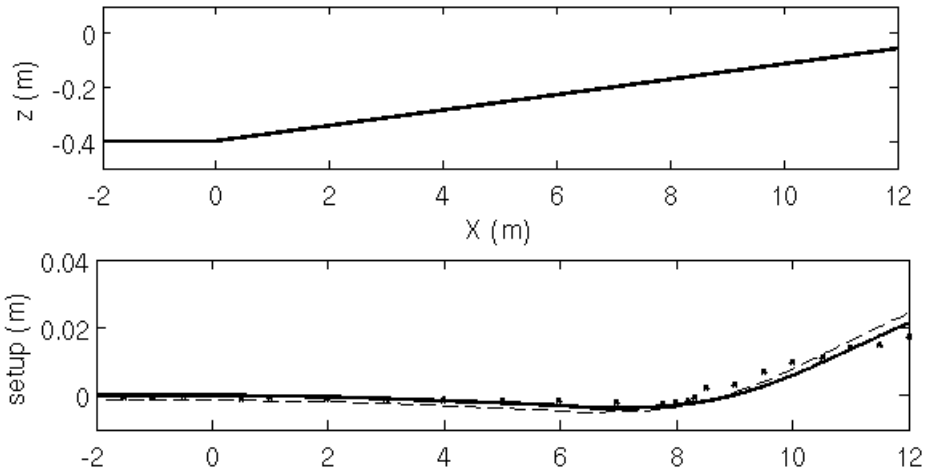

Figure 6.1: Bottom profile (top). Wave set-up Comparison (bottom). Modeled results using EFDC and G3D (—); modeled results using 2DH model and 2-D RS (- - -); and experimental data ($\cdots$).

models.

6.2.1 Undertow over a Sloping Beach

Undertow associated with the mass transport due to wave action significantly alters the mechanism of mixing and transport of pollutants and sediments in nearshore regions, and has been extensively studied (e.g. [96], [94], [93], [34], [97], [42]). Ting and Kirby [96] conducted a laboratory study to measure quantities associated with mass transport for spilling- and plunging-type breakers. Their data for plunging breaker case was recently used by Sheng and Liu [34] who compared the performance of three distinct RSTs (including M11) using the coupled system of the wave model SWAN and the circulation model CH3D.

The objective here is to investigate the performance of the two generalized formulations ($S_{\alpha\beta}^{M11}$ and $S_{\alpha\beta}^{L08}$) with the coupled system discussed earlier. We consider

the plunging breaker case from Ting and Kirby (1994) for which the laboratory data of set-up/down and vertical variation of current profiles are available. This case involves wave propagation over a sloping beach (slope 1:35) in a two-dimensional wave tank with the cross-shore length of 40 m and the alongshore width of 0.6 m. Water depth in the deeper portion of the tank is 0.4 m (Fig. 6.1), and the incident wave height and period are 0.128 m and 5 s respectively.

Two separate simulations for which the radiation stresses are obtained using $S_{\alpha\beta}^{M11}$ and $S_{\alpha\beta}^{L08}$ are considered. The wave model simulations (performed for a domain of size 14 m x 0.6 m) uses 15 triangular elements per wavelength. With the EFDC model, a horizontal grid with 0.35 m resolution is used, and the domain is decomposed into 20 sigma layers in the vertical. On a single processor of a 2.00 GHz computer with 3 GB RAM, the computational time for each simulation to achieve steady-state is around 12 min with a time step of 0.005 s. The modeled results of set-up/down obtained using the EFDC model are compared (in Fig. 6.1) with the experimental data and the results obtained using a 2DH analytical model given by

$$\frac{\partial S_{xx}}{\partial x} = -\rho g(h+\hat{\eta})\frac{\partial \hat{\eta}}{\partial x}. \tag{6.4}$$

(Due to similarity between the modeled results of set-up/down for two simulations, only the results obtained using $S_{\alpha\beta}^{M11}$ are shown in Fig. 6.1). Good agreement is observed between modeled results and other data; for example, the maximum value of the set-up at the shoreline and the location of the breaker line are comparable with the data. This implies that the choice of RST (2-D or 3-D) does not significantly affect the modeled set-up/down values for this case, probably because a balance similar to Eq. (6.4) also establishes for the 3-D model simulation. (Similar comparison is also observed in [34]. However, the 3-D model simulations properly resolve the

Table 6.1: Location of seven measurement stations (Ting and Kirby 1994)

Station	1	2	3	4	5	6	7
Location, x (m)	7.295	7.795	8.345	8.795	9.295	9.795	10.395
Depth, d (m)	0.169	0.156	0.142	0.128	0.113	0.096	0.079

vertical structure of the flow field as shown in Fig. 6.2. The vertical profiles of modeled mean horizontal velocities at seven different measurement stations (Table 1) also compare well (see Fig. 6.3) with the experimental data. As shown in Figs. 6.2 and 6.3, both $S_{\alpha\beta}^{M11}$ and $S_{\alpha\beta}^{L08}$ provide a similar vertical structure of the flow field; however, $S_{\alpha\beta}^{M11}$ slightly overestimates the magnitude to currents especially near the surface. Not surprisingly, the modeled results obtained using $S_{\alpha\beta}^{M11}$ are consistent with the results obtained by Sheng and Liu [34] using M11 formulation, because for forward propagating waves, $S_{\alpha\beta}^{M11}$ reduces to M11 (shown earlier). Minor differences between the flow field results may be attributed to the fact that only the turbulence associated with currents is included with the EFDC model (i.e. the effect of wave-induced bottom stress and wave-enhanced turbulence is assumed to have a minimal effect on the modeled quantities. Details regarding the implementation of these mechanisms can be found elsewhere [98]. It should also be noted that like most studies related to wave-induced circulation, the present study is also based on linear theory which can provide a reasonable estimate of nearshore dynamics; however, inside the surf zone, sometimes nonlinear processes are prevalent.

6.2.2 Standing Wave over a Flat Bottom

We consider the case of a standing wave over a flat bottom for which the surface elevation $\tilde{\eta}$ is expressed analytically using $\tilde{\eta} = 2a \cos kx \cos wt$. This case is analogous to a nearshore situation where a normally incident wave interacts with a fully-reflecting, infinitely-long shore-parallel breakwater or a seawall.

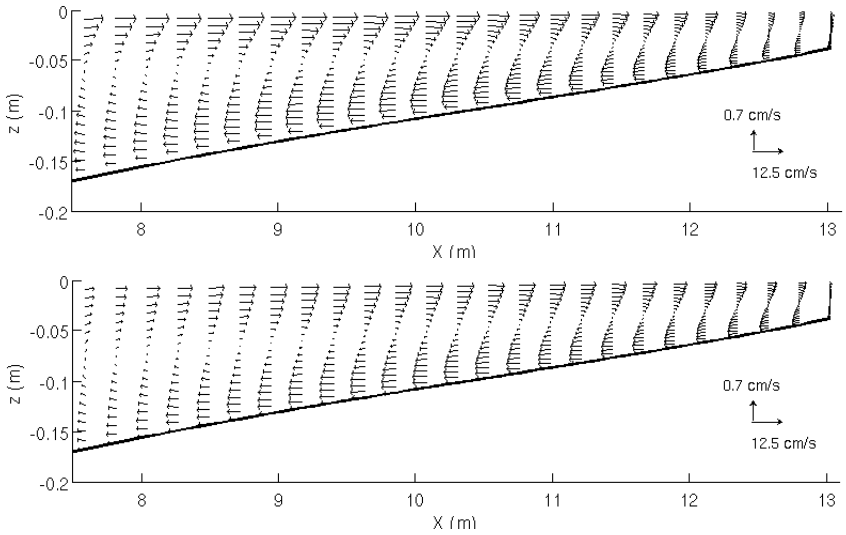

Figure 6.2: Vertical structure of modeled current velocities.

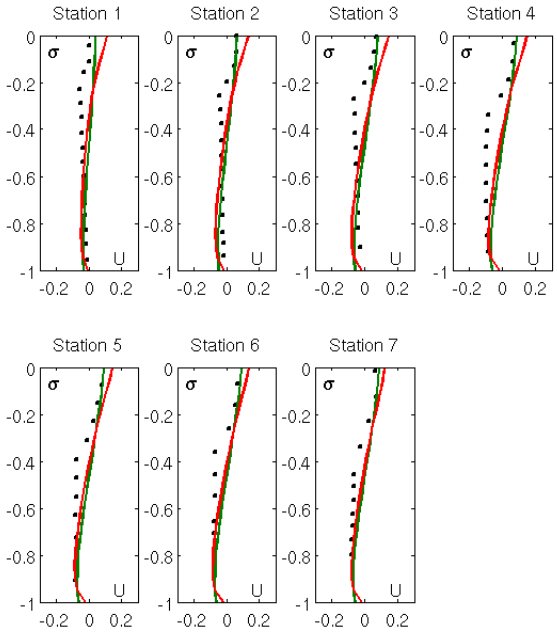

Figure 6.3: Comparison of modeled mean horizontal velocity (—) with data (···). Results using $S_{\alpha\beta}^{L08}$ (green) and using $S_{\alpha\beta}^{M11}$ (red)

Some analytical studies related to mass transport for standing waves are available (e.g. [100] [101], [99]). In general, as discussed by Scandura et al. [99], mass transport for standing waves depends notably on the parameter $D = (\delta/a)^2/2$ where $\delta = \sqrt{2\nu/\sigma}$ is boundary layer thickness, and ν is kinematic viscosity. D is defined as the order of magnitude of the ratio between the dissipative viscous term and the convective term. Analytical expressions for mass transport were obtained by Longuet-Higgins [100] and Ng [101] for $D >> 1$ and by Scandura et al. [99] for $D << 1$. For $D >> 1$, the spatial gradients of radiation stresses and the gradients of set-up/down in the momentum equation balance each other; however, for $D << 1$, the nonlinear convective term also contribute significantly to this balance. Special consideration for boundary layers is required for $D >> 1$, and Longuet-Higgins [100] and Ng [101] therefore divided the overall domain into three vertical regions (a surface boundary layer; a bottom boundary layer; and an intermediate region), allowing effective treatment of boundary layer effects. With the numerical tools used in this study, the boundary layer effects are not properly resolved. Moreover, for $D << 1$, dissipative viscous forces are negligible which makes the modeling of such cases difficult due to stability issues.

Here we consider two hypothetical cases: Case 1 for which a uniform value of viscosity is selected so that $D = 10$, and Case 2 for which the spatially varying vertical and horizontal viscosities are defined using default tools in the EFDC model. Note that the turbulence and bottom friction induced by wave action and boundary-layer effects are ignored in this study. For a flat bottom case with $kh = 0.25$ m, and the incident wave amplitude of $a = 0.1$ m and wave period of $T = 8.0$ sec, the modeled non-dimensional wave height (H/a) varies between 0 to 2 with the maximum and minimum values occurring at the antinodes ($X/L = 0,\ 1/2,\ 1,\ ...$ where X is the cross-shore distance and L is wavelength) and nodes ($X/L = 1/4,$

3/4, ...) respectively. (Wave heights not plotted for brevity). For EFDC simulations, 40 sigma layers are used with the EFDC model, and the horizontal grid is resolved at 0.125 m uniform spacing. On the same computer, with a time step of 0.001 s, the model takes approximately 3 mins to provide a steady-state solution of the set-up/down and current field. For both Case 1 and Case 2, two separate simulations for which radiation stresses are computed using $S_{\alpha\beta}^{L08}$ and $S_{\alpha\beta}^{M11}$ are considered.

The modeled set-up/down is compared in Fig. 6.4 with the standard analytical solution (Bettess and Bettess 1982; Copeland 1985)

$$\hat{\eta} = ak^2 \coth 2kh \cos 2kx \tag{6.5}$$

which is obtained from the horizontal balance equation (relating $\hat{\eta}$ to radiation stresses) in Eq. (6.4). For Case 1, the modeled set-up/down compares very well with the analytical solution. This is consistent with the type of momentum balance (discussed above) that exists for large values of D. However, for Case 2 (i.e. small D), the convective term also participates in this balance, and consequently, some mismatch between the modeled and analytical results is observed near the nodes and antipodes. Similar mismatch between the modeled and the analytical results for a progressive wave case (with small turbulent viscosity) was reported by Mellor (2013); see discussion later. (Due to similarity between the set-up/down results obtained using $S_{\alpha\beta}^{L08}$ and $S_{\alpha\beta}^{M11}$, only the results corresponding to $S_{\alpha\beta}^{L08}$ are shown).

The vertical profiles of current velocities obtained using the EFDC model are shown in Fig. 6.5 and Fig. 6.6 for Case 1 and Case 2 respectively. Since experimental data related to wave-induced circulation for standing waves are not available, the analytical results mentioned above may be used for qualitative verification. The formation of vertical circulation cells (in $x - z$ plane) for standing waves has been

reported by Longuet-Higgins [100], Ng [101] and Scandura et al. [99]. Irrespective of D values. the streamline plots in Figs. 6.5(a,b) and 6.6(a,b) also depict vertical cells for both RSTs $S_{\alpha\beta}^{L08}$ and $S_{\alpha\beta}^{M11}$. (For streamline plots, we use $\partial\psi/\partial x = -\Omega$ and $\partial\psi/\partial\sigma = dU_\alpha$ where ψ is streamfunction). The circulation cells on the left and the right side of the nodes (e.g. at $X = 6.25$ m) have clockwise and counter-clockwise patterns respectively, and as a result, a vertical jet shooting downwards forms under the nodes (e.g. at $X = 6.25$ m). An exactly opposite circulation pattern is found on the left and the right of the antinodes (e.g. at $X = 0$, 12.50 m), and a jet shooting vertically upwards exists under the antinodes. These characteristics of the flow fields are consistent with the analytical works mentioned earlier. Moreover, the magnitudes of velocities (both horizontal and vertical) are much smaller for Case 1 than for Case 2. This difference may be attributed to the different types of momentum balance (see discussion earlier) that exist for these cases. Large velocity magnitudes in Case 2 are due to the contribution of nonlinear convective term in the overall balance. This is consistent with the results shown by Scandura et al. [99] for a flat bottom standing wave case. Similar findings but for a progressive wave case were reported by Mellor (2013). Large velocity magnitudes (one order larger than the Stokes drift) are observed in his results for small values of vertical turbulent viscosity K_M. Mellor (2013) also showed that the convective terms may cause a considerable mismatch between the modeled and analytical set-up/down results as discussed earlier with regards to Fig. 5.6.

The vertical profiles of mean horizontal velocities at locations between the nodes and antinodes (e.g. at $X = 3.13$, 9.38 m) are shown in Figs. 6.5(c,d) and 6.6(c,d) for Case 1 and Case 2 respectively. It can be seen that the modeled results obtained using $S_{\alpha\beta}^{L08}$ and $S_{\alpha\beta}^{M11}$ differ significantly especially near the surface. Note that, as discussed earlier, the term E_D^{M11} in Eq. (5.43) is concentrated near the surface for

$S_{\alpha\beta}^{M11}$, but for this case E_D^{L08} in $S_{\alpha\beta}^{L08}$ is distributed over vertical (as a function of $\sinh 2kh$) with significant contribution to the lower layers. For large values of D, the difference between the results from the two RSTs is more pronounced than for small D values.

Furthermore, Zhang and Liu (2009) also reported the formation of vertical circulation cells using their 3-D RST formulation for standing waves, but the direction of the cell rotation and the magnitude of the currents were off due to inconsistencies in their formulation (discussed earlier in Section 1.) Importantly, this case also illustrates the role of reflection on wave-induced circulation. Dingemans et al. (1987) suggested that the reflection-diffraction effects cannot drive "depth-averaged" currents. However, as shown in Figs. 6.5 and 6.6, reflection effects can drive the flow field in the vertical plane. This is also consistent with deposition and scouring of sediments occurring at the nodes and antinodes for a standing wave (Zhang and Liu, 2009).

6.2.3 Flow around a Detached Breakwater

Next we simulate the wave-induced circulation in a complex domain involving a nearshore detached (shore-parallel) breakwater located on a plane beach. This case resembles a field situation where an artificial breakwater shelters a coastline from wave action. The half-detached breakwater, as depicted in the computational domain shown in Fig. 6.5, has an alonghshore length of 1 m and is installed at a location 1.5 m away from the shoreline. For computations, it is assumed that the breakwater reflects the incident waves perfectly. For this case, the laboratory tests were carried out by Kuroiwa et al. [102] who investigated the mechanism of 3-D circulation in the vicinity of the breakwater. Their measurement points are indicated by A, B, C and D in Fig. 6.7. The input wave is a normally-incident monochromatic

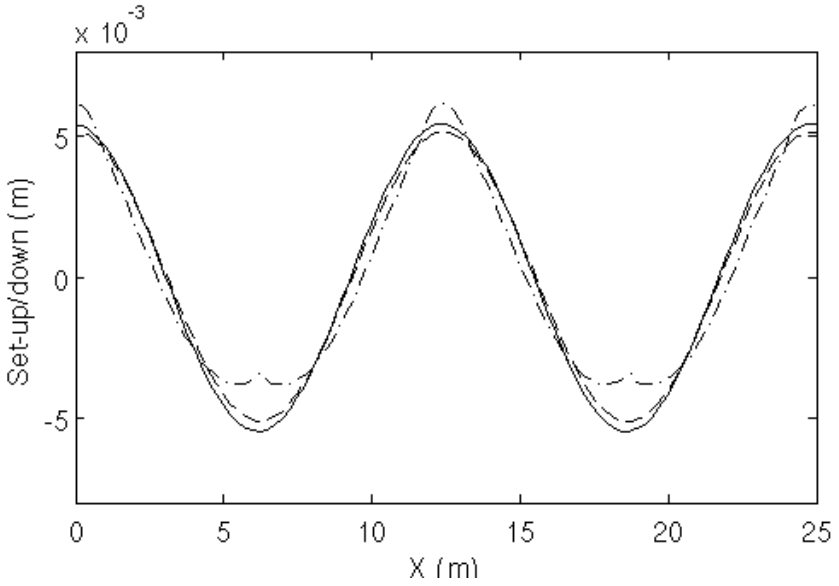

Figure 6.4: Comparison of wave-induced set-up/down. Analytical solution (—), and modeled results using $S_{\alpha\beta}^{L08}$ for Case 1 (- -) and Case 2 (- · -).

wave train with period $T = 1$ s and wave height $H_o = 6.90$ cm. A contour plot of modeled wave heights obtained using the elliptic model is shown in Fig. 6.8. Some typical features of the wave field around detached breakwater such as the formation of a shadow region (with negligible wave activity) behind the breakwater, significant wave reflection on the upwave side of the breakwater, wave diffraction shoreward of the breakwater and the energy dissipation due to wave breaking inside the surf-zone can be observed in Fig. 6.8. The formation of a partial standing wave upwave of the breakwater and the wave breaking along the sloping beach are reminiscent of the previous two tests. Reasonably good agreement between modeled wave heights and data [102] at all measurement points can be observed in Fig. 6.8.

Two separate simulations with EFDC model are considered for which the radiation stresses are obtained using $S_{\alpha\beta}^{L08}$ and $S_{\alpha\beta}^{M11}$. A 250 x 75 grid with a uniform spacing ($\Delta x = 2$ m and $\Delta y = 4$ m) is used in the horizontal direction, and a total of

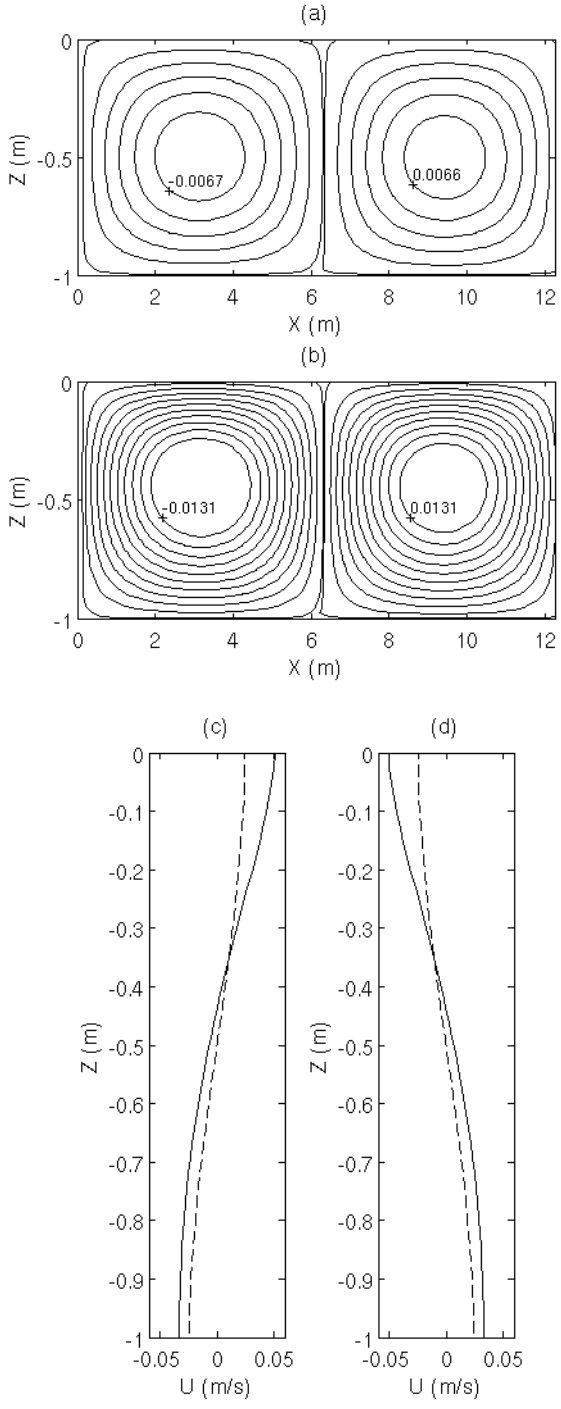

Figure 6.5: Comparison of modeled mean velocity field for Case 1. Streamline plots for mean velocity obtained using $S_{\alpha\beta}^{L08}$ (a) and $S_{\alpha\beta}^{M11}$ (b). Mean horizontal velocity along $X = 3.125$ m (c) and along $X = 9.375$ m (d) obtained using $S_{\alpha\beta}^{L08}$ (- -) and $S_{\alpha\beta}^{M11}$ (—).

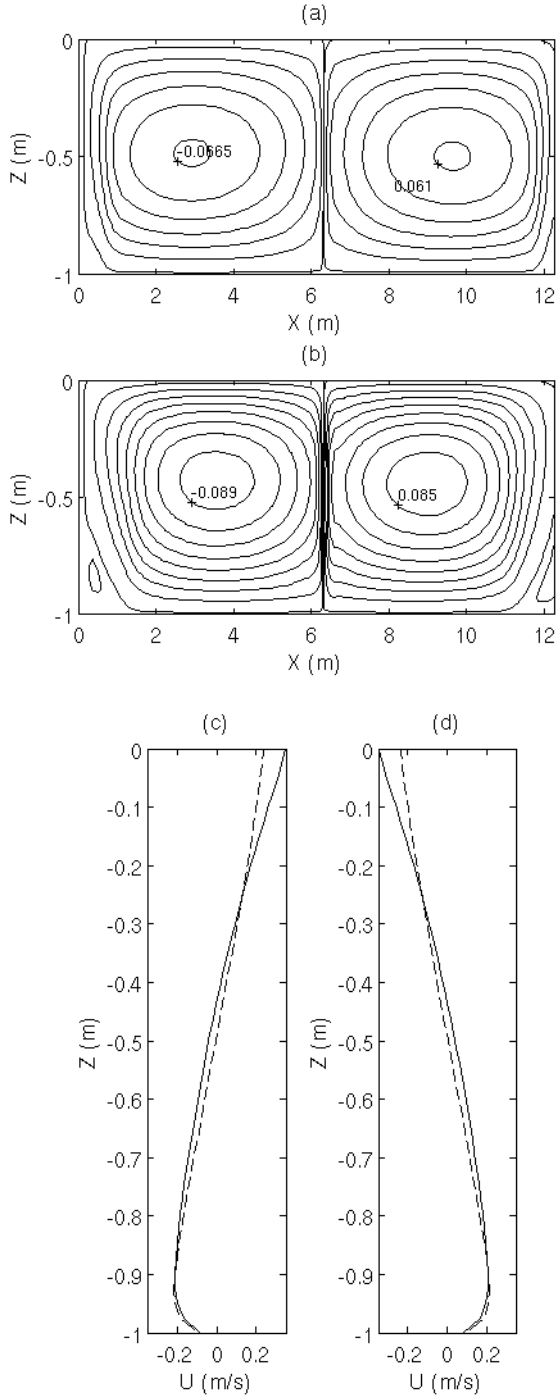

Figure 6.6: Comparison of modeled mean velocity field for Case 2. Streamline plots for mean velocity obtained using $S_{\alpha\beta}^{L08}$ (a) and $S_{\alpha\beta}^{M11}$ (b). Mean horizontal velocity along $X = 3.125$ m (c) and along $X = 9.375$ m (d) obtained using $S_{\alpha\beta}^{L08}$ (- -) and $S_{\alpha\beta}^{M11}$ (—).

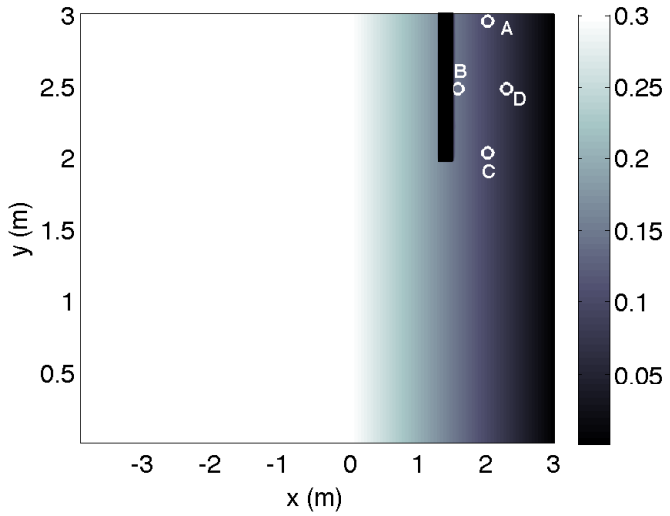

Figure 6.7: Model domain. Circles denote current measurement stations A, B, C and D.

20 sigma layers are used in the vertical. With a time step of 0.035 s, each simulation takes approximately 300 mins to complete a 0.20 day run on the same computer. The spatial variation of wave-induced set-up/down ($\hat{\eta}$) simulated using the EFDC model with $S_{\alpha\beta}^{L08}$ is shown in Fig. 6.9. The spatial variation of $\hat{\eta}$ on the upwave side of the breakwater can be attributed to the formation of standing wave; this is somewhat analogous to the standing wave case discussed earlier.

Further, the wave-induced flow fields (obtained using 3-D EFDC) for the regions upwave and downwave of the breakwater are shown in Figs. 6.10 and 6.11 for the top and the bottom layers. Behind the breakwater, a horizontal circulation cell is observed (in both top and the bottom layers) which is a typical feature of the wave-induced flow field around a detached breakwater. The vertical profiles of the horizontal components of current velocity at four measurement points are compared with the experimental data in Fig. 6.12. (Note that the results obtained using $S_{\alpha\beta}^{M11}$ are not shown here for brevity; discrepancies between the results obtained using

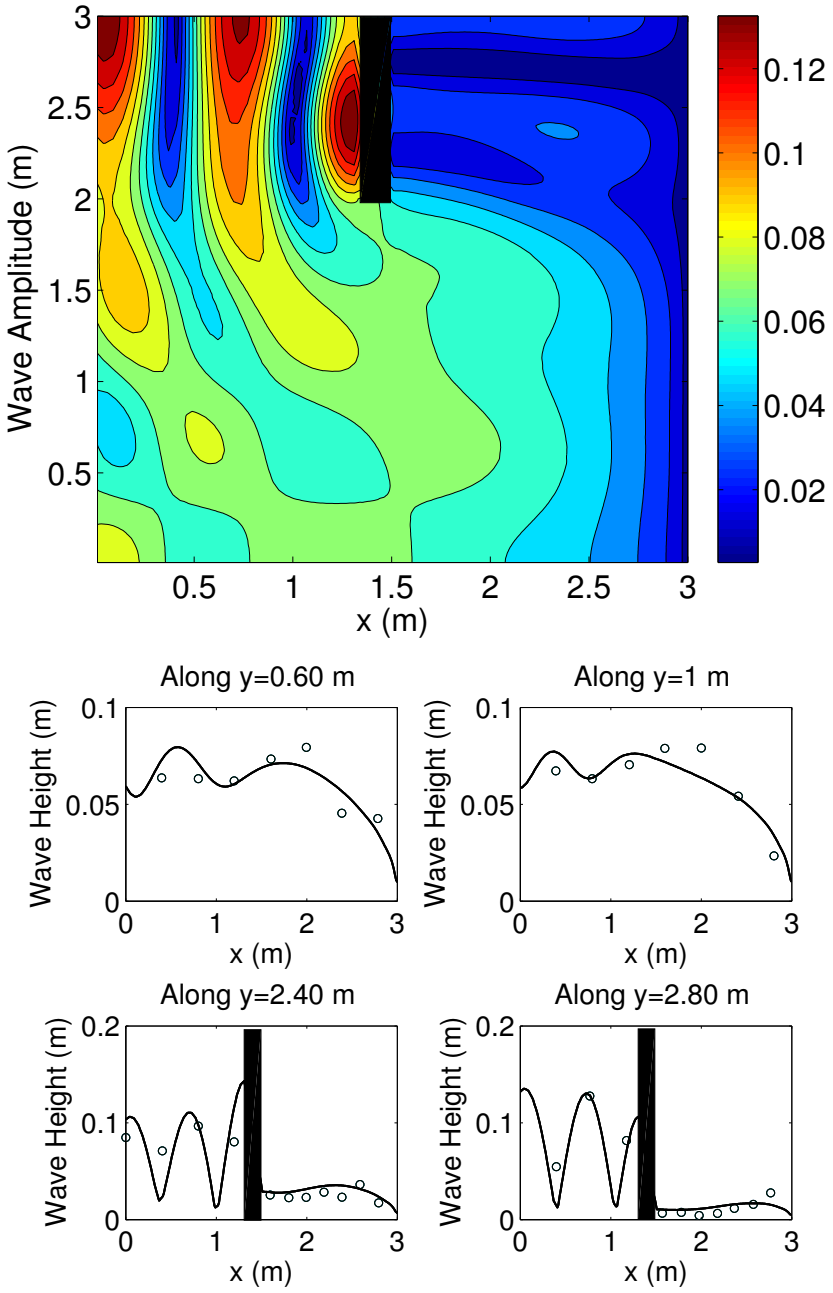

Figure 6.8: Modeled wave height distribution (top), and wave height comparison (bottom). Solid line: modeled wave height, and circles: denote measurements.

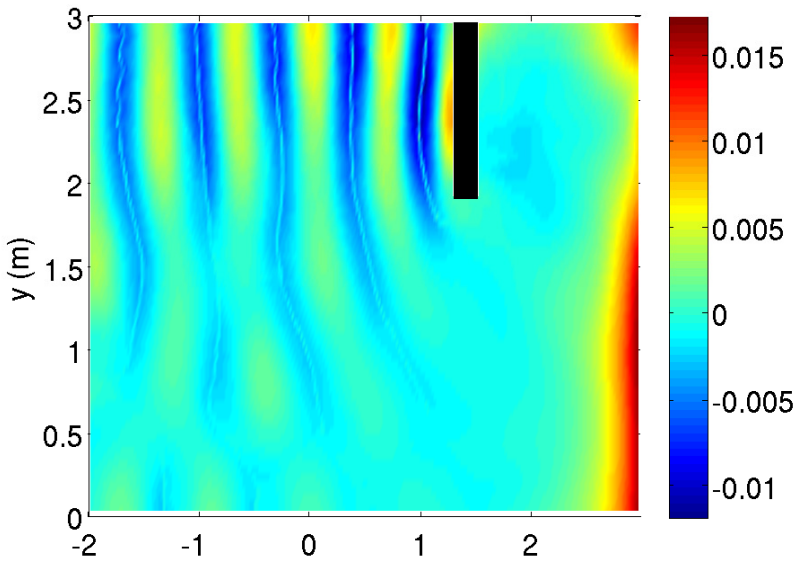

Figure 6.9: Modeled wave-induced set-up/down obtained using EFDC-3D and G3D.

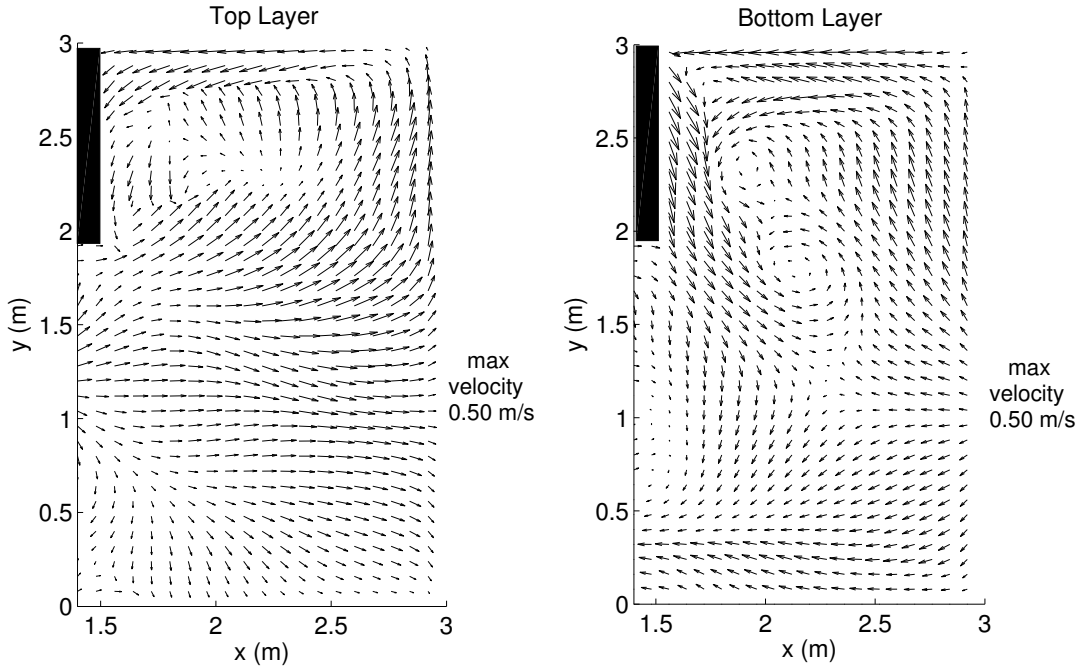

Figure 6.10: Spatial distribution of currents on the downwave side of the breakwater. Top layer (left) and bottom layer (right)

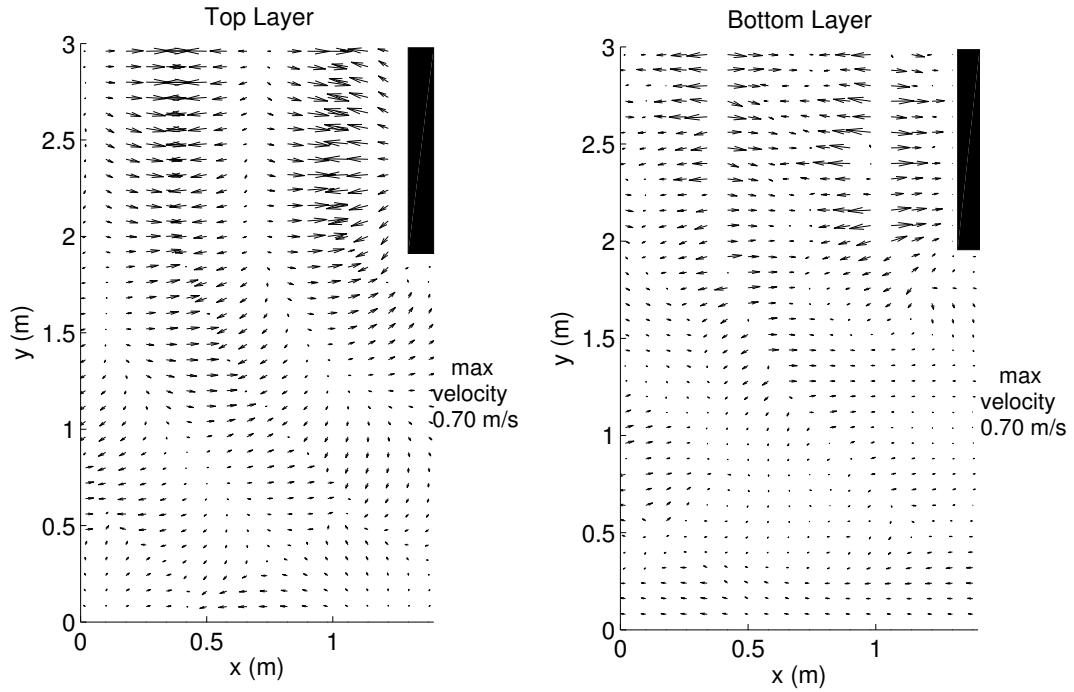

Figure 6.11: Spatial distribution of currents on the upwave side of the breakwater. Top layer (left) and bottom layer (right)

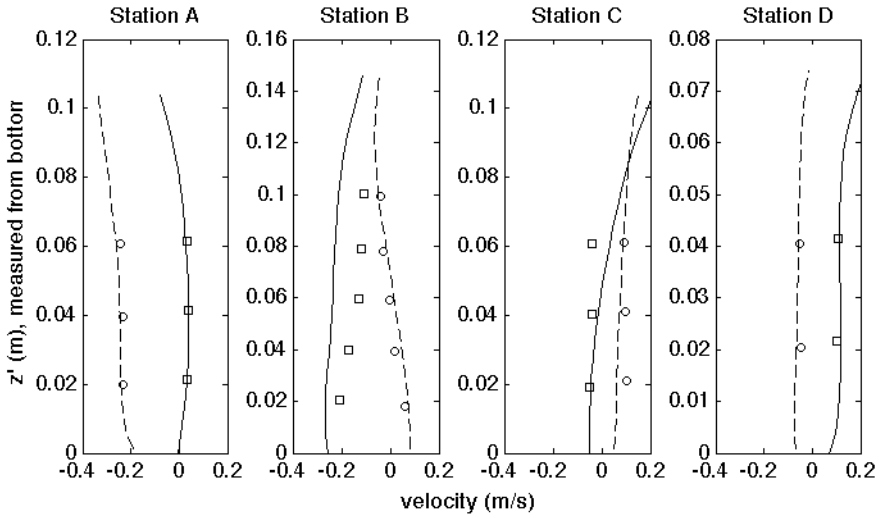

Figure 6.12: Comparison of the vertical profile of current velocity. Modeled x-directed (solid) and y-directed (dashed) velocity components; measured x-directed ($\square$) and y-directed velocities ($\circ$).

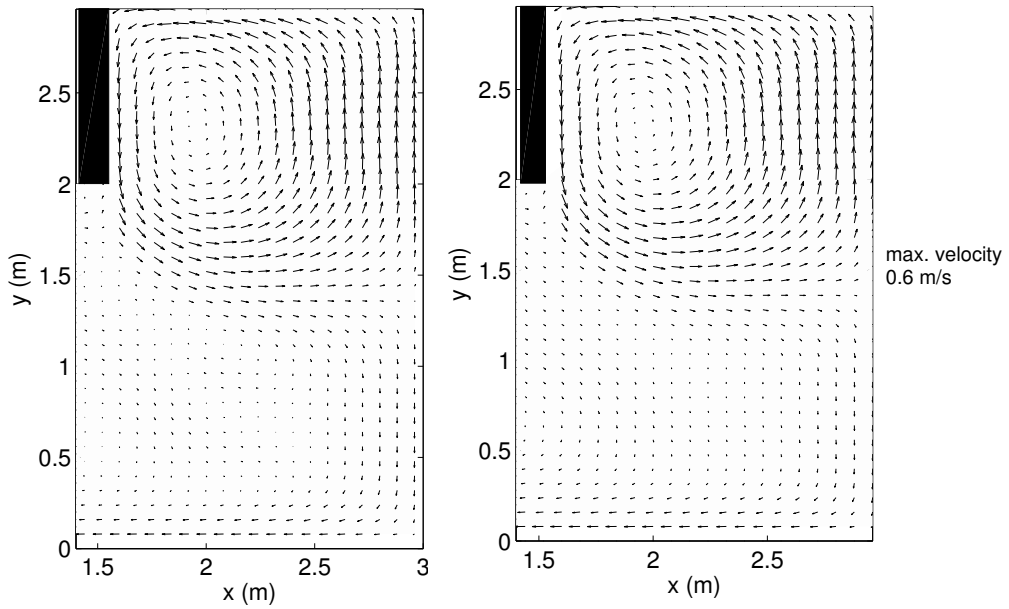

Figure 6.13: Modeled 2DH current field using BB2D (left) and D87 (right).

$S_{\alpha\beta}^{L08}$ and $S_{\alpha\beta}^{M11}$ are of the same order as for Case 2 in the previous section.) For the most part, very good agreement is observed, which confirms the efficacy of the newly derived RSTs with the coupled system. Some discrepancies in the results may be attributed to the choice of the breaking model, ignoring the boundary-layer effects and the wave-enhanced turbulence, etc. In addition, the top and bottom layer flow fields shown in Figs. 6.10 and 6.11 depict the presence of undertow in the surf-zone away from the breakwater (say $y = 1.0$ m) and the formation of vertical circulation cells on the upwave side (say $y = 2.4$ m) of the breakwater. These features of the flow field are also reminiscent of the previous two tests.

Finally, we address the issue of potential numerical errors associated with the computation of higher-order derivative terms present in the generalized RSTs. As noted earlier, such a possibility was raised by Dingemans et al. (1987) who provided

an alternative approximate formulation (referred to as D87 here) suitable for 2-D cases. Due to the lack of detailed data related to 3-D flow field, it is not possible to conclude if the results presented in Figs. (6.10 and 6.11) are contaminated by these numerical errors. However, this issue can be addressed by comparing the 2DH flow fields obtained using D87 and BB2D formulations. Recall that the BB2D formulation also contains higher-order derivatives, and the D87 is an alternative approach which avoids the computation of higher-order derivatives. The wave-induced flow fields obtained using D87 and BB2D formulations with the single-layer EFDC model are shown in Fig. 6.13. In a visual examination, one does not detect any spurious patterns in the flow field obtained using BB2D, confirming that the generalized formulations are not vulnerable to numerical issues as postulated by Dingemans et al. (1987), as long as the grid resolution is $L/10$ or smaller (where L is wavelength).

7. SUMMARY AND CONCLUSIONS

7.1 Summary and Conclusions

This study describes the development of an approach to simulate nonlinear wave transformation in the presence of wave reflection, diffraction, refraction, breaking, etc. The proposed model would be applicable to a wide range of practical wave conditions encountered in harbor and coastal engineering applications. Since linear elliptic equation models (e.g. MIKE21-EMS, CGWAVE, PHAROS, etc) are widely used for harbor applications, an initial foray is made into extending such models to include wave-wave interactions. It is expected that the findings of this research will contribute to the eventual development of a new generation of elliptic harbor wave models. The second-order extension of nonlinear elliptic mild-slope equation was first considered; however, convergence issues inspired the derivation of an evolution-type equation. The ADI scheme with finite-difference method is found to perform satisfactorily for all the validation cases. Boundary conditions typically used for elliptic (linear) wave models were found to be unsatisfactory. A combination of these boundary conditions with dissipative sponge layers and internal wave generation techniques was therefore established and validated for the present model. Further, the "marching" process used in the evolution scheme enables one to compute the nonlinear terms for both wave-wave interactions and breaking simultaneously without requiring an "iterative" process in the usual sense of the word, as described in previous work [6, 12]. Various model features are verified for a variety of wave conditions ranging from deep to shallow water conditions. Reasonable agreement found between data and model results, and superior model performance in some cases, suggest that the proposed approach will enhance the applicability of the elliptic mild-slope wave mod-

els. In addition, this preliminary investigation of the nonlinear mild-slope equation paves the way for the development of more sophisticated finite-element based nonlinear models capable of handling arbitrary shaped domains in a more accurate manner. Based on this, a methodology is then developed which can be used to advance the existing finite element models to include wave-wave interaction effects. The finite element model is applied to simulate nonlinear wave transformation inside Ponce de Leon Inlet, FL. Results show that the methodology developed here performs reasonably well, and has thus improved the applicability existing finite element models based on linear elliptic equation.

Future efforts to extend the present model to handle multidirectional input and steep bathymetric variations may also be warranted. Motivation for such extensions come from the works of Athanassoulis and Belibassakis [82], Belibassakis and Athanassoulis [83] and Toledo and Agnon ([84]) who developed different forms of wave transformation models with improved capabilities to handle steep slopes. Although their models (in the context of nonlinear waves) are primarily applied to domains with one-dimensional bottom variations and are devoid of the mechanisms like breaking dissipation, internal generation, etc., they allow the incorporation of steep bathymetric variations encountered in practice. A study combining developments discussed in the present study with the models in [83, 84] will certainly benefit reseach community and wave modelers.

Furthermore, a preliminary investigation of the three existing RSTs for linear progressive waves is conducted. It is found that the 3-D RST proposed by Mellor [44] does not work satisfactorily. Two alternative approaches (Mellor 2011 and Lin 2008) are considered to obtain generalized 3-D RSTs for using with the complex velocity potential resulting from analytical methods or phase-resolving wave models (e.g. elliptic mild-slope models) applicable to complex wave conditions where re-

flection, diffraction, breaking and focusing effects may play a significant role. This represents a generalization of the work of Bettess and Bettess [24] for such models, and overcomes the limitations of existing formulations which are suitable for forward-propagating waves only. The generalized formulations are implemented in a coupled wave-current system developed using a wave model (based on the elliptic mild-slope equation) and a 3-D circulation model, and the wave-induced flow field is estimated for a series of test cases involving reflection, diffraction and breaking. Three different cases involving wave propagation over a sloping beach, a standing-wave case, and wave interaction with a shore-parallel breakwater are considered. For all cases, modeled results agree well with the results from analytical methods and with laboratory data available in literature. Some discripancy between the modeled velocities obtained using the two newly-developed RSTs are observed; the approach suggested by Lin (2008) is found more reliable. Moreover, it is shown that existing 2-D and 3-D formulations can be deduced from the generalized formulation. It can further be used to derive analytical expressions of 3-D RST for simple cases, e.g. an analytical formulation is developed for full/partial standing waves over a flat bottom for the first time. Using the full standing wave case, it is also deduced that the reflection/diffraction-related effects, which do not drive depth-averaged flow field, can drive currents in the vertical. Finally, numerical issues associated with the higher-order derivatives are addressed, and it is concluded that the generalized formulation is not vulnerable to numerical noise if a reasonable grid resolution of $L/10$ or smaller is used.

BIBLIOGRAPHY

[1] Berkhoff, J.C.W., Booy, N., Radder, A.C.. Verification of numerical wave propagation models for simple harmonic linear water waves Coast Eng 1982;6(3).

[2] Berkhoff, J.C.W.. Computation of combined refraction-diffraction. Proceedings 13th International Conference on Coastal Engineering, Vancouver (Canada) 1972;471-490.

[3] Chandrasekera, C.N., Cheung, K.F.. Extended linear refraction-diffraction model. J Waterw, Port, Coast Ocean Eng 1997;123(5).

[4] Massel, S.. Extended refraction-diffraction equations for surface waves. Coast Eng 1993;97-126.

[5] Li, D., Panchang, V.G., Tang, Z., Demirbilek, Z., Ramsden, J.. Evaluation of an approximate method for incorporating floating docks in two-dimensional harbor wave prediction models. Can J Civ Eng 2005;32(3-4).

[6] Chen, W., Panchang, V.G., Demirbilek, Z.. On the modeling of wave-current interaction using the elliptic mild-slope wave equation. Ocean Eng 2005;32(17-18).

[7] Zhao, L., Panchang, V.G., Chen, W., Demirbilek, Z., Chhabra, N.. Simulation of breaking effects in a two-dimensional harbor wave prediction model. Coast Eng 2001;42(4).

[8] Kirby, J.T., Dalrymple, R.A.. An approximate model for nonlinear dispersion in monochromatic wave propagation models. Coast Eng 1986;9(6).

[9] Walkley, M., Berzins, M.. A finite element method for the one-dimensional extended Boussinesq equations. Int J Numer Meth Fluids 1999;29(2).

[10] Kirby, J.T.. Rational approximations in the parabolic equation method for water waves. Coast Eng 1986;10(355-378).

[11] Panchang, V.G., Demirbilek, Z.. Simulation of waves in harbors using two-dimensional elliptic equation models. In: Advances in Coastal and Ocean Engineering Vol. 7. Word Scientific Publishing Co.; 2001, p. 125–162.

[12] Kostense, J.K., Dingemans, M.W., van den Bosch, P.. Wave-current interaction in harbours. In: 21st Int. Conf. Coast. Engrg., ASCE, New York. 1988, p. 32–46.

[13] Zubier, K., Panchang, V.G., Demirbilek, Z.. Simulation of waves at Duck (North Carolina) using two numerical models. Coast Eng J 2003;45(3).

[14] Panchang, V.G., Wei, G., Pierce, B.R., Briggs, M.J.. Numerical simulation of irregular wave propagation over a shoal. J Waterw, Port, Coast Ocean Eng 1990;116(3).

[15] Agnon, Y., Sheremet, A., Gonsalves, J., Stiassnie, M.. Nonlinear evolution of a unidirectional shoaling wave field. Coast Eng 1993;20(1-2).

[16] Chapalain, G., Cointe, R., Temperville, A.. Observed and modeled resonantly interacting progressive water-waves. Coast Eng 1992;16(3).

[17] Rogers, S.R., Mei, C.C.. Nonlinear resonant excitation of a long and narrow bay. J Fluid Mech 1978;88(1).

[18] Woo, S.B., Liu, P.L.F.. Finite-element model for modified Boussinesq equations. ii: Applications to nonlinear harbor oscillations. J Waterw, Port, Coast Ocean Eng 2004;130(1).

[19] Demirbilek, Z., Nwogu, O.G., Zundel, A.K.. Infra-Gravity Wave Input Toolbox (IGWT): User's Guide. Tech. Rep. CHETN-I-73; USACE, Waterways Expt. Stn., Vicksburg, MS; 2007.

[20] Kaihatu, J.M., Kirby, J.T.. Nonlinear transformation of waves in finite water

depth. Phys of Fluids 1995;7(8).

[21] Tang, Y., Ouellet, Y.. A new kind of nonlinear mild-slope equation for combined refraction-diffraction of multifrequency waves. Coast Eng 1997;31(1-4).

[22] Toledo, Y.. An oblique parabolic equation model for linear and nonlinear wave shoaling. J Fluid Mech 2013;715.

[23] Longuet-Higgins, M. S., Stewart, R. W.. Radiation stresses in water waves: a physical discussion with applications. Deep Sea Res 1964; 11.

[24] Bettess, P., Bettess, J. A.. A generalization of the radiation stress tensor. Applied Mathematical Model 1982;6.

[25] Dingemans, M. W., Radder, A. C., Vriend, H. J.. Computations of the driving forces of wave-induced currents. Coastal Eng 1987; 11.

[26] Moghimi, A., Klingbeil, K., Gräwe, U., Burchard, H. . A direct comparison of a depth-dependent radiation stress formulation and a vortex force formulation within a three-dimensional coastal ocean model. Ocean Model 2013;70.

[27] Kumar, N., Voulgaris, G., Warner, J.. Implementation and modification of a three-dimensional radiation stress formulation for surf zone and rip-current applications. Coastal Eng 2011;58.

[28] Kumar, N., Voulgaris, G., Warner, J., Olabarrieta, M. Implementation and modification of a three-dimensional radiation stress formulation for surf zone and rip-current applications. Ocean Modeling 2012;47.

[29] Lane, E.M., Restrepo, J.M., McWilliams, J.C.. Wave-Current Interaction: A Comparison of Radiation-Stress and Vortex-Force Representations. J Phys Oceanogr 2007;37.

[30] McWilliams, J.C., Restrepo, J.M.. The Wave-Driven Ocean Circulation. J Phys Oceanogr 1999;29.

[31] McWilliams, J.C., Restrepo, J.M., Lane, E. An Asymptotic Theory for the Interaction of Waves and Currents in Shallow Coastal Waters. J Fluid Mech 2004;511.

[32] Xia, H., Xia, Z., Zhu, L.. Vertical variation in radiation stress and wave induced current. Coastal Eng 2004;51.

[33] Mellor, G. L.. The three-dimensional current and surface wave equations. J Phys Oceanogr 2003;33.

[34] Sheng, Y. P., Liu, T.. Three-dimensional simulation of wave-induced circulation: comparison of three radiation stress formulations. J Geophys Res 2011;116.

[35] Ardhuin, F., Jenkins, A. D., Belibassakis, K. A. . Comments on The three-dimensional current and surface wave equations. J Phys Oceanogr 2008;38.

[36] Mellor, G. L.. The depth-dependent current and wave interaction equations: a revision. J Phys Oceanogr 2008;38.

[37] Mellor, G. L.. Corrigendum. J Phys Oceanogr 2011a;41.

[38] Mellor, G. L. . Reply to comments by A.-C. Bennis and F. Ardhuin. J Phys Oceanogr 2011b.

[39] Phillips, O. M.. The dynamics of the upper ocean (2nd ed.). Cambridge University Press 1977.

[40] Bennis, A-C., Ardhuin, F.. Comments on "the depth-dependent current and wave interaction equations: A revision". J Phys Oceanogr 2011;41.

[41] Warner, J. C., Sherwood, C. R., Signell, R. P., Harris, C. K., Arango, H. G.. Development of a three-dimensional, regional, coupled wave, current, and sediment-transport model. Computers and Geosciences 2008;34.

[42] Bruneau, N., Dodet, G., Bertin, X., Fortunato, A. B.. Development of a three-dimensional coupled wave-current model for coastal environments. J Coastal

Res 2011; SI 64.

[43] Wang, J., Shen, Y.. Modeling oil spills transportation in seas based on unstructured grid, finite-volume, wave-ocean model. Ocean Model 2010; 35.

[44] Mellor, G. L. . Unpublished works: *shoni2.princeton.edu/ftp/glm/Corrected2003.pptx* and *shoni2.princeton.edu/ftp/glm/Combined Derivation 2 space.docx.*

[45] Mellor, G. L. . Wave, circulation and vertical dependence. Ocean Dynamics 2013; 63.

[46] Lin, P., Zhang, D.. The depth-dependent radiation stresses and their effect on coastal currents. Hydrodynamics VI: Theory and Applications: Proc., the 6th International Conference on Hydrodynamics, Chang, L., Kervin, Y., eds., Perth, Western Australia, 2004.

[47] Chybicki, W.. On vertical variations of wave-induced radiation stress tensor. Arch Hydro-Eng and Environmental Mech 2008;55.

[48] Herbich, J. B.. Scour around pipelines, piles, and seawalls. Handbook of Coastal and Ocean Engineering, J. B. Herbich, ed., Gulf Publishing Co., Houston, Texas.

[49] Yu, J., Mei, C. C.. Formation of sand bars under surface waves. J Fluid Mech 2000; 416.

[50] Silvester, R., Hsu, J. R. C.. Coastal Stabilization. World Scientific, Singapore 1997.

[51] Sumer, B. M., Fredsøe, J. (2000). Experimental study of 2D scour and its protection at a rubble-mound breakwater. Coastal Eng 2000;40.

[52] Dalrymple, R. A.. On beach cusps formed by intersecting waves. Bull Geol Soc Amer 1975;87.

[53] Liu, P. L. F., Mei, C. C.. Water motion on a beach in the presence of breakwater 2. Mean Currents. J Geophys Res 1976;81.

[54] Copeland, G. J. M.. Practical radiation stress calculations connected with equations of wave propagation. Coastal Eng 1985;9.

[55] Newell, C., Mullarkey, T., Clyne, M.. Radiation stress due to ocean waves and the resulting currents and set-up/set-down. Ocean Dynamics 2005;55.

[56] Zhang, J. X., Liu, H.. Currents induced by vertical varied radiation stress in standing waves and evolution of the bed composed of fine sediments. Int J of Sediment Res 2009;24.

[57] Mei, C. C., Stiassnie, M., Yue, D. K. P.. Theory and applications of ocean surface waves. Advanced Series on Ocean Engineering. World Scientific; 23.

[58] Li, B.. An evolution equation for water waves. Coast Eng 1994;23(3-4).

[59] Lee, C., Suh, K.D.. Internal generation of waves for time-dependent mild-slope equations. Coast Eng 1998;34(1-2).

[60] Steward, D. R., Panchang, V.G.. Improved coastal boundary conditions for water wave simulation models. Ocean Eng 2000;28(1).

[61] Beltrami, G.M., Bellotti, G., Girolamo, P.D., Sammarco, P.. Treatment of wave-breaking and total absorption in a mild-slope equation FEM model. J Waterw, Port, Coast Ocean Eng 2001;127(5).

[62] Wei, G., Kirby, J.T., Sinha, A.. Generation of waves in Boussinesq models using a source function method. Coast Eng 1999;36(4).

[63] Lee, C., Kim, G., Suh, K.D.. Extended mild-slope equation for random waves. Coast Eng J 2003;48(4).

[64] Suh, K.D., Lee, C., Lee, T.H., Park, Y.H.. Experimental verification of horizontal two-dimensional modified mild-slope equation model. Coast Eng 2001;44(1).

[65] Schäffer, H.A., Sørensen, O.R.. On the internal wave generation in Boussinesq and mild-slope equations. Coast Eng 2005;53(4).

[66] Hafsia, Z., Haj, M.B., Lamloumi, H., Maalel, K.. Internal inlet for wave generation and absorption treatment. Coast Eng 2009;56(9).

[67] Kim, G., Lee, C., Suh, K.D.. Internal generation of waves: Delta source function method and source term addition method. Ocean Eng 2007;31(17-18).

[68] Cho, Y.J., Kim, G.S.. Internal generation of waves in fully elliptic modified mild-slope equation using source function method under FEM computational environment. Coast Eng J 2004;46(4).

[69] Bellotti, G., Beltrami, G.M., Girolamo, P.D.. Internal generation of waves in 2d fully elliptic mild-slope equation FEM model. Coast Eng 2003;49(1-2).

[70] Eldeberky, Y., Madsen, P.A.. Deterministic and stochastic evolution equations for fully-dispersive and weakly nonlinear waves. Coast Eng 1999;38(1).

[71] Kaihatu, J.M.. Improvement of nonlinear parabolic dispersive wave model. J Waterw, Port, Coast Ocean Eng 2001;127(2).

[72] Ohyama, T., Kiota, W., Tada, A.. Applicability of numerical models to nonlinear dispersive waves. Coast Eng 1995;24(3-4).

[73] Mase, H., Kirby, J.T.. Hybrid frequency-domain KdV equation for random wave transformation. In: 23rd Int. Conf. Coast. Engrg., ASCE, New York. 1993, p. 474 -487.

[74] Liu, P.L.F., Yoon, S.B., Kirby, J.T.. Nonlinear refraction-diffraction of waves in shallow water. J Fluid Mech 1985;153(1).

[75] Thornton, E.B., Guza, R.T.. Transformation of wave height distribution. J Geophys Res 1983;88(C10).

[76] Eldeberky, Y., Battjes, J.A.. Spectral modeling of wave breaking: Application to Boussinesq equations. J Geophy Res 1996;101(C1).

[77] Whalin, R.W.. The limit of application of linear wave refraction theory in a convergence zone. Research Rept. Tech. Rep. H-71-3; USACE, Waterways

Expt. Stn., Vicksburg, MS; 1971.

[78] Liu, P.L.F.., Tsay, T.K. Refraction-diffraction model for weakly nonlinear water waves. J Fluid Mech 1984;141(3-4).

[79] Madsen, P.A., Sørensen, O.R.. A new form of the Boussinesq equations with improved linear dispersion characteristics. part 2- a slowly-varying bathymetry. Coast Eng 1992;18(3-4).

[80] Madsen, P.A., Banijamali, B., Schäffer, H.A., Sørensen, O.R.. Boussinesq type equations with high accuracy in dispersion and nonlinearity. In: 25th Int. Conf. Coast. Engrg., ASCE, New York. 1996, p. 95–108.

[81] Sharma, A., Panchang, V.G., Kaihatu, J.M., Sørensen, O.R.. Modeling nonlinear wave-wave interactions with the elliptic mild slope equation. Applied Ocean Res. 2014, p. 114-125.

[82] Athanassoulis, G.A., Belibassakis, K.A.. A consistent coupled-mode theory for the propagation of small-amplitude water waves over variable bathymetry regions. J Fluid Mech 1999;389.

[83] Belibassakis, K.A., Athanassoulis, G.A.. A coupled-mode system with application to nonlinear water waves propagating in finite water depth and in variable bathymetry regions. Coast Eng 2011;58(4).

[84] Toledo, Y., Agnon, Y.. Nonlinear refraction-diffraction of water waves: The complementary mil-slope equation. J Fluid Mech 2009;641.

[85] Reddy, J.N.. An Introduction to The Finite Element Method, 2nd Edition, McGraw-Hill, USA 1993.

[86] Panchang, V.G., Wei, G., Cushman-Roisin, B.. Solution of the mild-slope wave problem by iteration. Applied Ocean Research 1991;13.

[87] Smith, S.J., Harkins, G.S.. Numerical wave model evaluations using laboratory data. Proc. Ocean Wave Measurements and Analysis, Waves '97 1997,

Virginia Beach, VA.

[88] Shi, F., Kirby, J.T., Dalrymple, R.A., Chen, Q.. Wave simulations in Ponce de Leon Inlet using Boussinesq model. J Waterw, Port, Coast Ocean Eng 2003;129.

[89] Jin, K. R., and Ji, Z. G. (2001). "Calibration and verification of a spectral wind-wave model for Lake Okeechobee." *Ocean Eng.*, 28, 571-584.

[90] Kuo, A. Y., Shen, J., and Hamrick, J. M. (1996). "The effect of acceleration on bottom shear stress in tidal estuaries." *J. Waterway, Port, Coastal Ocean Eng.*, 122, 75-83.

[91] Singhal, G., Panchang, V. G., and Nelson, J. A. (2013). "Sensitivity assessment of wave heights to surface forcing in Cook Inlet, Alaska." *Continental Shelf Res.*, 63, S50-S62.

[92] Park, K., Jung, H. S., Kim, H. S., and Ahn, S. M. (2005). "Three-dimensional hydrodynamic-eutrophication model (HEM-3D): application to Kwang-Yang Bay, Korea. *Marine Environmental Res.*, 60, 171-193.

[93] Stive, M. J. F., and Wind, H. G. (1986). "Cross-shore mean flow in the surf-zone." *Coastal Eng.*, 10, 325-340.

[94] Svendsen, I. A. (1984). "Mass flux and undertow in a surf zone." *Coastal Eng.*, 8, 347-365.

[95] Svendsen, I. A. (2006). "Introduction to Nearshore Hydrodynamics." *World Scientific*, Singapore.

[96] Ting, F. C. K., and Kirby, J. T. (1994). "Observation of undertow and turbulence in a laboratory surf zone." *Coastal Eng.*, 24, 51-80.

[97] Guannel, G., Özkan-Haller, H. T., and Haller, M. C. (2008). "Modeling undertow over a barred laboratory beach." *Proc., 31st Int. Conf. on Coastal Eng.,* Hamburg, Germany, 940-949.

[98] Grant, W. D., and Madsen, O. S. (1979). Combined wave and current interaction with a rough bottom. *J. Geophys. Res.*, 84, 1797-1808.

[99] Scandura, P., Foti, E., Faraci, C. (2012). Mass transport under standing waves over a sloping beach. *J Fluid Mech*, 701, 460-472.

[100] Longuet-Higgins, M.S. (1953). Mass transport in water waves. *Philos. Trans. R. Soc. London, Ser. A*, 245.

[101] Ng, C.-O. (2004). Mass transport in gravity waves revisited. *J. Geophys. Res.*, 109(C4), C04012.

[102] Kuroiwa, M., Noda, H., and Matsubara, Y. (1998). "Applicabilty of a quasi-three dimesnional numerical model to nearshore currents." *Proc., 13th Int. Conf. on Coastal Engineering,* Vancouver, Canada, 471-490.